Novel spin Hall effect materials and artificially engineered magnetic thin film heterostructures for energy-efficient spintronic memories

Dissertation

zur Erlangung des Doktorgrades der Naturwissenschafen

(Dr. rer. nat.)

der

Naturwissenschaftlichen Fakultät II

Chemie, Physik und Mathematik

der Martin-Luther-Universität

Halle-Wittenberg

vorgelegt von

Herrn Peng Wang

geb. am 20.08.1992 in Harbin, China

Gutachter: Prof. Dr. Stuart S.P.Parkin

Prof. Dr. Günter Reiss

Prof. Dr. Jamal Berakdar

Tag der öffentlichen Verteidigung: 17.11.2022

Abstract

The discovery of novel materials with superior properties is a key factor to promote the progress of highly energy-efficient spintronic memories which are urgently needed to satisfy the increasing demand for data storage. Of special interest are new materials that convert charge current into spin currents with high efficiency. These could impact two distinct classes of spintronic memories, namely magnetoresistive random-access memories (MRAMs), which are already in mass production, and racetrack memories that have great potential for high density and high performance, non-volatile memory-storage devices. For the latter chiral non-collinear spin textures such as domain walls and skyrmions are the basic storage elements.

In this thesis, we first explore charge to spin conversion in thin films deposited from the large family of alloys that combine 5*d* transition metal elements, which have high spin orbit coupling, and aluminum. We demonstrate that some of these alloys show unexpectedly large spin Hall angles and spin Hall conductivities. We show that these high values are derived from large extrinsic scattering at alloy compositions close to a phase transition between amorphous and $L1_0$ structural phases. Second, taking advantage of the high spin Hall values in the $L1_0$ alloy IrAl, we construct synthetic antiferromagnet heterostructures from perpendicularly magnetized ultrathin Co/ Ni / Co tri-layers that are antiferromagnetically coupled via a novel spacer layer of RuAl, itself with a $L1_0$ crystal structure. We demonstrate that this state-of-the-art racetrack device has a several-fold increased current induced domain wall efficiency as compared to prior-art materials**.** Moreover, we establish that all the layers in this synthetic antiferromagnetic heterostructure are oriented in the (001) direction thereby making them compatible with (001) oriented MgO tunnel barriers, a key requisite for high performance magnetic tunneling devices that are needed to read the presence or absence of chiral domain walls in the racetrack itself.

Third, we report the discovery of a novel magnetic thin film material Co_xAl, whose magnetic and electrical properties vary with its composition and thickness. Using Lorentz transmission electron microscopy (LTEM) we have found skyrmion-like bubbles in thin films with the composition $Co_{2.3}Al$ that are grown on IrAl as an underlayer. Preliminary studies suggest that the skyrmions arise from an interface derived Dzyaloshinskii – Moriya exchange interaction (DMI) with the IrAl underlayer since Co_xAl is centrosymmetric.

Finally, we show the results of artificially engineering ferrimagnetic Mn_xSn (Sb) Heusler alloys with various thicknesses and compositions. We demonstrate electrical current induced magnetization switching of thin films formed from magnetic $Mn_{2.15}Sn$ alloys using IrAl

underlayers that display ultralow critical current densities in zero field. We find evidence for both damping-like and field-like spin orbit torques arising from the IrAl underlayers.

Our findings of several novel materials are significant contributions to the further successful implementation of spintronic memories with high performance and high capacities.

Contents

1. Introduction 8

1.1 Thin films deposition by magnetron sputtering 10

1.2 Characterization techniques for deposited thin films 12

1.2.1 *X*-ray diffraction measurements of thin films 12

1.2.2 Characterization the roughness of thin film by atomic-force microscopy 12

1.2.3 Sheet resistance measurements by four-point probe method 13

1.2.4 Superconducting Quantum Interference Device - Vibrating Sample Magnetometer 14

1.2.5 Rutherford Backscattering Spectrometry (RBS) 15

1.3 Device fabrication from blanket thin films 16

1.3.1 Spin coating of samples. 16

1.3.2 Lithography of samples 17

1.3.3 Developing process for samples 17

1.3.4 Etching process and electrode deposition process for samples. 17

1.4 Electronic transport measurement setup 18

1.5 Domain wall motion measurement setup 19

1.6 Ion-milling machine 20

1.7 JEOL High resolution transmission electron microscopy 20

1.8 Magnetic force microscopy 21

1.9 Current-in-plane tunneling (CIPT) setup and measurements 22

2. Spin Hall effects of 5*d* transition metal – aluminum (M_xAl_{100-x}) alloy thin films 23

2.1 M_xAl_{100-x} alloys thin films growth 23

2.2 *X*-ray diffraction results of M_xAl_{100-x} alloy thin films 23

2.3 Sheet resistivity of M_xAl_{100-x} alloy thin films 26

2.4 High resolution cross section transmission electron microscopy images of M_xAl_{100-x} thin films 27

2.5 Spin Torque Ferromagnetic Resonance (ST-FMR) measurements for M_xAl_{100-x} / $Co_{20}Fe_{60}B_{20}$ bilayer samples 28

2.5.1 Introduction and mechanisms of ST-FMR 28

2.5.2 ST-FMR line-shape method 29

2.5.3 ST-FMR line-width method 31

2.5.4 Spin Hall effect from line-width analysis of M_xAl_{100-x} / $Co_{20}Fe_{60}B_{20}$ bilayer samples 33

2.6 Summary 37

3. [001] orientation synthetic antiferromagnets for racetrack memories 38

3.1 Introduction of racetrack memories 38

3.2 The application of racetrack memories 39

3.3 The mechanism of domain wall motion 40

3.3.1 The concept of the domain wall ... 40
3.3.2 Motion of the domain wall ... 41
3.3.3 Relationship among spin torques, motion speed and efficiency of domain walls ... 41
3.3.4 Synthetic antiferromagnets used as racetrack memories ... 42
3.4 Perpendicular magnetic anisotropy of Co / Ni / Co multilayer with [001] orientation ... 44
3.5 Domain wall motion of Co / Ni / Co multilayer with [001] orientation ... 48
3.6 [001] orientation synthetic antiferromagnets with $L1_0$ RuAl alloy as space layer ... 49
3.7 Domain wall motion in synthetic antiferromagnets with [001] orientation ... 51
3.8 Magnetic properties and domain wall motion performance of $Co_{90}Fe_{10}$ | Ni | $Co_{90}Fe_{10}$ multilayer ... 55
3.9 Growth of M_xAl_{100-x} and M_xAl_{100-x} – SAF structure on top of Si (001) wafer ... 55
3.10 Spin-orbit torque switching of IrAl - Co based SAF structures ... 57
3.11 Exploration of magnetic tunnel junction with $Ir_{42}Al_{58}$ under layer ... 60
3.12 Summary ... 67
4. Thin film structure design for skyrmions ... 68
4.1 Skyrmions concept ... 68
4.1.1 Skyrmions in noncentrosymmetric magnets ... 69
4.1.2 Skyrmions in centrosymmetric magnets ... 70
4.1.3 Skyrmions in multilayer thin films ... 72
4.2 Skyrmions in Co_xAl films ... 79
4.2.1 Crystal structure, magnetic and electrical properties of Co_xAl films ... 79
4.2.2 Magnetic spin textures of 30 nm $Co_{2.3}Al$ film ... 84
4.3 IrAl / $Co_{2.3}Al$ bilayer structure ... 86
4.3.1 Crystal structure, magnetic and electric properties of IrAl / $Co_{2.3}Al$ bilayers ... 86
4.4 Electric, magnetic properties and domain structures of $Co_2Pt_{0.45}Al$ thin film ... 92
4.5 Summary ... 94
5. Magnetization switching of tetragonal distorted Mn_xSn (Sb) Heusler alloys by seeded IrAl ... 95
5.1 Introduction of current induced magnetization switching ... 95
5.2 Magnetic properties and Hall effect of IrAl / *t* Mn_xSn (Sb) samples ... 97
5.3 High resolution cross section TEM images of IrAl / Mn_xSn (Sb) bilayer structures ... 97
5.4 Current induced magnetization switching in IrAl / Mn_xSn (Sb) bilayer samples ... 99
5.5 Current induced switching and SOT efficiency in IrAl / Mn_xSn bilayer structures ... 104
5.5.1 Magnetic and electrical properties of 90 Å $Mn_{2.15}Sn$ layer ... 106
5.6 XMCD analysis of IrAl / $Mn_{3.05}Sn$ bilayer structure ... 108
5.7 Summary ... 111
6. Summary and Outlook ... 112

Bibliography **114**
Acknowledgement **124**
List of Publications **125**
Academic Curriculum Vitae **126**

Acronyms

MRAMs	Magnetoresistive random-access memories
SAFs	Synthetic antiferromagnets
TMR	Tunneling magnetoresistance
SOTs	Spin-orbit torques
MTJ	Magnetic tunnel junction
XRD	X-ray diffraction
AFM	Atomic Force Microscopy
SQUID	Superconducting quantum interference device
VSM	Vibrating sample magnetometer
RBS	Rutherford Backscattering Spectrometry
PPMS	Physical property measurement system
FIB	Focused-ion beam
TEM	Transmission electron microscopy
LTEM	Lorentz- Transmission electron microscopy
MFM	Magnetic force Microscopy
ST-FMR	Spin-torque ferromagnetic resonance
PMA	Perpendicular magnetic anisotropy
RKKY	Ruderman-Kittel-Kasuya-Yosida
HR-TEM	High-resolution transmission electron microscopy
STT	Spin transfer torque
SOT-MRAMs	Spin-orbit torque - magnetoresistive random-access memories
STT-MRAMs	Spin transfer torque - magnetoresistive random-access memories
DMI	Dzyalonshinski-Moriya interaction
AHE	Anomalous Hall effect
OHE	Ordinary Hall effect
THE	Topological Hall effect
XMCD	X-ray magnetic circular dichroism
CMOS	Complementary metal-oxide-semiconductor
MR	Magnetoresistance
CIPT	Current-in-plane tunneling

1. Introduction

Lowering the energy consumption and improve the performance in current reading and writing speed as well as decreasing the writing error rate are most important factors for the practical application of magnetoresistive random-access memories (MRAMs) [1,2,3]. The typical structure stack for MRAMs involved in materials that displays large spin Hall effect, ferro/ferrimagnetic thin films, antiferromagnetic materials, artificially synthetic antiferromagnet, MgO or AlN tunneling barrier, finally full magnetic tunnel junction which shows high tunneling magnetoresistance (TMR) [4-10].

Spin Hall effect is a kind of effect that converting charge current into spin current with charge current injecting into strong spin-orbit coupling materials usually include heavy metals such as Pt[4], Ta[11], W[12], and WO_x[13], topological insulators like BiSe[14], BiTe[15], BiSb[16], $(BiSb)_2Te_3$[17], 2D materilas like WTe_2[18,19], $MoTe_2$[20], $PtTe_2$[21], and 1T-TaS_2[22], antiferromagnet Weyl semimetal Mn_3Sn[23], Mn_3Pt[24] and Mn_3Ir[25] et al. The charge current flow through *x* direction and spin polarized current transport along *z* axis direction. The conversion efficiency between charge and spin current called spin Hall angle (θ_{SH}). The spin Hall conductivity (σ_{SH}) is defined as $\sigma_{SH} = \theta_{SH} \times \sigma_{xx}$, σ_{xx} is the longitudinal conductivity of materials [26, 27]. Materials showing large spin Hall angle and spin Hall conductivity is what we pursued to improve the performance of non-volatile magnetic memory devices.

Synthetic antiferromagents (SAFs) is grown by magnetron sputtering with Co, Ni, Pt, and Ru multi-elements [28, 29], which has been frequently used as free layer in magnetic tunnel junction. Platinum can be used as spin Hall effect layer to provide spin-orbit torques for the purpose of driving the domain wall motion in films with perpendicular magnetic anisotropy, which is constructed by Pt / Co / Ni / Co multilayer [30, 31]. Ruthenium can be used as spacer layer to separate the top and bottom Co / Ni / Co multilayer. Then the exchange coupling torque in between can fix the two magnetic moment pointed antiparallel. The low ratio between remanent and saturation magnetization (M_r / M_s) in SAFs suggests the large exchange coupling torque. The domain walls form from nonequivalent magnetization dynamics in between two magnetic domains with different magnetization direction. The motion of domain walls is driven by both spin transfer torque and spin-orbit torques. The exchange coupling torque originates from antiferromagnetic exchange coupling field, which is key to account for high motion velocities of domain walls in the SAFs racetrack memories. The spin transfer torque is that when charge current flowing through the magnetic materials, the charge current can be spin polarized. The spin-polarized current can transfer the spin angular momentum to the conduction

electrons to make it pointing along with the transport direction of spin-polarized current, the torque is called spin transfer torque.

The spin current originates from intrinsic spin Hall effect in strong spin-orbit coupling materials and / or interfacial Rashba-Edelstein effect. Spin current can be absorbed when flow into adjacent ferro- / ferri-magnetic materials, then it exert torques on the magnetization of ferro- / ferri-magnets, which is called spin-orbit torques (SOTs) [32, 33]. The SOTs is used to manipulate the magnetization of thin films and drive the motion of different magnetic spin textures such as domain walls, skyrmions, and antiskyrmions et al [34].

The magnetic tunnel junction lies at the heart of MRAMs, tunneling magnetoresistance shows giant difference with field applied parallel and antiparallel to the magnetization direction of MTJ. High and low magnetoresistance can present status of "1" and "0" respectively, which is the basic digital bit [9, 10]. The magnetic tunnel junction is mainly composed of several layers including two permanent magnetic layer separated by several nanometer thin insulating layer such as [001] oriented MgO or AlN [9, 10, 35]. The permanent magnets used in MTJ usually contain $Co_{70}Fe_{30}$, $Co_{90}Fe_{10}$, $Co_{20}Fe_{60}B_{20}$, $Co_{40}Fe_{40}B_{20}$, cubic Co layers and/or binary or ternary Heuslers [9, 10, 36, 37]. Typical MRAMs stacks include bottom heavy metal electrode and top magnetic tunnel junction bits. Charge current or voltage pulses is input into the bottom line, which used as writing bits then spin-orbit torques from bottom heavy metal electrode can manipulate the magnetization of MTJ [1, 2, 3]. We can detect the change of magnetoresistance from MTJ as reading bits. Energy efficiency, low error rate of writing and reading as well as ultrafast reading and writing operation lies at the heart in improving the performance of MRAMs. Racetrack memories is a new kind of memory using the motion of domain walls in micrometer wires or nanowires as digital bits for current reading and writing operation [38, 39]. The threshold current density to drive the motion of domain walls and motion speed of the domain walls are two important parameters to evaluate their practical application. The integration of racetrack memories and magnetic tunnel junction provides a new route to explore multifunctionalities of MRAMs [40]. More important is that the discovery of new spin Hall conductivity materials, which showing large spin-orbit torques, and find out new magnetic materials or thin film stacks to replace conventionally used permanent magnet are two important goals in the area of new MRAMs exploration.

1.1 Thin films deposition by magnetron sputtering

The magnetron sputtering equipment that we used is an AJA 'Flagship Series' sputtering system, which consists 11 confocal DC magnetron sputtering sources and 1 off-axis MgO radio frequency sputtering gun, which is shown in Figure 1.1a. All sputtering targets pointed to the center of sample holder shown in Figure 1.1b. Magnetron sputtering is kind of technique that utilize the magnetron sources which is consist of small south and north magnet integrated into a copper plate shown in Figure 1.1c. The polarity between the center and surrounding magnet is opposite. High voltage power is utilized to ionize the Argon gas, then Argon ion can hit the surface of metal target with metal atoms production, the power control panel is shown in Figure 1.1d. Under the effect of electric field applied between the metal target and substrate holder, the metal atoms can fly to the substrates' surface. The process of magnetron sputtering is shown in Figure 1.1e and f, the color of plasma is pink usually, however the color is different from target to target. The thickness of films is controlled by magnetron sputtering time and power, the deposition pressure is 3 mTorr. The targets on top of magnetron ground is protected by ground, chimney and shutter, which is shown in Figure 1.1b. For ultrathin and multilayer films deposition, we can control the close and open state of shutter. The accuracy of shutter open and close is no more than 0.5s. The alloys thin films is prepared by magnetron co-sputtering from two targets or one alloy target sputtering with different power for the purpose of tuning the composition of alloy thin films. Conventionally the metal or alloy targets that we use for sputtering is ignited by direct current. However, for oxides growth like MgO, we use radio-frequency sputtering. Radio-frequency sputtering technique is involved in alternating the electrical potential of the current in the vacuum environment at radio frequencies to avoid a charge building up on certain types of sputtering target materials.

Figure 1.1 (a) - (f) Magnetron sputtering equipment and process of sputtering.

1.2 Characterization techniques for deposited thin films

1.2.1 *X*-ray diffraction measurements of thin films

The *X*-ray diffraction equipment that we used is a type of Bruker D8 Discover machine shown in Figure 1.2 a. The sample is mounted on a goniometer, the goniometer is used to tune the position where *X*-ray beam incident into. The incident *X*-ray beams will be scattered by atom planes, the atoms can be viewed as different scattering centers. The periodic arrangement of scattered atoms can produce a regular array of spherical waves. These waves add constructively in some specific directions, determined by Bragg's law:

$$2\,d\sin(\theta) = n\,\lambda \tag{1}$$

where d is the lattice of atoms plane, θ is the incident angle, n is any integer and λ is the wavelength of incident beam. *X*-ray diffraction results include the peak intensity, peak position and peak width, which can reflect the crystal quality, main crystal phase composition and the growth orientation of crystals. More important is that we can calculate both in - plane and out - of - plane lattice parameter to determine the crystal structure. Then we can make sure the space group and point group that the crystals belong to. This is very useful information to understand their crystal symmetry.

Figure 1.2 (a) Bruker D8 X-ray diffraction facility.

1.2.2 Characterization the roughness of thin film by atomic-force microscopy

Atomic-force microscopy is a kind of scanning probe microscope, which is used to characterize the three-dimensional morphology of thin film samples by means of interaction force between tip and sample surface. Atomic force microscopy has higher resolution compare with optical

microscopy, also it did not use lenses or beam irradiation. This method is not limited in spatial resolution due to diffraction and aberration, and preparing a space for guiding the beam (by creating a vacuum) and staining the sample are not necessary. AFM is used to measure the surface roughness and thickness of thin film samples. The mode of AFM that we use is Dimension Icon that is used to perform nanoscale imaging, while simultaneously capturing nanomechanical material information. The schematic of AFM setup and measurement procedure as well as images is shown in Figure 1.3 a and b.

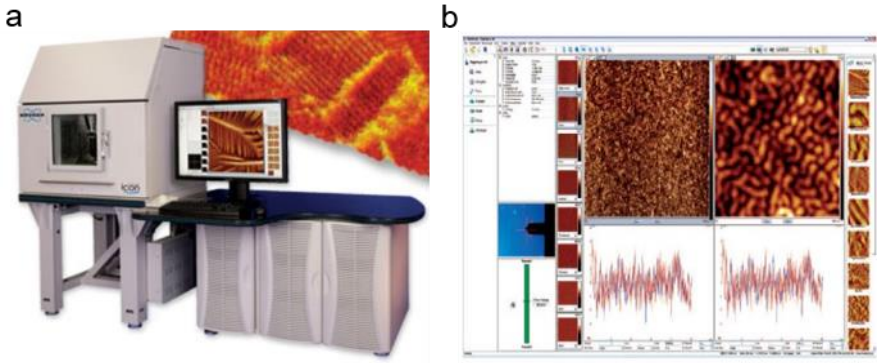

Figure 1.3 (a) Bruker D8 Atomic Force Microscopy facility, (b) Sample image of thin films probed by AFM.

1.2.3 Sheet resistance measurements by four-point probe method

The sheet resistance R square (R_{sq}) of thin films can be measured by four-point probe station. The measurement facility and schematic is shown in Figure 1.4 a and b. The sheet resistivity ρ can be defined as below:

$$\rho = c \times R_{sq} \times t$$

where t is thickness of thin films. According to the sample dimension, the coefficient c is different from samples to samples. The coefficient is dependent on the ratio between length and width of samples. The brand and modes of four-point probe station is FPP5000 produced by Veeco Instrument. The bulk resistivity of M_xAl_{100-x} thin films is measured by four-point probe station.

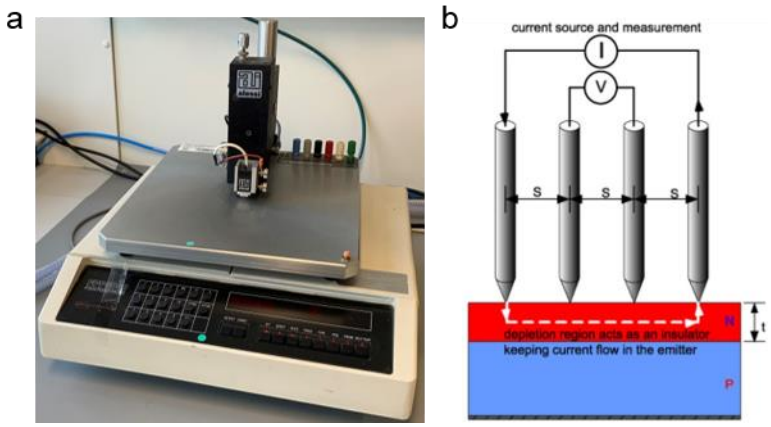

Figure 1.4 (a) Four-point probe station facility. (b) Measurement schematic of four-point probe.

1.2.4 Superconducting Quantum Interference Device - Vibrating Sample Magnetometer

We measure the magnetization hysteresis loop and temperature dependent magnetic signals by Superconducting Quantum Interference Device - Vibrating Sample Magnetometer (SQUID-VSM) produced by quantum design company. SQUID is a very sensitive magnetometer used to measure magnetic moment values in ferri-/ferromagentic materials and antiferromagnetic materials, based on superconducting loops containing Josephson junctions. SQUIDs are sensitive enough to measure fields as low as 5×10^{-14} T and it contains two modes including both direct current (D.C) and radio-frequency (R.F) modes. The radio - frequency can work with only one Josephson junction. The facility and schematic of the simple measurement set up is shown in Figure 1.5 a and b. A constant biasing current is maintained in the SQUID device, the measured voltage oscillates with the changes in phase with two Josephson junction, which depends on the magnetic flux. Counting the oscillations allows to evaluate the flux change which has occurred. Thus it is essentially to convert magnetic flux into voltage.

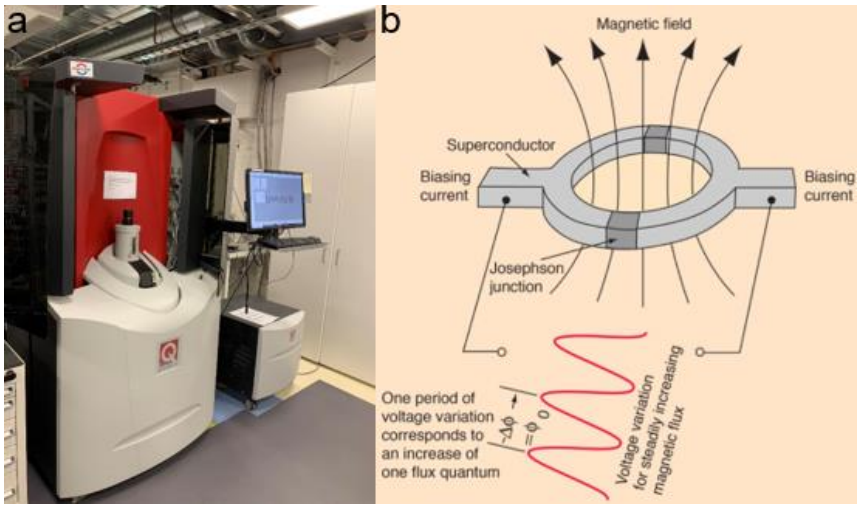

Figure 1.5 (a) SQUID-VSM facility, (b) The schematic figures of SQUID-VSM measurements.

1.2.5 Rutherford Backscattering Spectrometry (RBS)

RBS is used to determine the structure and composition of materials by measuring the backscattering of a beam of high energy ions (typically protons or alpha particles) impinging on a sample. We describe the Rutherford backscattering as an elastic, hard sphere collision between a high kinetic energy from the incident beam (the projectile) and a stationary particle located in the sample (the target). An RBS instrument generally includes three essential components:

(1) An ion source, usually alpha particles (He^{2+} ions) or, less commonly protons.
(2) A linear particle accelerator capable of accelerating incident ions to high energies, usually in the range 1-3 MeV.
(3) A detector capable of measuring the energies of backscattered ions over some range of angles.

The setup of RBS is shown in Figure 1.6a, two common source/acceleration are used in commercial RBS systems. “Tandem accelerators”, start with a source of He^- ions and position the position terminal at the center of acceleration tube. A stripper element included in the positive terminal removes electrons from ions which pass through, converting He^- ions to He^{++} ions. The ions thus start out being attracted to the terminal, pass through and become positive, and are repelled until they exit the tube at ground. This arrangement, though more complex, has the advantage of achieving higher accelerations with lower applied voltages: a typical tandem accelerator with an applied voltage of 750 kV can achieve ion energies of over 2 MeV.

The energy loss of a backscattered ion is dependent on two processes: the energy loss in scattering events with sample nuclei, and the energy lost to small-angle scattering from the

sample electrons. The first process is dependent on the scattering cross section of the nucleus and thus on its mass and atomic number. For a given measurement angle, nuclei of two different elements will therefore scatter incident ions to different degrees and with different energies, producing separate peaks on an N(E) plot of measurement count versus energy. These peaks are characteristic of the elements contained in the material, providing a means of analyzing the composition of a sample by matching scattered energies to known scattering cross-sections. Relative concentrations can be determined by measuring the heights of the peaks, the example is shown in Figure 1.6 b.

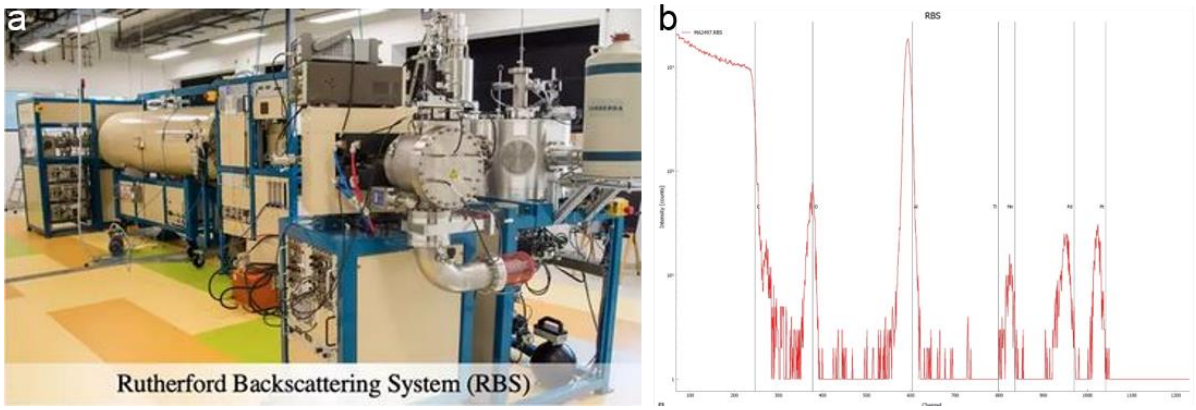

Figure 1.6 (a) RBS set up and (b) RBS peak from films contain different elements.

1.3 Device fabrication from blanket thin films

1.3.1 Spin coating of samples.

The substrates that we used for thin film growth include [001] orientation MgO and $MgAl_2O_4$ substrates. For photoresist spin coating, the type of photoresist is ARN4340. A few drops of photoresist is put on top of 10 × 10 mm substrates with spin coating speed of 4000 round/min. The process is shown in Figure 1.7 a. The coated samples is put on top of hot plate for 1min with 90 degrees. After baking for 1min, the samples need to be put on cooling plate for 1 min. After that the samples can be put inside MLA150 maskless lithography tool produced by Heidelberg instruments.

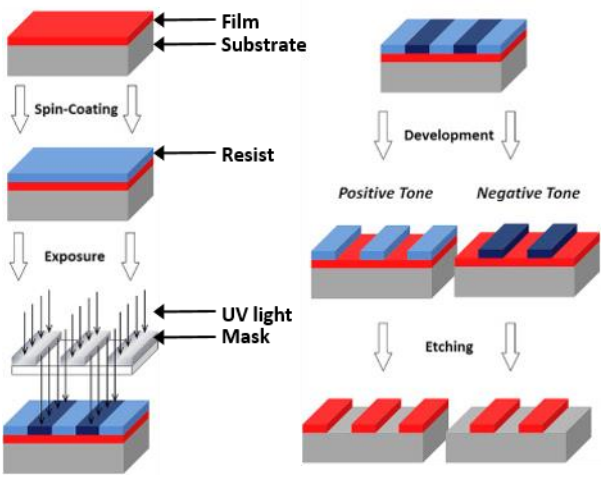

Figure 1.7 Schematic of device fabrication process.

1.3.2 Lithography of samples

The photoresist is exposed under the ultraviolet light with wavelength of 375 nm and 210 mJ/cc energy units. The device pattern is designed by Layout software. After exposed, the samples need post-baking with 95^{o} for 2 min. After baking, the exposed samples need to be cooled down put on top of the cooling plate for 1 min.

1.3.3 Developing process for samples

The developer type that we used for developing is AR300-475, we put the samples in the developer for 1 min then rinsed with deionized water for 1min. Then the device design is showed on top of samples surface.

1.3.4 Etching process and electrode deposition process for samples.

After the device pattern showed on samples' surface, we attach the samples on top of substrate holder with tape on back side, then we put it into etching machine. Scia 200 milling systems. The angle between etching gun and samples is 90^{o}. We usually do over etching for 2 ~ 3 min after we have seen the signal of MgO substrate. After etching we need to put samples in acetone or remover at the same with supersonic treatment for 4 ~ 5 min to remove the left resist. Then we need to repeat the process of lithography for Ti/Au deposition. The thickness of Ti and Au is 5 and 80 nm respectively, the schematic of device is shown in Figure 1.8a.

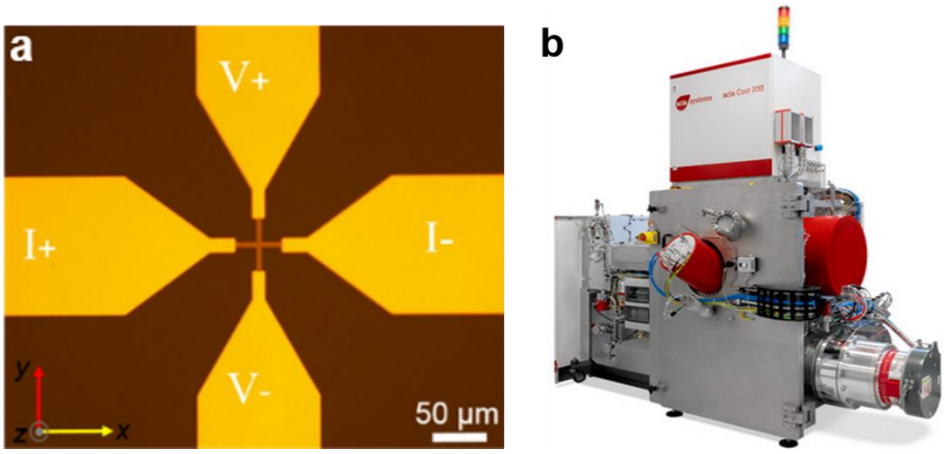

Figure 1.8 (a) Optical microscopy image of Hall bar device fabricated by lithography and ion-beam etching. (b) Scia Coat 200 Ion Beam Sputtering machine.

1.4 Electronic transport measurement setup

All the electrical measurement including conventional Hall effect measurement, electrical current induced magnetization switching experiments, and harmonic Hall measurements of the devices we done at physical property measurement system (PPMS) produced by Quantum Design company and the probe station produced by Lake shore company. The spin-torque ferromagnetic resonance measurement is a home-made measurement system. For conventional Hall measurement, a set of DC current source (Keithley 6221) and nanovoltmeter (Keithley 2182a) is used. The whole set up for electrical properties measurement of thin film is shown in Figure 1.9 a, b, and c. To perform electrical switching experiment with millisecond and nanosecond pulse, a multifunctional sourcemeter (Keithley 2635B) and Advan Tech pulse generator is used. Harmonic Hall voltage was measured by Zurich lock-in Amplifier (MFLI 500 kHz/5 MHz).

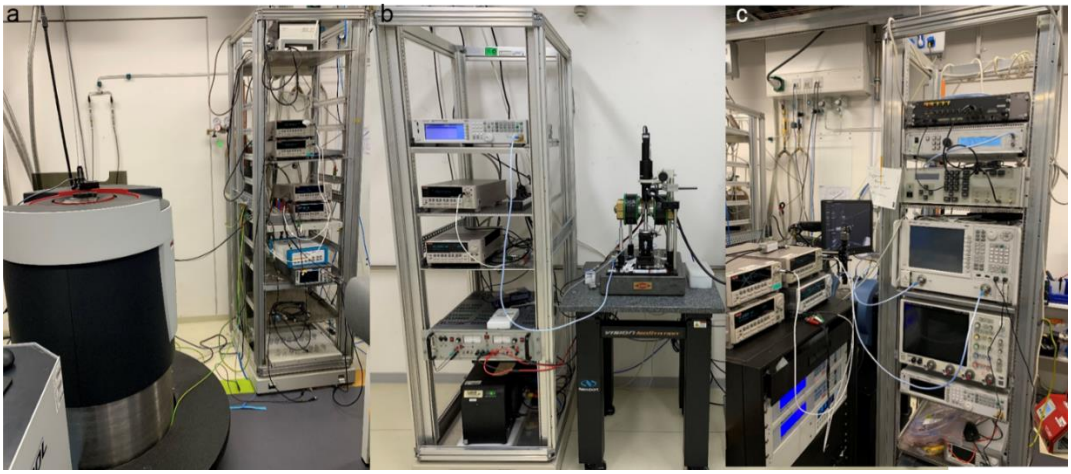

Figure 1.9 (a) 14T PPMS equipment, (b) Spin-torque ferromagnetic resonance facility, and (c) in-plane probe station.

1.5 Domain wall motion measurement setup

Zeiss Kerr optical microscopy in differential mode is used to monitor the position of the DW along the nanowire in response to a series of current pulses. The sensitivity of this technique is sufficient to detect the motion of single DWs in nanowires as narrow as ~ 100 nm. Images are took after a fixed number of current pulses chosen such that the DW has moved by a significant distance, typically ~ 1-2 μm. The Kerr microscope image is shown in Figure 1.10a.

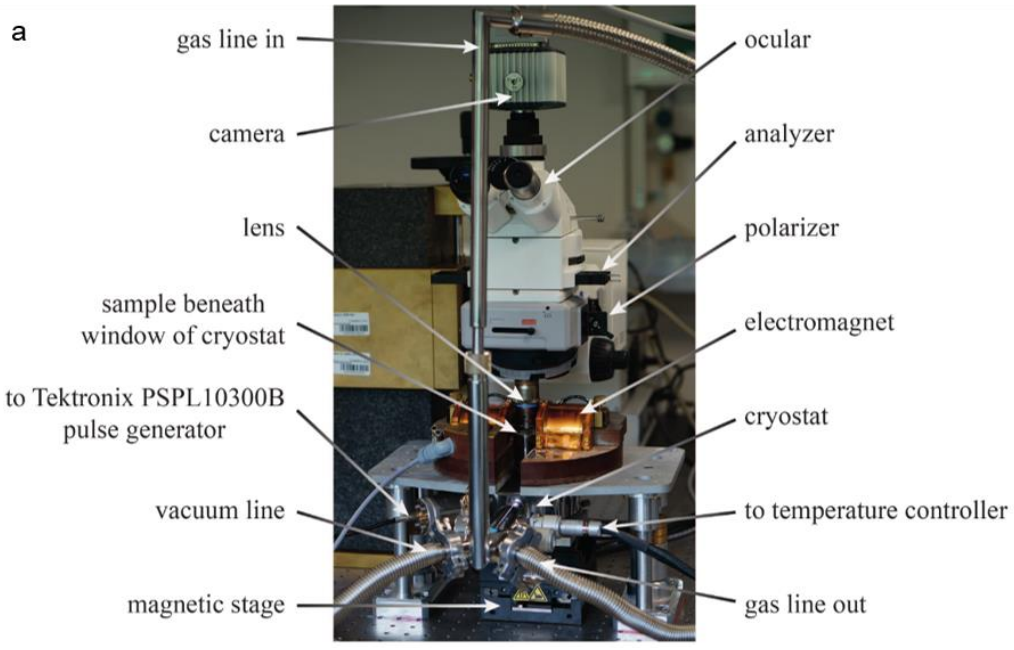

Figure 1.10 (a) Temperature variable Kerr microscope setup.

1.6 Ion-milling machine

The ion-polishing machine is used to prepare cross-section and plane-view lamella for investigating the crystal and magnetic domain structure under TEM and LTEM mode. The ion-polishing machine has *x-y* stage permits alignment of argon beams to region of interest on the sample. It has advantage of improved collimated beam provides useable voltages as low as 100 volts for rapid and damage free preparation of FIB lamella.

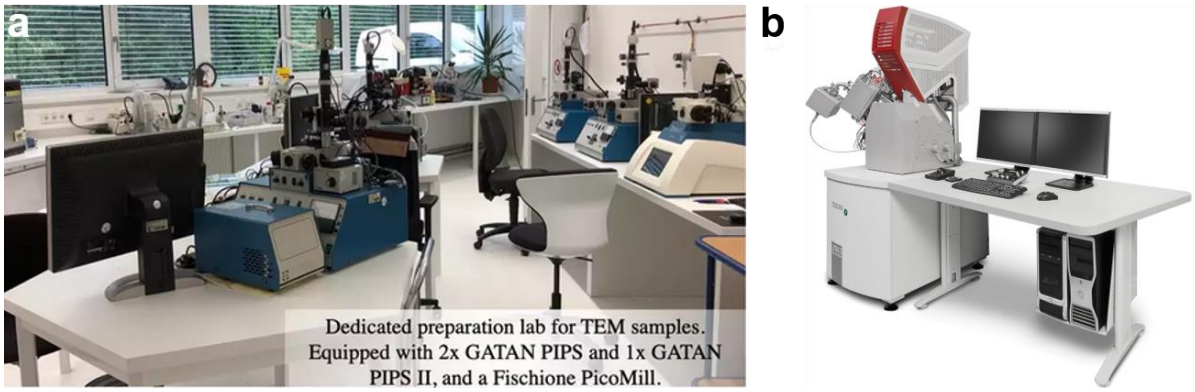

Figure 1.11 (a) Argon-ion milling machine. (b) Focused-ion beam milling machine.

1.7 JEOL High resolution transmission electron microscopy

JEM-ARM300F GRAND ARM is an Atomic Resolution Electron Microscope offering a maximum accelerating voltage of 300 kV, and equipped with JEOL's own Cs Corrections. This instrument guarantees an unprecedented STEM-HAADF image resolution of 58 pm. In the Lorentz mode, however, we observe the magnetic domains by tuning the objective lense (OL) off and manually increasing the magnetic fields continuously by adjusting the OL current in so-called "free lens-control mode" or by using the specially designed JEOL dedicated Lorentz TEM where the residual magnetic field is ignorable at around 4 Oe to 10 Oe.

The principle of magnetic domain images obtained from Lorentz TEM or Lorentz mode of standard TEM is based on the electron beam passing through the magnetic material, where the in-plane magnetization induces a Lorentz force normal to both the magnetization and the perpendicular electron beam. The electron beam is deflected by *L*orentz force, F_L, as a result of the presence of an electrostatic field *E* and/ or a magnetic field *B* within and around the sample:

$$F_L = -e\,(E + v \times \boldsymbol{B}) \qquad (1)$$

In Lorentz TEM, only the in-plane components of the magnetic induction B_{xy} contribute to the deflection angle, which is typically much smaller than the Bragg angle of a few milliradians.

Figure 1.12 (a) High resolution transmission electron microscope.

1.8 Magnetic force microscopy

MFM is a type of atomic force microscope. By using a tip that is magnetized, thereby interacting with the stray field created by the magnetization of the sample, the magnetization can be measured with a scanning probe microscopy technique with a spatial resolution of the order of < 40 nm. MFM experiments were carried out in a commercial variable temperature system in our group, as shown in Figure 1.13a, equipped with a 2D vector superconducting magnet, which can generate a magnetic field of 3 T in plane and 9 T perpendicular to the sample surface. Before measurements, the tip magnetization needs to be initialized by a small permanent magnet. The topographic and magnetic contrast can be simultaneously measured. Typically, the tip first interacts with the sample in the tapping mode to acquire the surface topography and is then lifted to some distance, e.g. 80 nm, above the sample surface to record the magnetic texture. We use the phase-detection technique.

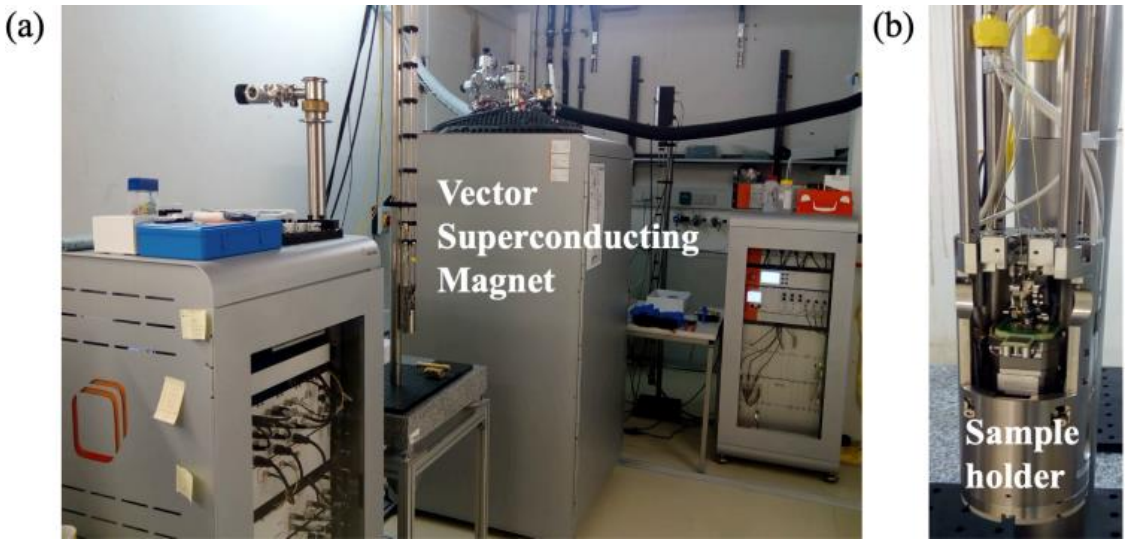

Figure 1.13 MFM setup with model AttoLiquid MFMF I from the company Attocube. (a) Chambers for low temperature measurement and superconductor vector magnet and (b) Sample holder with the magnetic tip and piezo stage.

1.9 Current-in-plane tunneling (CIPT) setup and measurements

The CIPTech® determines the critically important tunneling resistance and magneto-resistance (RA & MR) directly on blanket magnetic tunnel junction (MTJ) stacks for MRAM (Magnetic Random Access Memory) and magnetic recording read head applications. The tool combines IBM and Infineon Technologies proprietary Current In-Plane Tunneling (CIPT) technology licensed from IBM and Infineon Technologies with CAPRES multi-point micro-probing methods. CIPT is used to process data obtained from a multi-point measurement made with a CAPRES M12PP Micro Twelve-Point Probe, enabling MR & RA to be determined directly on blanket films.

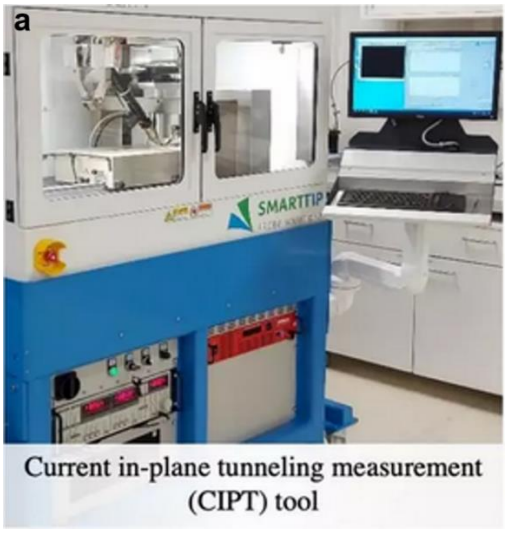

Figure 1.14 Current in-plane tunneling measurement tool setup.

2. Spin Hall effects of 5*d* transition metal – aluminum (M_xAl_{100-x}) alloy thin films

2.1 M_xAl_{100-x} alloys thin films growth

We grow M_xAl_{100-x} thin films (M = Ta, W, Re, Os, Ir, Pt, and Au**)** by co-sputtering technique from heavy metal targets and Al target. In order to change *x* from 0 to 100, we tune the sputtering power of heavy metal targets .with sputtering power of Al target fixed at 95 Walt. The vacuum of main sputtering chamber is lower than 10^{-8} Torr before sputtering. The sputtering gas that we use is Argon and sputtering pressure is 3 mTorr. We grew M_xAl_{100-x} thin films on top of 10 × 10 mm (001) orientation MgO substrates with 2 nm MgO as buffer layer. We use insulating MgO capping layer to protect M_xAl_{100-x} thin films from oxidation. The schematics of thin films structure is shown in Figure 2.1.a. The sputtering time is 600 seconds for the growth of M_xAl_{100-x} alloys in order to calibrate their thickness, crystal structure and electric properties.

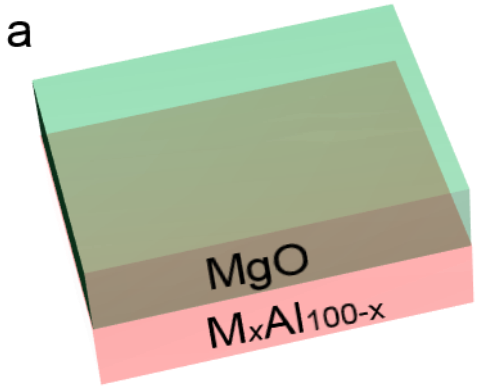

Figure 2.1a Schematic of M_xAl_{100-x} alloy thin films protected with MgO capping layer.

2.2 *X*-ray diffraction results of M_xAl_{100-x} alloy thin films

The composition of M_xAl_{100-x} alloys are calibrated by Rutherford backscattering spectroscopy in a range of 10 × 10 mm with three sites. The XRD experiments were carried out with a four-circle diffractometer using Cu-K-α1 radiation and employing a two-dimensional pixel detector. It is shown in Figure 2.2a, all Ta_xAl_{100-x} alloys grown on top of MgO substrates displays poor crystallinity degree with amorphous and/or polycrystal structure, which is mostly because of highly lattice mismatching between Ta_xAl_{100-x} thin film and MgO substrate. We can see from Figure 2.2b, when *x* increases to 53 atom %, W_xAl_{100-x} films display typical (002) XRD peak at 58^o, which belong to α-W phase. Furthermore, the position of (002) peak slightly shift to the left, which suggests the increase of out-of-plane lattice parameter (*c*) according to Bragg's law

2 $d\ sin(\theta) = n\ \lambda$. In Figure 2.2c, we have observed typical (100) and (102) peaks of Re in Re_xAl_{100-x} compounds.

It is shown in Figure 2.2d, in Os_xAl_{100-x} alloy thin films, no XRD peak is observed when x is lower than 33 atom %, which suggests its amorphous crystal structure. Furthermore, when $x \geq$ 33 atom %, both (001) and (002) peaks are found in Os_xAl_{100-x} compounds. Both (001) and (002) peaks gradually shift to the left with x increasing, which indicates increase of c. The tetragonal distortion Os_xAl_{100-x} thin film has been successively grown on top of MgO substrate with $L1_0$ structure. However, the XRD peaks gradually collapsed as x increases up to 60 atom %. This suggests the crystal lattice structure of $L1_0$ is broken by large strain from tetragonal distorted.

We can see from the phase diagram of Ir_xAl_{100-x} alloys in Figure 2.2e and f, no X-ray peak is found when $x < 30$ atom %, which suggests their amorphous and / or polycrystal structure. And, in the range of 33 atom % $< x <$ 61 atom %, both (001) and (002) XRD peaks of Ir_xAl_{100-x} thin films gradually shift to the left, which suggests the increase of c. Tetragonal distortion of Ir_xAl_{100-x} alloys increases a lot with x varying from 33 to 61 atom%. Furthermore, cubic iridium phase is dominated in Ir_xAl_{100-x} alloy with $x >$ 61 atom %, which suggests aluminum atoms randomly inserted into iridium matrix.

It is shown in Figure 2.2g, XRD results suggest that the alloy is amorphous and/or polycrystal structure dominated when $x < 32$ atom % in Pt_xAl_{100-x} compounds. When x varies from 32 to 50 atom %, we have found both (001) and (002) X-ray peaks shifting to left, which indicates the tetragonal distortion features in Pt_xAl_{100-x} alloy systems. Furthermore, Pt_3Al is the dominate phase in Pt_xAl_{100-x} alloys when $x > 50$ atom %.

Several distinct X-ray peaks of Au_xAl_{100-x} is shown in Figure 2.2h, (001) and (002) XRD peaks of CsCl-type Au_xAl_{100-x} is found, also there is (111) peak of pure cubic Au phase, therefore, the crystal structure of Au_xAl_{100-x} is a kind of mixture with different phase. The c lattice parameter systematically increases with increasing x within the crystalline phase region, as shown in Figure 2.3a. For example, for Ir_xAl_{100-x}, c increases by ~ 10% as x increasing from 33 to 61 atom %, consistent with an enhanced tetragonality.

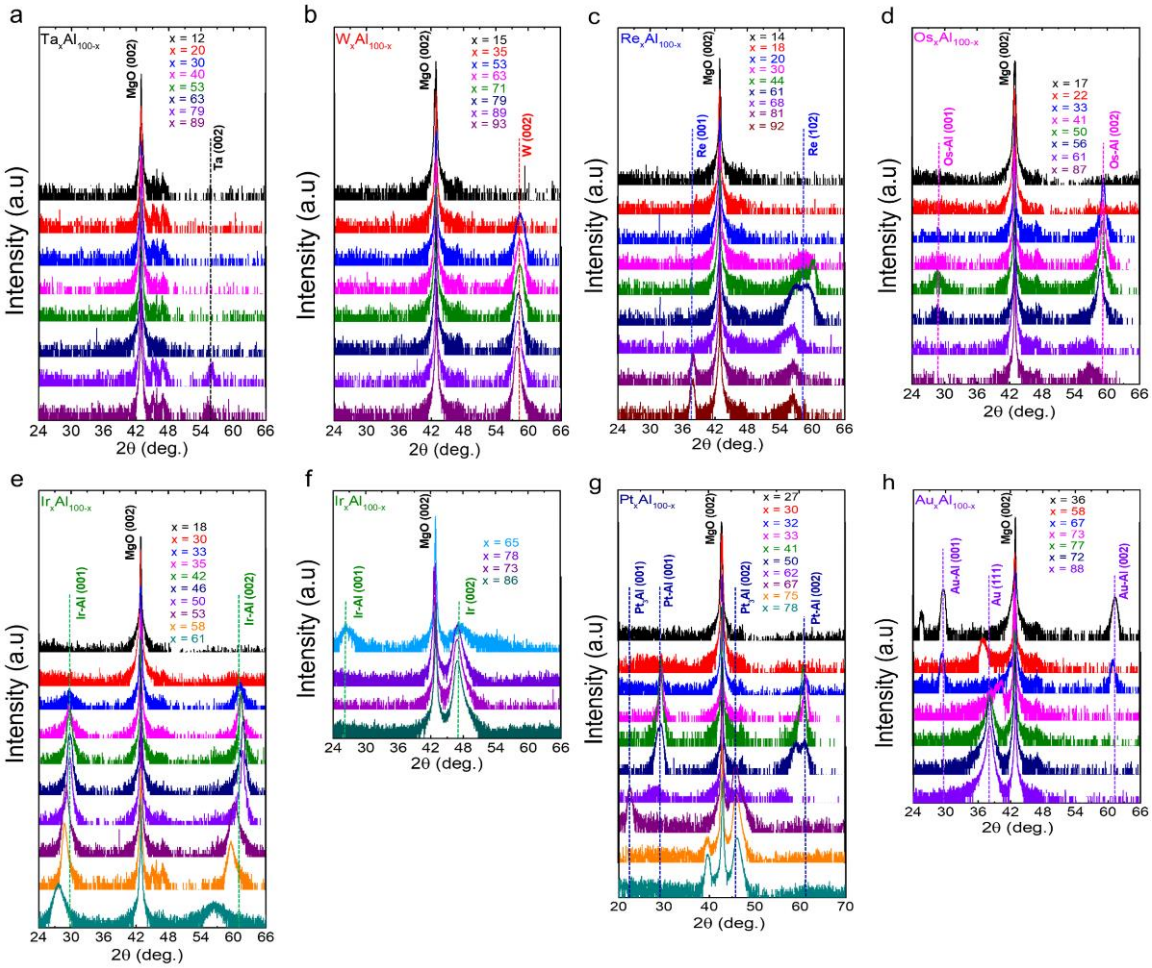

Figure 2.2 (a – h) XRD measurements of M_xAl_{100-x} compounds, 2θ -ω scan specular scan.

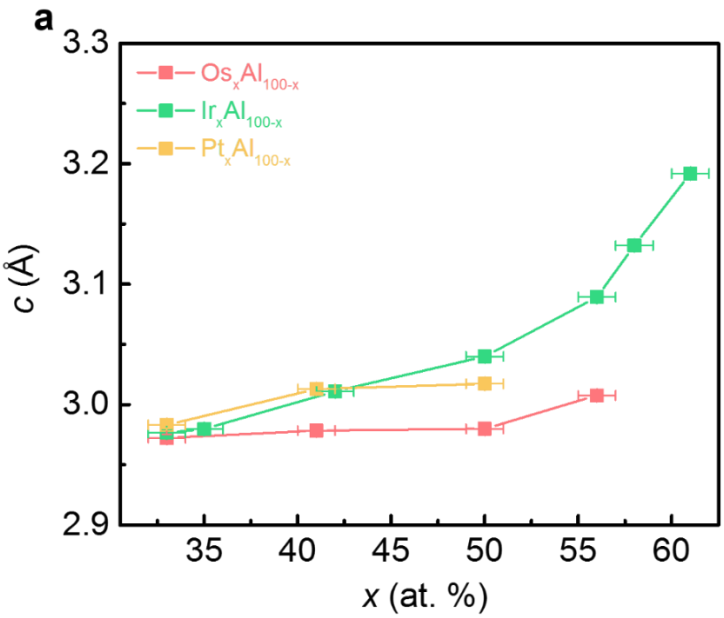

Figure 2.3 (a) Out-of-plane lattice parameter c as a function of x for Os_xAl_{100-x}, Ir_xAl_{100-x} and Pt_xAl_{100-x} with the $L1_0$ structure.

2.3 Sheet resistivity of M_xAl_{100-x} alloy thin films

Sheet resistances R_S of grown films are measured by four-point probe method, from which ρ is obtained from the relation $\rho = R_s \times t$ where t the thickness of film. It is found that the ρ shows a strong correlation with the crystal structures. In all cases where a crystalline CsCl-type structure is formed at intermediate values of *x*, a resistivity maximum is observed at the onset of the long-range order, which is identified at *x* lying in the range of about *x* = 20 - 40 atom %, depending on *M* (see Figure 2.4 a and b). This concentration likely corresponds to a "percolation limit" where the metal number density exceeds a critical value where the average *M*-*M* distance and interaction becomes large enough to establish a long-range ordered structure [41, 42]. This coincides with the resistivity maximum as the crystalline domains are still small and the number of grain boundaries is large. The maximum value of $\rho \sim 1100\ \mu\Omega\ \text{cm}$ is observed for $Os_{22}Al_{78}$. The peak values of the resistivity are considerably higher than the end members in each M_xAl_{100-x} alloy thin film (~ 3 μΩ cm for Al and Au and 5 to 20 μΩ cm for the other *M*). Beyond this critical concentration the resistivity decreases as the size of the coherently scattering domains and the degree of chemical ordering increases. More important is that, the maximum resistivity (ρ_{max}) of M_xAl_{100-x} alloy thin films heavily depend on 5*d* band electron number and atomic number Z, which displays in Figure 2.4 c.

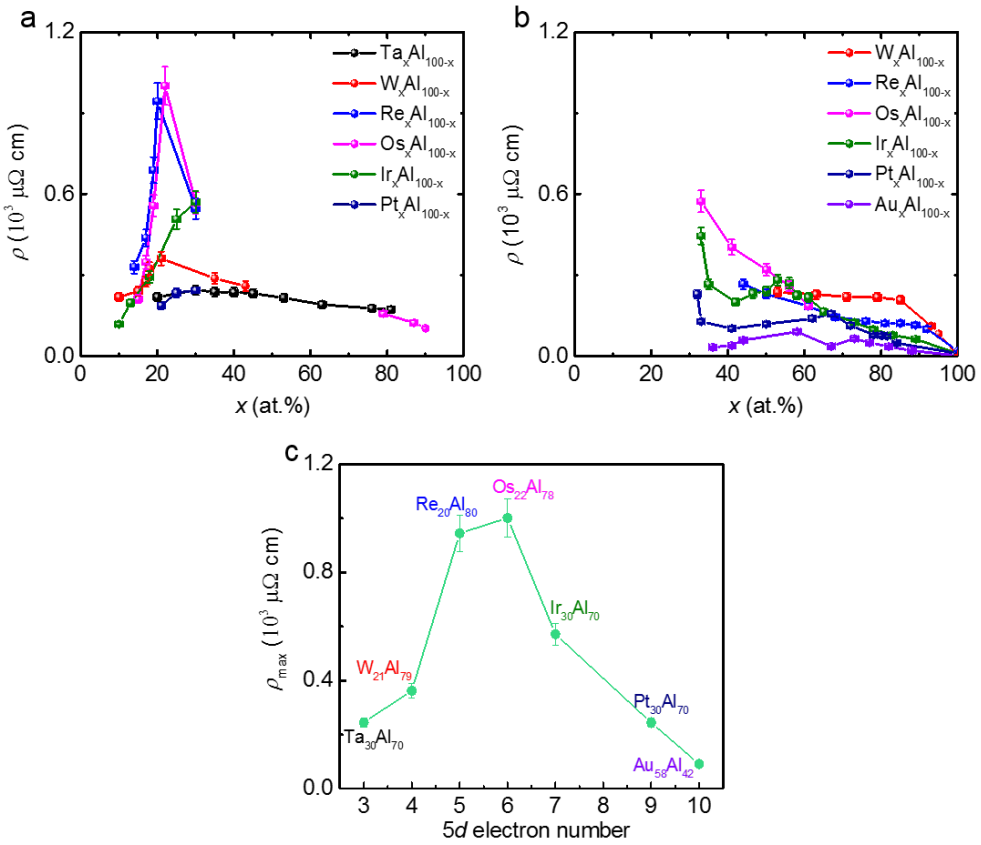

Figure 2.4 (a, b) Sheet resistivity of M_xAl_{100-x} with a poorly crystalline phase (a), and a highly textured crystalline phase (b) as a function of x, respectively. (c) Maximum resistivity for M_xAl_{100-x} as a function of 5d electron number.

2.4 High resolution cross section transmission electron microscopy images of M_xAl_{100-x} thin films

Figure 2.5 a – l show the high resolution cross section transmission electron microscopy images of IrAl, OsAl and PtAl alloy thin films. All these $L1_0$ M_xAl_{100-x} alloy thin film shows the high degree of crystallinity with the feature of monocrystalline from the result of selected area electron diffraction. The elements distribute uniformly in the whole films without grain boundary precipitation. Furthermore, we can confirm that all $L1_0$ M_xAl_{100-x} alloy thin films grow with 45° rotation along with [001] orientation MgO substrate. The tetragonal distortion of these $L1_0$ M_xAl_{100-x} is approved by both SAED and STEM images from lattice structure.

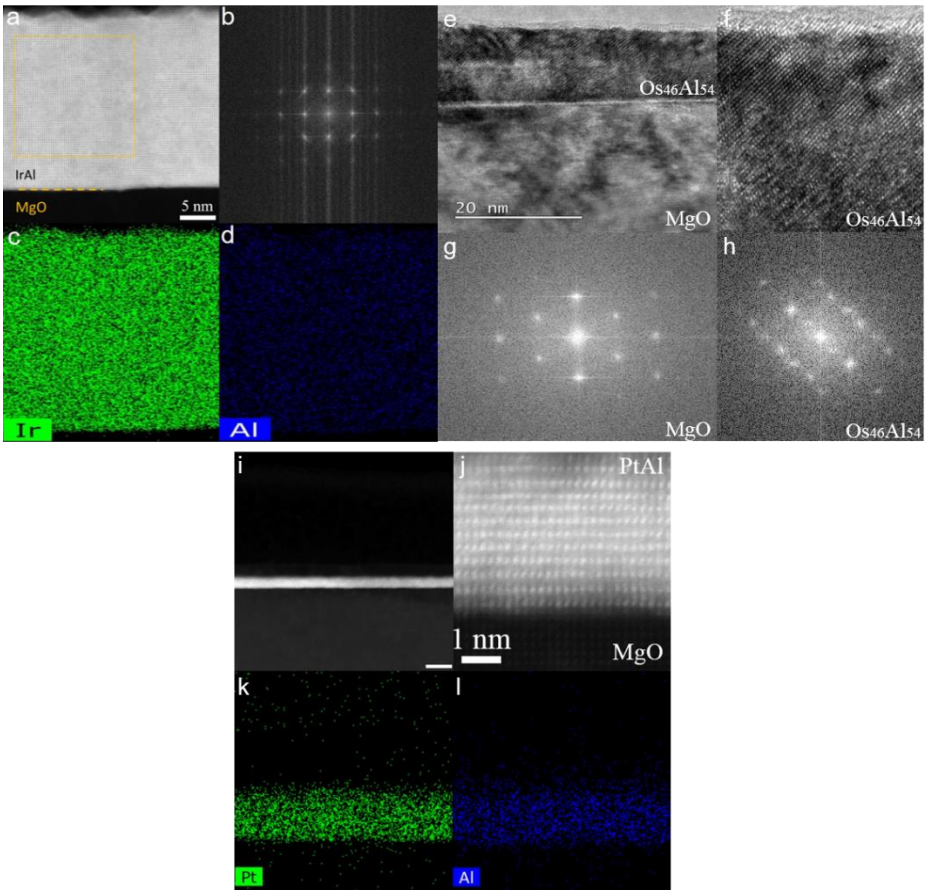

Figure 2.5 (a) HR-TEM image and (b) SAED, (c) and (d) EDX element mapping of IrAl film. (e), (f) HR-TEM image and (g) and (h) SAED of MgO substrate and OsAl film (i), (j) HR-TEM image and (k) and (l) SAED of PtAl film.

2.5 Spin Torque Ferromagnetic Resonance (ST-FMR) measurements for M_xAl_{100-x} / $Co_{20}Fe_{60}B_{20}$ bilayer samples

2.5.1 Introduction and mechanisms of ST-FMR

Conventionally, for the spin Hall angle measurement we need bilayer structures such as spin Hall effect layer adjacent with in-plane magnet such as $Co_{20}Fe_{60}B_{20}$ or $Co_{40}Fe_{40}B_{20}$ and Permalloy ($Ni_{89}Fe_{11}$) layer. The long stripe for measurements is from blanket films after etching. Gigahertz radio - frequency current (I_{rf}) is input into devices. I_{rf} exerts an oscillatory spin torque on the free magnetic layer. The spin torque excites the magnetization dynamics of the free layer and causes the resistance to oscillate. A D.C voltage arises from the mixing of I_{rf} and oscillating resistance of bilayers. The resonance features enable us to quantify the spin current absorbed by magnetic free layer [4]. The schematic of measurement set up is shown in Figure 2.6 a. There are two kinds of spin Hall angle analysis method, including the shape analysis of D.C voltage curve and the line-width measurements between peaks of DC voltage at different gigahertz. In our measurements, we use 60 Å

$Co_{20}Fe_{60}B_{20}$ (CFB) layer as free layer and 43 Å M_xAl_{100-x} alloy thin films as spin Hall effect layer then 50 Å TaN as capping layer to protect samples from oxidation.

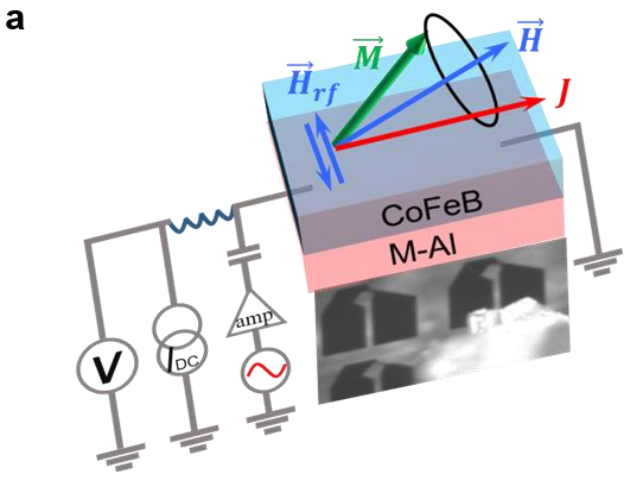

Figure 2.6 (a) Illustration of the ST-FMR experimental setup.

2.5.2 ST-FMR line-shape method

Figure 2.7 a - g shows the plot of V_{mix} versus H_{ext} for 43 M_xAl_{100-x} / 60 CFB bilayer samples, which displays the large spin Hall angle at different excitation frequencies. The ST-FMR spectra is fitted by a Lorentzian function with symmetric and antisymmetric components [4, 13] according to,

$$V_{mix} = c\left[V_S \frac{\Delta^2}{\Delta^2 + (H_{ext} - H_0)^2} + V_A \frac{\Delta\,(H_{ext} - H_0)}{\Delta^2 + (H_{ext} - H_0)^2}\right] \qquad (1)$$

where c is a fitting constant, and V_S and V_A are the amplitudes of symmetric and antisymmetric components respectively, H_0 is the resonant field and Δ is the linewidth of the resonance peak. Resonant field increases with excitation frequency, as expected from the Kittel model, whose fit to the data in Figure 2.8 a - g allows the determination of the effective magnetization (M_{eff}), according to the formula,

$$f = \frac{\gamma \mu_0}{2\pi} \sqrt{H_0(H_0 + 4\pi M_{eff})} \qquad (2)$$

where γ represents the gyromagnetic ratio 2.16 and μ_0 represents the vacuum permeability. The extracted values M_{eff} and the saturation magnetization (M_s) of CFB films measured using SQUID-VSM.

Based on frequency-dependent line-shape analysis by comparing the V_S and V_A, we can extract effective spin Hall angle θ_{ls} according to the formula,

$$\theta_{ls} = \frac{J_s}{J_c} = \frac{V_s}{V_A} \frac{e\mu_0 M_s t d}{\hbar} \sqrt{\left(1 + \frac{4\pi M_{eff}}{H_0}\right)} \qquad (3)$$

where e is the electron charge , $\hbar$ represents Planck's constant, t and d is the thickness of FM and NM (d) layers, respectively.

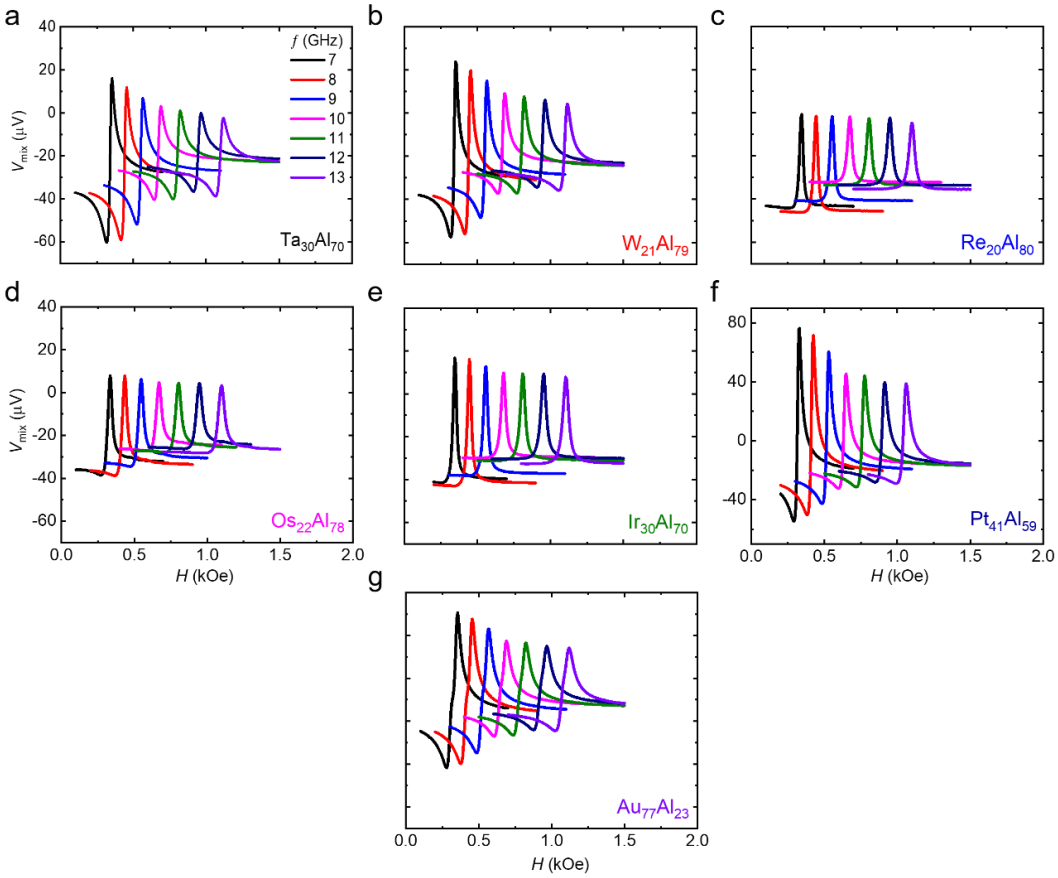

Figure 2.7 (a – g) ST-FMR spectra measured in the frequency range from 7 to 13 GHz for M_xAl_{100-x} / CFB bilayer samples, which shows the largest spin Hall angle at x.

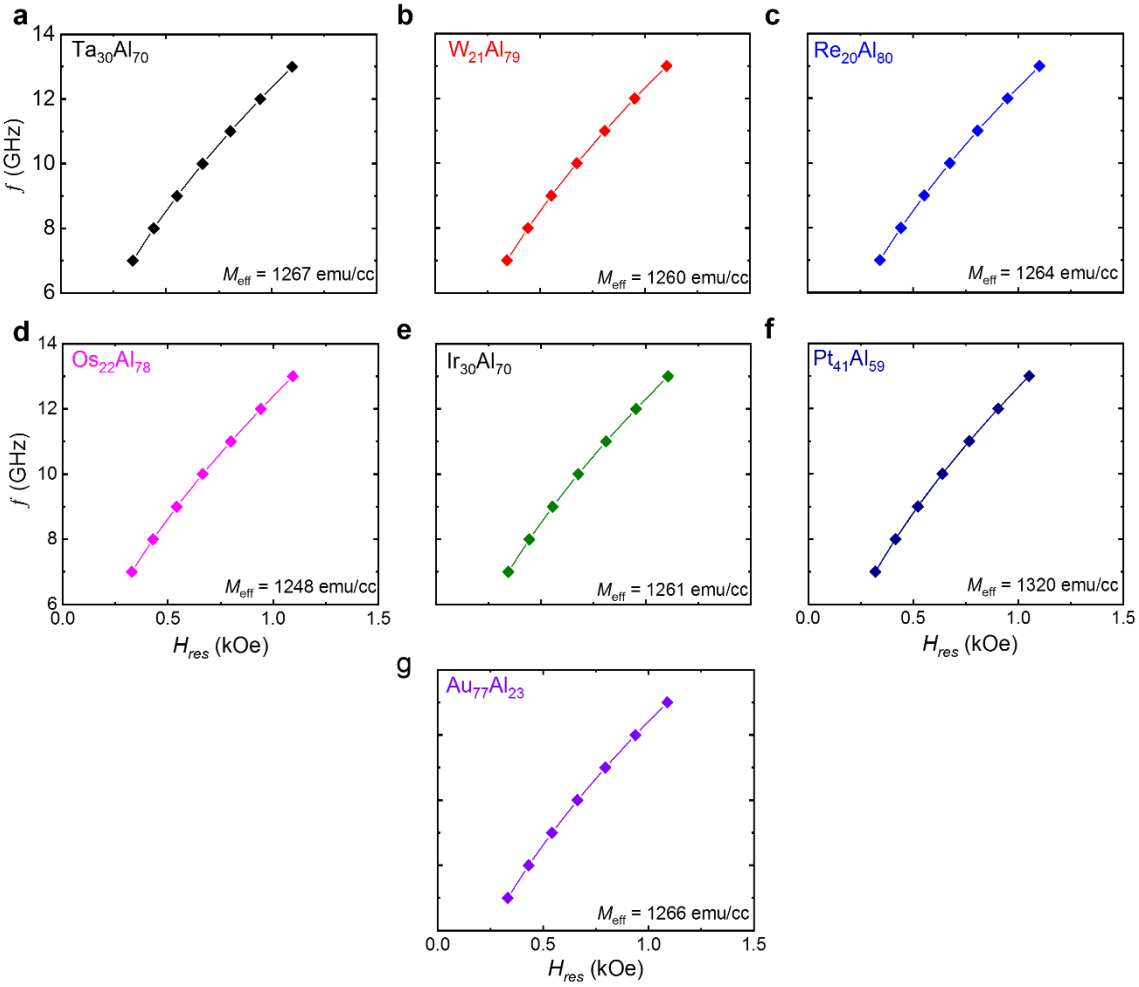

Figure 2.8 (a – g) Plot of frequency versus resonant field for M_xAl_{100-x} / CFB bilayer samples, which shows the largest spin Hall angle at *x*.

2.5.3 ST-FMR line-width method

As discussed, when a DC current flows through M_xAl_{100-x} alloy layer, the charge-to-spin conversion processes will generate a damping-like (DL) spin-orbit effective field. This, in turn exerts an additional DL-SOT on magnetization of CFB layer, which will modify linearly its FMR linewidth according to the equation,

$$\Delta = \frac{2\pi f}{\gamma}\left(\alpha + \frac{\sin\varphi}{(H_{ext}+2\pi M_{eff})\mu_0 M_S t}\frac{\hbar}{2e}J_S\right) \quad (4)$$

where φ is the angle between direction of DC current and magnetization of CFB layer.

We can obtain the ratio of charge-to-spin current density from the slope $\delta\Delta$ / δI_{DC} by using equation (5) and (6), which is shown in Figure 2.9 a - g,

$$\theta_{SH} = \frac{\delta\Delta/\delta I_{d.c.}}{\frac{2\pi f}{\gamma}\left(\frac{\sin\varphi}{(H_{ext}+2\pi M_{eff})\mu_0 M_S t}\frac{\hbar}{2e}\right)}\frac{R_{CFB}+R_{MAl}}{R_{CFB}}A_c \quad (5)$$

$$\theta_{SH} = \frac{\delta\Delta/\delta I_{d.c.}}{\frac{2\pi f}{\gamma}\left(\frac{\sin\varphi}{\left(H_{ext}+2\pi M_{eff}\right)\mu_0 M_S t}\frac{\hbar}{2e}\right)}\left(1+\frac{\rho_{MAl}\,t_{CFB}}{\rho_{CoFeB}\,t_{MAl}}\right)A_c \qquad (6)$$

The dimension of ST-FMR device being used is 25 μm width with 50 μm length. Here R_{CFB} and R_{MAl} are resistances of CFB and M_xAl_{100-x} layer, respectively, and A_c is the cross-section area of ST-FMR device. The resistivity of M_xAl_{100-x} thin films is shown in Figure 2.3a and b, saturation magnetization of 60 Å CFB layer is 1440 emu/cc. And the resistivity of CFB and TaN layer is shown as below:

ρ ($Co_{20}Fe_{60}B_{20}$) = 100 (μΩ cm)

ρ (TaN) = 1300 (μΩ cm)

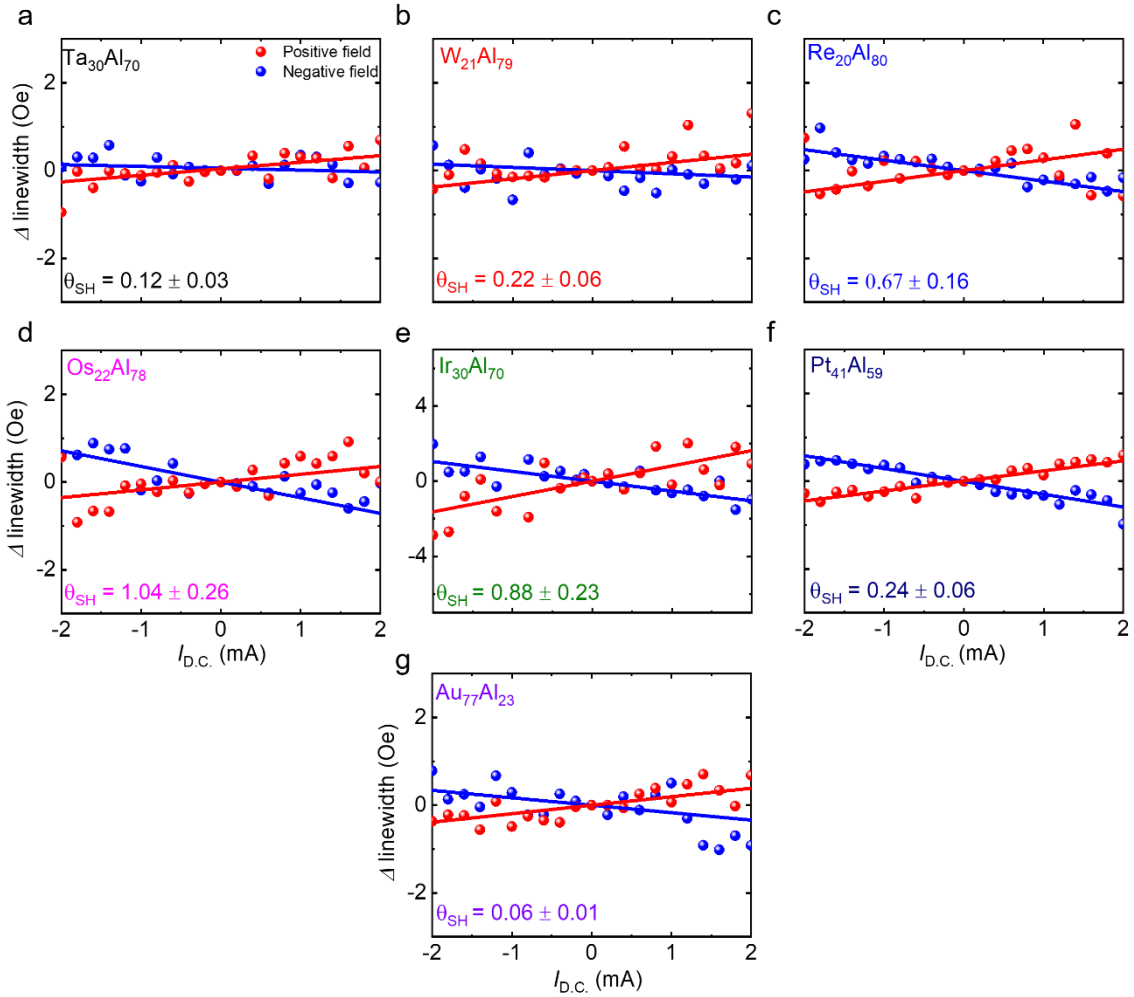

Figure 2.9 (a – g) Change of linewidth as a function of DC bias current applied during ST-FMR measurements at 9 GHz, with a linear fit to the broadening used to calculate effective SHA (θ_{SH}) in 43 M_xAl_{100-x} | 60 $Co_{20}Fe_{60}B_{20}$ bilayer samples.

2.5.4 Spin Hall effect from line-width analysis of M_xAl_{100-x} / $Co_{20}Fe_{60}B_{20}$ bilayer samples

According to the large resistivity of M_xAl_{100-x} alloy thin film and strong spin-orbit coupling from 5*d* transition metal components, we grew 60 Å CFB layer on top from a series of M_xAl_{100-x} thin films. We measure its line-shape curve with in-plane magnetic field from 0 to 2 kOe by patterned device. The radio-frequency current varies from 7 to 13 GHz with 20 dBm power. We calculate the effective spin Hall angle (θ_{SH}) in a series of M_xAl_{100-x} alloy thin films with D.C.-bias current varies from -2 to 2 mA at 9 GHz. We plot all spin Hall angles (θ_{SH}) as a function of *x* for M_xAl_{100-x} compounds in Figure 2.10 a - d. We separate the plot of θ_{SH} for M_xAl_{100-x} compounds into four regions according to the number of electrons in 5*d* band from transition metal components. In Figure 2.10 a, the number of electrons in 5*d* band is less than 5. The magnitude and sign of θ_{SH} is highly dependent on the *x*. The sign of θ_{SH} changes from positive to negative with $x > 50$ atom %. θ_{SH} shows the peak value in the range of $20 < x < 40$ atom %. Furthermore, θ_{SH} of W_xAl_{100-x} thin film is larger compare with Ta_xAl_{100-x} with same *x*, which is related to *Z* atomic number.

The θ_{SH} of Re_xAl_{100-x} dramatically increases with a peak value at $Re_{20}Al_{80}$, which is up to 0.67 ± 0.16. Then θ_{SH} gradually decreases with *x* increasing without sign changing. We can conclude *Z* atomic number and unpaired electron in 5*d* band play an important role in determining θ_{SH}. The number of electron in 5*d* band is more than half filling in Os_xAl_{100-x}, Ir_xAl_{100-x} and Pt_xAl_{100-x} thin films. The magnitude of *x*, which is correlated with peak value of θ_{SH} gradually shift to right with Z number increasing in the range of 20 ~ 40 atom %. θ_{SH} is up to ~ 1 for $Os_{22}Al_{78}$. The effective θ_{SH} for Au_xAl_{100-x} is much smaller compare with that in other M_xAl_{100-x} alloys. The number of electron in 5*d* band for Au_xAl_{100-x} alloy is 10 with full filling. Furthermore, the largest θ_{SH} for M_xAl_{100-x} lies in the range of $20 < x < 40$ atom %, which is the boundary between disordered and ordered crystalline. The strong spin-orbit interaction of 5*d* transition metal *M* increases scattering of electrons. The transition from crystalline disordered to ordering state decreases the electron mean free path *l*. Short electron mean free path increases the probability of electron scattering. Therefore, the number of electron in 5*d* band and crystalline ordered state make crucial contribution to the sign and magnitude of θ_{SH}.

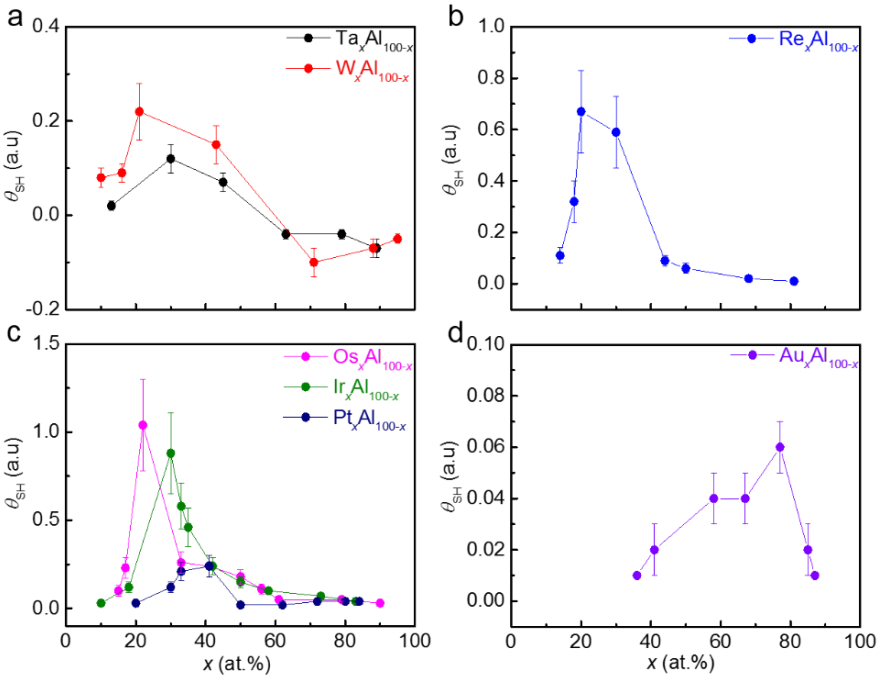

Figure 2.10 (a – d) Plot of spin Hall angle versus x for M_xAl_{100-x} alloy thin films

The spin Hall conductivity (σ_{SH}) is defined as $\sigma_{SH} = \theta_{SH} \times \sigma$, where σ is the conductivity of M_xAl_{100-x} alloy thin films. σ is converted from its sheet resistivity. The spin Hall conductivity is used to evaluate the energy efficiency of charge current injected into spin Hall effect materials. The ratio of x for peak value of σ_{SH} in M_xAl_{100-x} alloy also lies in the range of 20 ~ 40 atom %. However, the magnitude of x increases compare with that in the plot of θ_{SH} versus x. Pt_xAl_{100-x} alloys show the giant spin Hall conductivity ~ 2.34 ± 0.61 (10^5 $\hbar/2e$ Ω^{-1} m^{-1}) with x ~ 41 atom %. This results is comparable with previously reported value of 2.0 (10^5 $\hbar/2e$ Ω^{-1} m^{-1}) from $Pt_{80}Al_{20}$. Although θ_{SH} of Au_xAl_{100-x} alloy is much smaller compare with other M_xAl_{100-x} alloys, σ_{SH} is considerable compare with Ta_xAl_{100-x} and W_xAl_{100-x} compounds. Both spin Hall angle and conductivity determine the performance of M_xAl_{100-x} alloys used as spin-orbit torque sources.

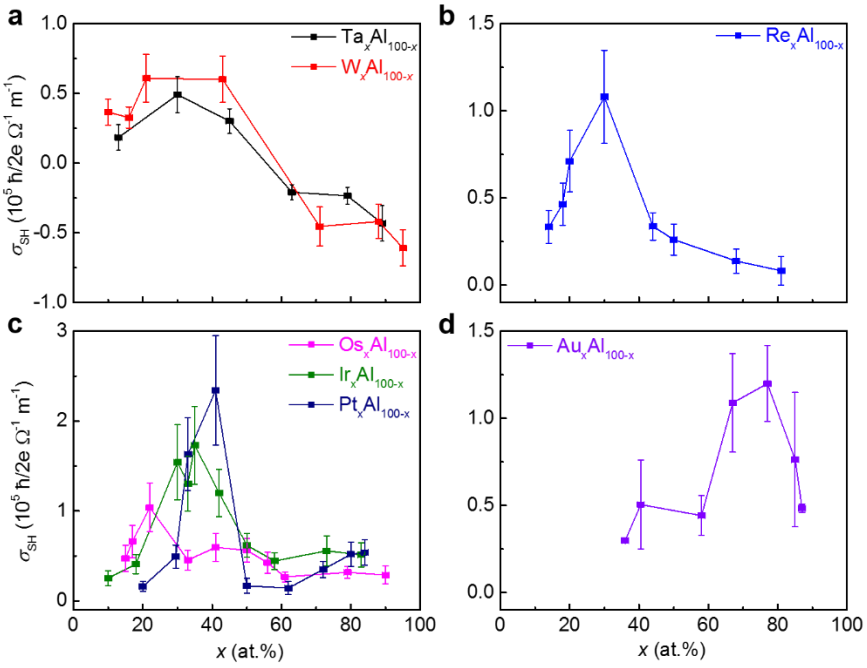

Figure 2.11 (a – d) Plot of spin Hall conductivity versus *x* for M_xAl_{100-x} alloy thin films.

In consideration of magnetization switching of unit ferromagnets by spin-orbit toques, the power consumption factor (ρ / θ_{SH}^2) is used to evaluate the performance of spin Hall effect materials [43]. Large ratio of ρ / θ_{SH}^2 indicates high power consumption for magnetization switching of unit ferromagnets. ρ / θ_{SH}^2 for Ir_xAl_{100-x} is minimum ~ 737 ± 265 (μΩ cm) compare with other M_xAl_{100-x} alloy thin films Figure 2.12c. Although σ_{SH} and θ_{SH} of Ir_xAl_{100-x} is not best in M_xAl_{100-x} alloys system, it shows the minimum power consumption factor. Furthermore, the spin Hall effect of M_xAl_{100-x} alloys is strongly correlated with scattering of electrons, *Z* atomic number and the number of electrons in 5*d* band of transition metal *M*.

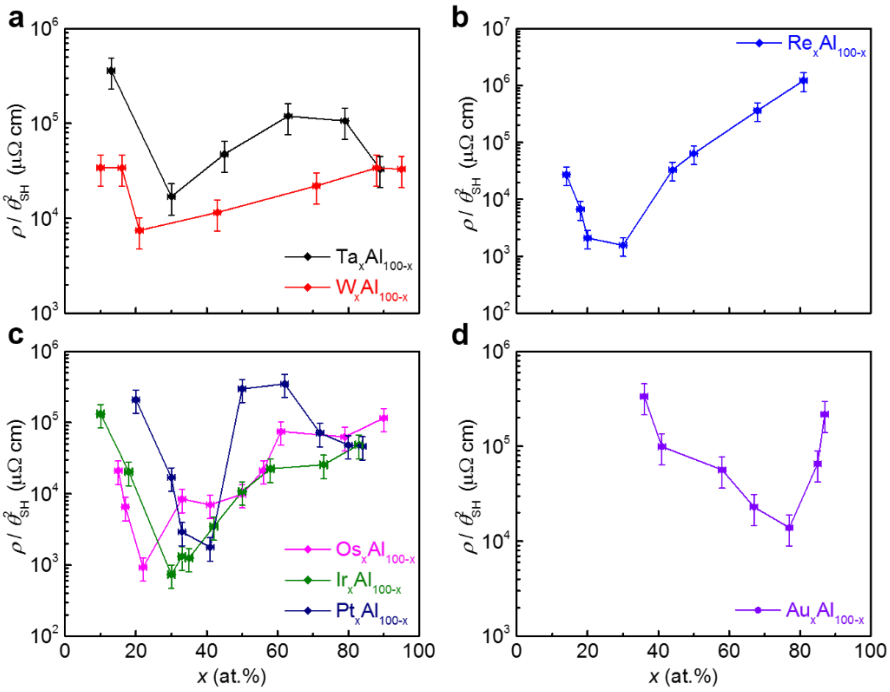

Figure 2.12 (a – d) Plot of power consumption factor versus x for M_xAl_{100-x} alloy thin films.

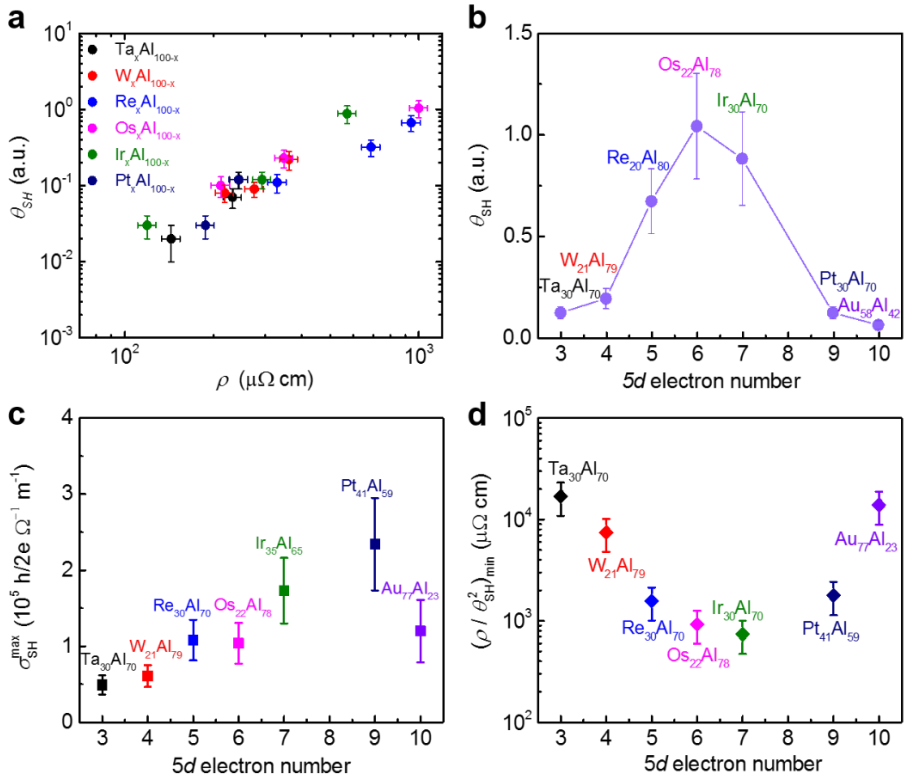

Figure 2.13 (a) Effective θ_{SH} as a function of resistivity for several M_xAl_{100-x} alloys which display poor crystallinity. (b) Maximum θ_{SH} for M_xAl_{100-x} as a function of the number of electrons in 5*d* band of M. (c) Maximum σ_{SH} in M_xAl_{100-x} | $Co_{20}Fe_{60}B_{20}$ samples as a function of the number of electrons in 5*d* band of M. (d) The minimum ratio of ρ/θ_{SH}^2 of M_xAl_{100-x} as a function of the number of electrons in 5*d* band of M.

2.6 Summary

Alloys of 5*d* elements with light elements are shown to give rise to very large spin Hall angles that exceed those of the best known non-topological materials to date. The largest values of ρ and θ_{SH} are observed to be ~1,000 μΩ cm and 1.04, respectively, in the alloy $Os_{22}Al_{78}$, while the largest value of σ_{SH} is found to be 2.34 (10^5 $\hbar$/2e $\Omega^{-1}m^{-1}$) in $Pt_{41}Al_{59}$. Moreover, these materials can be prepared by straightforward sputter deposition techniques, rather than molecular beam epitaxy methods, and, furthermore, act as a template for the growth of highly crystalline textured magnetic layers and heterostructures. An important finding is that the largest spin Hall angles are found at compositions that lie close to a phase boundary where the structure loses its crystalline texture, and, that the magnitude of the spin Hall angle scales with the resistivity of the 5*d*-alloy, clearly demonstrating the extrinsic origin of the spin Hall effect. Finally, the power consumption for spin orbit torque switching is minimized for the most resistive alloys. Our findings show that the giant SHE and spin-orbit torques in M_xAl_{100-x} alloys can provide an excellent platform for potential applications in diverse memory and logic devices with highly efficient interconversion of charge-to-spin currents and low power consumption.

3. [001] orientation synthetic antiferromagnets for racetrack memories

3.1 Introduction of racetrack memories

The racetrack memory described here consist an array of nanowires, which is composed by magnetic materials adjacent with strong spin-orbit coupling materials. These nanowires can be arranged horizontally or vertically on a silicon chip or some other special substrates, which is shown in Figure 3.1 A and B [38]. The magnetic domain walls formed at the boundary of magnetic domains with opposite magnetization pointing direction. The back and forth motion of domain walls can intersect with reading and writing elements, which is used as digital bits for information storage, as shown in Figure 3.1 C - E.

The injected current flowing through magnetic materials is spin polarized because of spin-dependent diffusive scattering. When the spin-polarized current passed through the domain walls, the spin angular momentum transferred from current to the magnetization moments. Thereby, the wall is moved by the torques from the transfer of spin angular momentum. As a result, the critical current density to drive the motion of domain walls and motion speed are key factors to evaluate their performance. In this chapter, we mainly focus on the performance improvement of racetrack memories from point of view of new materials with large spin Hall effect and special crystal orientation.

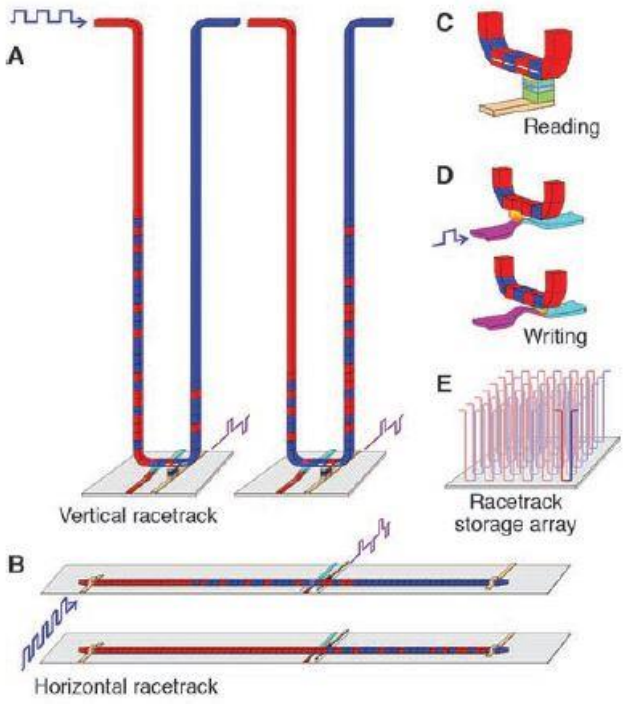

Figure 3.1 The racetrack is a ferromagnetic nanowire, with data encoded as a pattern of magnetic domains along a portion of the wire. Pulses of highly spin-polarized current move the entire pattern of DWs coherently along the length of the wire past read and write elements. The nanowire is approximately twice as long as the stored DW pattern, so the DWs may be moved in either direction. (**A**) A vertical-configuration racetrack offers the highest storage density by storing the pattern in a U-shaped nanowire normal to the plane of the substrate. The two cartoons show the magnetic patterns in the racetrack before and after the DWs have moved down one branch of the U, past the read and write elements, and then up the other branch. (**B**) A horizontal configuration uses a nanowire parallel to the plane of the substrate. (**C**) Reading data from the stored pattern is done by measuring the tunnel magnetoresistance of a magnetic tunnel junction element connected to the racetrack. (**D**) Writing data is accomplished, for example, by the fringing fields of a DW moved in a second ferromagnetic nanowire oriented at right angles to the storage nanowire. (**E**) Arrays of racetracks are built on a chip to enable high-density storage. This figure is from Ref [38].

3.2 The application of racetrack memories

The motion of domain walls along the nanowires can be read by the integrated magnetic tunnel junctions, thereby displaying the high and low tunneling resistance state, which is used to represent the status of “0” and “1” as the proto type for magnetic random-access magnetoresistance memories (MRAMs) [1,2,3,9]. Ultrafast reading and writing with pico and

nanosecond length current pulses is the advantage of MRAMs compare with other various types of memories such as flash memories, phase change memories, resistance change memories, et al. In the meantime, the integration of nanowires and nanometer pillars is also used as magnetic sensors, which shows promising application in the cars industry, medical health care et al.

3.3 The mechanism of domain wall motion

3.3.1 The concept of the domain wall

The domain walls is viewed as "transition regions" between the adjacent magnetic domains with opposite preferential magnetization. The domain walls itself has the width and internal structure which includes Bloch type and Néel type walls, as shown in Figure 3.2 a and b.

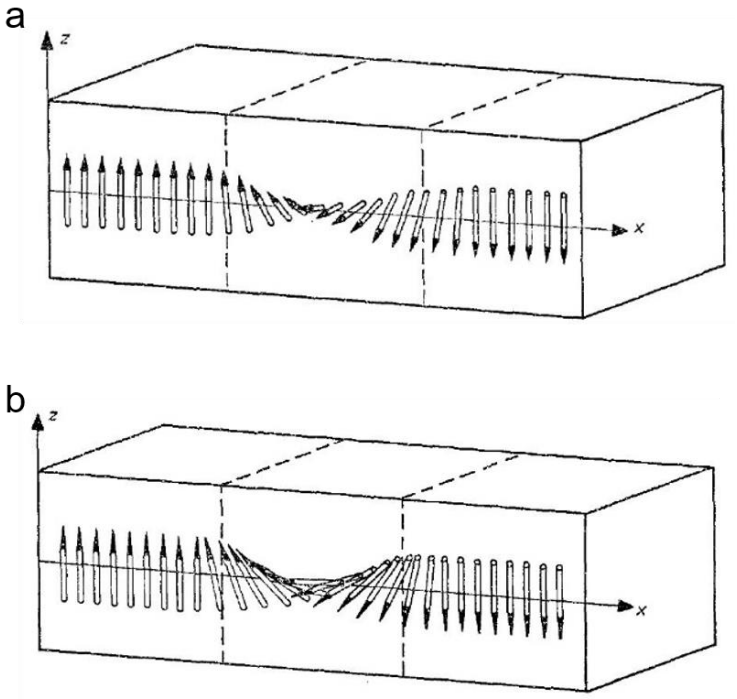

Figure 3.2 Schematics of magnetic moment pointing direction of Bloch type domain walls (a) and Néel type domain walls (b) along the projection axis.

The moment pointing direction changes from up to down with its direction gradually changes from *z* parallel direction to the normal to the *x* axis direction, which is the type of Bloch wall. The change of moment direction of Néel wall is always in the *x*-*z* plane. Both the Bloch and Néel wall has an additional freedom: the sense of rotation direction including clockwise or counterclockwise. Néel wall has a higher specific energy compare with Bloch wall because of the demagnetization field introduced by the free poles on the surface of the wall [30, 31].

3.3.2 Motion of the domain wall

The motion of magnetic domain walls is a kind of gyroscopic precession of the magnetic moment, which depends on the time in three dimensional space. The motion of magnetic domain walls is a description of magnetization vector responses to the torque acting on it, which can be described by Landau-Lifshitz-Gilbert-Slonczewski equation [30, 44]:

$$\dot{\boldsymbol{m}} = -\gamma \boldsymbol{m} \times \boldsymbol{H}_{eff} + \alpha \boldsymbol{m} \times \dot{\boldsymbol{m}} + \tau_{||} \frac{\boldsymbol{m} \times (\boldsymbol{x} \times \boldsymbol{m})}{|\boldsymbol{x} \times \boldsymbol{m}|} + \tau_{\perp} \frac{\boldsymbol{x} \times \boldsymbol{m}}{|\boldsymbol{x} \times \boldsymbol{m}|} \quad (1)$$

where α is the unitless damping parameter, $\tau_{\perp}$ and $\tau_{||}$ are driving torques, and x is the unit vector along the polarization of the current, $\boldsymbol{m} = \boldsymbol{M} / M_s$. The transfer of spin angular momentum from current to magnetization results in the excitation or movement of domain walls. The domain wall width (Δ) is a critical parameter for both field and current-driven DW motion. The DW velocity is proportional to Δ in small magnetic fields. The current distribution is affected by the presence of domain wall in magnetic materials. Such as in a 180° DW, the reversal of magnetization can make the eddy-current form a loop, the current loop can produce a magnetic field which exert a net force on the DW in the direction of drift velocity. The first contribution is the conduction electrons being reflected with different spin-dependent coefficient, the viscous force acting on the DW is from the *s-d* exchange drag, which is proportional to the current [45]. The second contribution is the exchange drag related to the transfer of spin angular momentum to the localized magnetization. Current-induced DW experiments studies can be separated into two aspects, current-induced DW propagation and current-induced DW depinning [46]. The motion of domain walls above the critical current (J_c) at zero field is an important parameter for the comparison between experiments and theory as well as for potential technology application.

3.3.3 Relationship among spin torques, motion speed and efficiency of domain walls

Perpendicular magnetic anisotropy (PMA) thin films such as Pt / Co bilayers [47], Co / Ni multilayer structure [30], Co / Pd et al [48]. PMA thin films adjacent with strong spin orbit coupling materials for example heavy metals Pt [49], W [12] and Ta [11], alloys with large spin Hall effect (WTe_2 [50], PtMn [51] et al.), topological insulators (Bi_2Se_3 [14], $Bi_{0.9}Sb_{0.1}$ [16] et al.). The interface symmetry breaking can give rise to Dzyalonshinski-Moriya interaction (DMI), which is a kind of antisymmetric interaction [52]. Quantitatively, it is a term in the Hamiltonian which can be written as:

$$\boldsymbol{H}_{i,j} = \boldsymbol{D}_{ij} \cdot \left(\boldsymbol{S}_i \times \boldsymbol{S}_j\right) \quad (2)$$

where, $\boldsymbol{S}_i$ and $\boldsymbol{S}_j$ are two neighboring magnetic spins, $\boldsymbol{D}_{ij}$ is the DMI constant. The interaction is a found of production of skyrmions, antiskyrmions, Bloch and Néel type domain walls [53, 54]. Spin Hall torques, DMI and crystalline anisotropy (K_u) all contribute to the motion speed and efficiency of domain walls. The current pulses injected into the pads of patterned nanowires shown in Figure 3.3a. Then domain wall is nucleated, which can be observed under the standard differential model of wide Kerr microscopy. The spin-orbit torques from the nonmagnetic under layers and spin transfer toques can both drive the motion of domain walls. The torques that need to drive the domain wall motion need to overcome K_u and pinning field. Therefore, the domain walls can start moving above the critical current density (J_c), which is driven by torques. The motion speed of domain wall in single PMA thin films is limited below 300 m s^{-1} with large driving current density of 2×10^8 A cm^{-2} and J_c of 5×10^7 A cm^{-2} [30]. The highlight question is how to minimize J_c, and improve speed with low driving current density in order to improve the performance of racetrack memories for practical application.

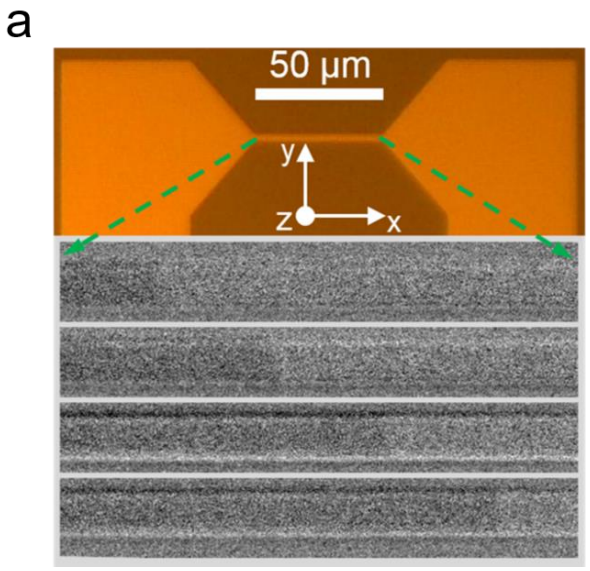

Figure 3.3a Optical micrograph of the racetrack device and Kerr microscopy differential images showing the propagation of a single domain wall along the track, in response to a sequence of 5-ns-long current pulses ($J \sim 1.2 \times 10^8$ A cm^{-2}).

3.3.4 Synthetic antiferromagnets used as racetrack memories

The synthetic antiferromagnet is consisted of two or more ferromagnetic layers separated by metallic spacers like ruthenium et al. By tuning the thickness of space layers, the magnetization state of multilayers is adjust from ferromagnetic to preferential moment parallel – to antiferromagnetic – to preferential antiparallel alignment [7]. The bottom and upper magnetic layer separated by space layer is exchange coupled. The interlayer exchange coupling

suppressed as the thickness of space layers increasing. This interlayer exchange coupling by metallic spacers or insulators is a Ruderman-Kittel-Kasuya-Yosida (RKKY) interaction, which is rooted in spin dependent Friedel-like spatial oscillations shown in Figure 3.4 a , b and c [55,56,57,58]. The typical magnetization hysteresis loop of synthetic antiferromagnets with perpendicular magnetized ferromagnetic layer is shown in Figure 3.5 a and b, with applied field normal to and parallel the sample. The ratio between remanent (M_r) and saturation (M_s) magnetization indicates the strength of exchange coupling torque in SAF structure according to one-dimensional model of domain wall dynamics [28]. The exchange coupling toque is critical for domain wall motion to obtain high speed in SAF structure.

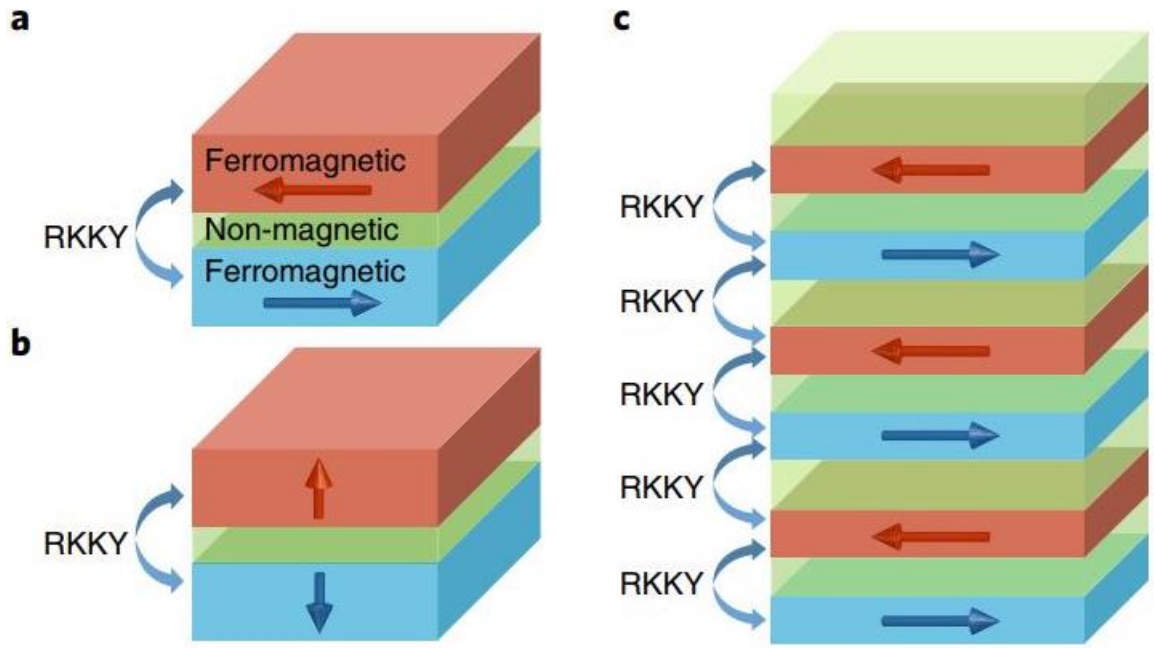

Figure 3.4 (a) Bilayer with in-plane magnetization. (b) Bilayers with out-of-plane magnetizations. (c), Multilayer. The arrows within each ferromagnetic layer indicate the direction of magnetization. Depending on the magnetic configurations the RKKY coupling and dipolar fields add (a) or substract (b), leading in part to the large degree of tenability of multilayers. This figure is from Ref [7].

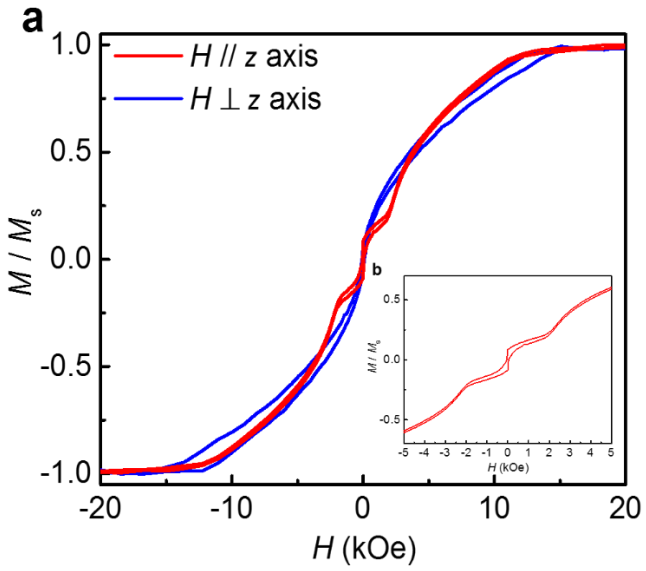

Figure 3.5 (a) Out-of-plane (red) and in-plane (blue) magnetic hysteresis loops for synthetic antiferromagnet with perpendicular magnetized ferromagnetic layer. (b) The magnified out-of-plane *M* - *H* loop shown in the inset.

Furthermore, it is found that spin-orbit torques can contribute to highly efficient domain wall movement. And, interfacial DMI can stabilize Néel domain wall. The interlayer exchange coupling torque can stabilize Néel structure of domain wall and enhance its driving motion speed in multilayer of Co / Ni structure by using Ru as space layer with Pt as spin-orbit torque sources. According to previously report, the crystal structure of SAF is highly textured with [111] orientation. J_c is as large as ~ 50 MA/cm^2 to excite the motion of domain wall even with much high speed (> 750 m s^{-1}). Based on our findings about giant spin Hall effect in M_xAl_{100-x} alloy thin films and their high degree of crystallinity. We tried to use M_xAl_{100-x} alloys as new spin-orbit torque sources to replace platinum to achieve the goal of energy efficient racetrack memories.

3.4 Perpendicular magnetic anisotropy of Co / Ni / Co multilayer with [001] orientation

Conventionally, perpendicular magnetic anisotropy of Co / Ni multilayer is used as ferromagnetic units in racetrack memories. Based on our findings about giant spin Hall effect in various kinds of Ta_xAl_{100-x}, W_xAl_{100-x}, Re_xAl_{100-x}, Os_xAl_{100-x}, Ir_xAl_{100-x}, Pt_xAl_{100-x} and Au_xAl_{100-x} alloys. We grew multilayer of 3Co / 7Ni / 2.5Co (all the numbers are Å) on top of 43Å M_xAl_{100-x} thin film, the magnetization hysteresis loop of Co / Ni / Co multilayer is shown in Figure 3.6 a - g.

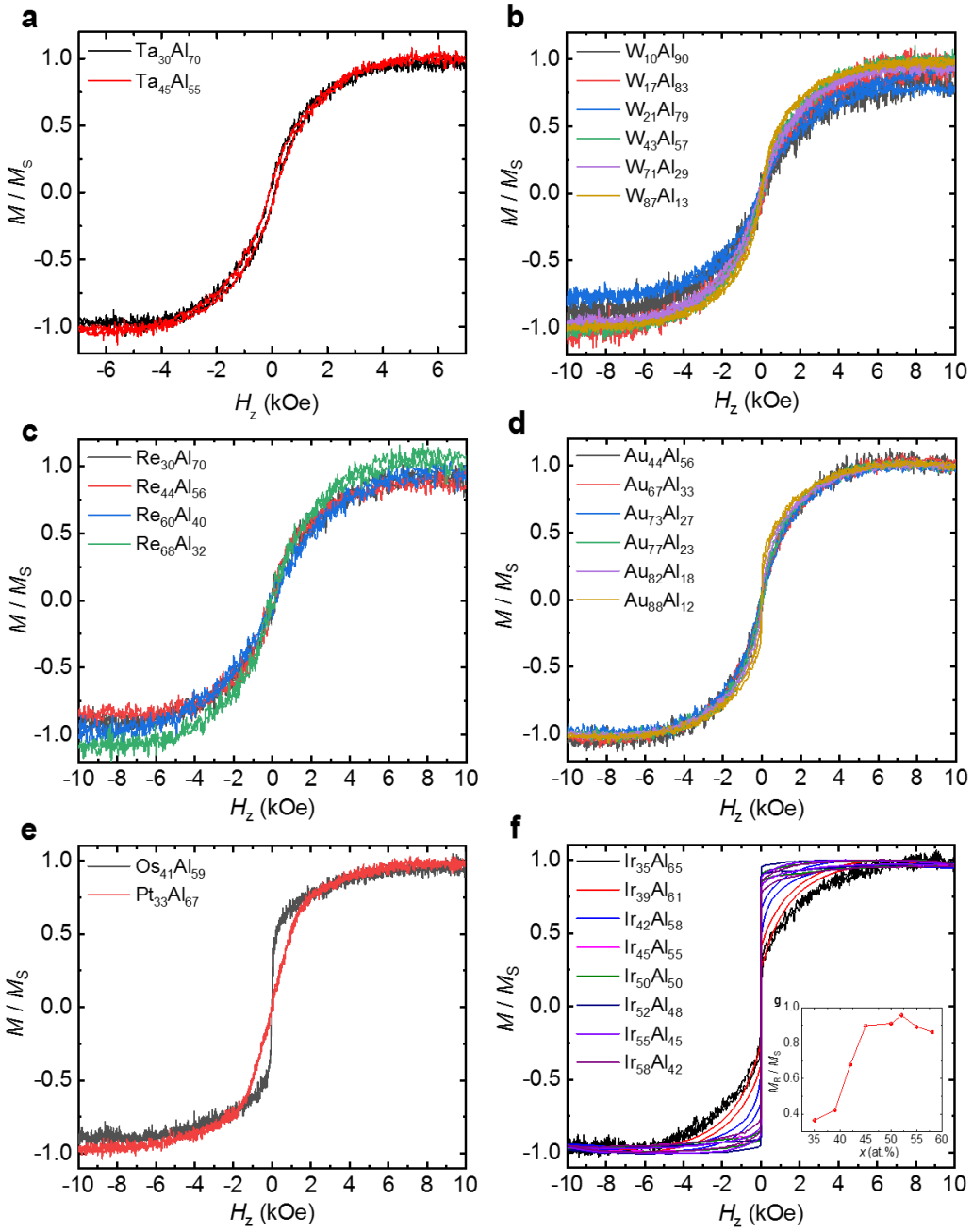

Figure 3.6 (a – g) All the thickness of M_xAl_{100-x} layers is 43 Å with multilayer structure of 3 Co | 7 Ni | 2.5 Co grown on top, all the samples are grown on top of MgO (001) substrates, and all samples capping with 50 Å TaN as protective layer. Field is perpendicular to the samples.

It is found that Co / Ni / Co multilayer grown on top of Ir_xAl_{100-x} and Pt_xAl_{100-x} thin films showing PMA, which may be correlated with $L1_0$ crystal structure of Ir_xAl_{100-x} and Pt_xAl_{100-x}. Furthermore, the magnetic state varies from weak to strong PMA as x increasing for Co / Ni / Co multilayer formed on top of Ir_xAl_{100-x} layer, which could be correlated with its lattice parameter. We patterned these blanket films with racetrack memories design. However, the domain wall can be nucleated by current pulses but thermally unstable because of low magnetic crystalline anisotropy. We further increase the bottom and top layer thickness of Co into 5Co /

7Ni / 3Co with Ir_xAl_{100-x} under layer (x = 35, 42, 50, 55 and 58), and its out-of-plane and in-plane magnetization hysteresis loop is shown in Figure 3.7 a – f.

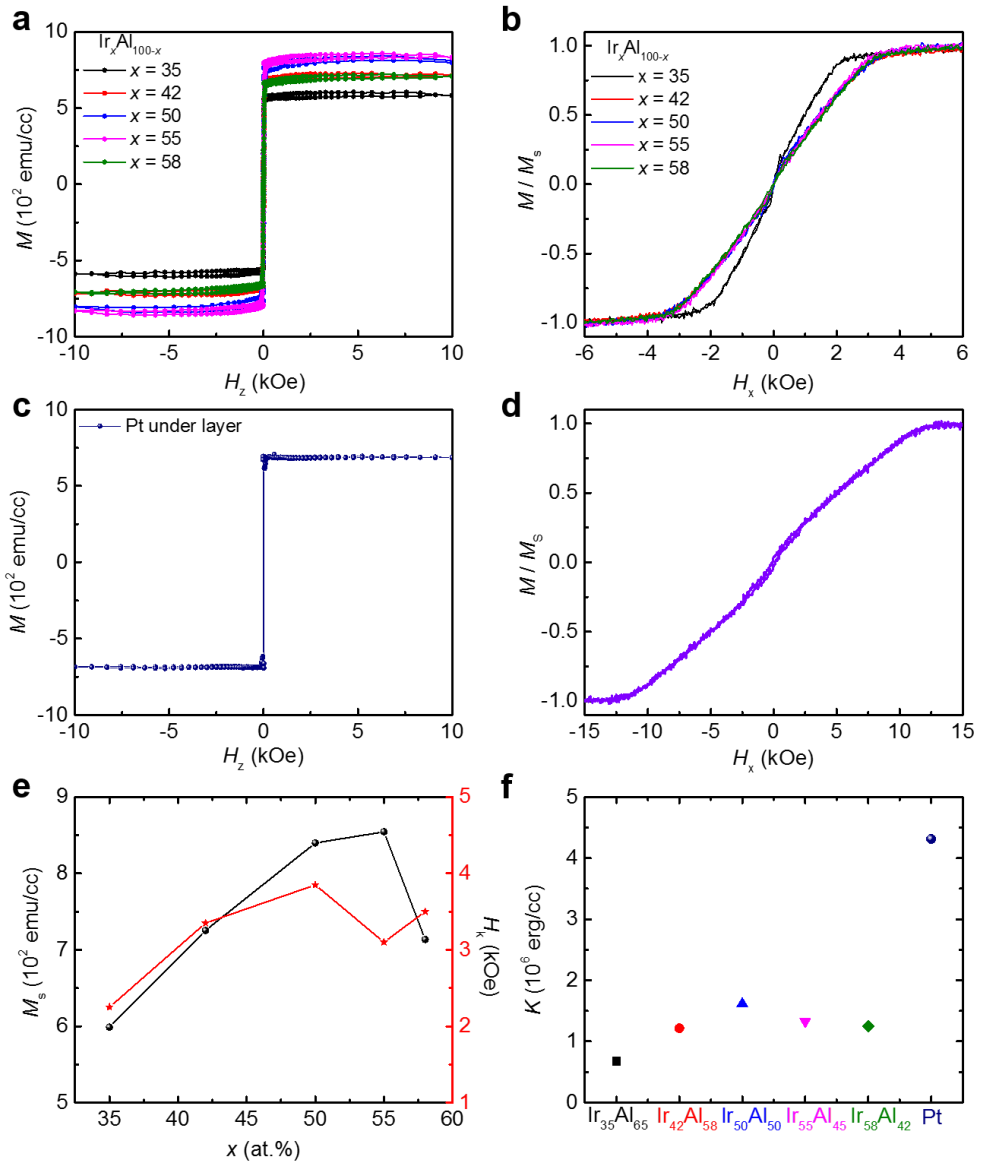

Figure 3.7 (a) Out-of-Plane and (b) in-plane magnetization hysteresis loop of Co / Ni / Co with Ir_xAl_{100-x} under layer. (c) Out-of-plane and (d) in-plane magnetization hysteresis loop of Co / Ni / Co with Pt under layer. (e) Plot of saturation magnetization and anisotropy field of Co / Ni / Co versus x for Ir_xAl_{100-x} under layer. (f) Magnetic crystalline anisotropy K_u of Co / Ni / Co with different under layers.

Comparing with the same film stack of Co / Ni /Co grown on top of 43Å Pt under layer, Co / Ni / Co multilayer grown on top of Ir_xAl_{100-x} alloys shows strong perpendicular magnetic anisotropy with small anisotropy field (H_k) shown in Figure 3.7 d, e and f. H_k is smaller with an order of three comparing with that in Co / Ni / Co grown on top of Pt under layer. The saturation magnetization (M_s) of Co / Ni / Co grown on top of Ir_xAl_{100-x} increases from 600 to

850 emu/cc with x varying from 35 to 55 atom % then reduced to 710 emu/cc. The increase of M_s as a function of x is most probably from proximity induced moment at the interface between Ir_xAl_{100-x} and Co layers. H_k changes slightly with x increasing. The magnetic crystalline anisotropy energy $K_{u,eff}$ is defined by:

$$K_{u,eff} = \frac{H_k M_s}{2} \quad (3)$$

$K_{u,eff}$ reaches a peak value of 1.62×10^6 erg/cc for $Ir_{50}Al_{50}$ then gradually decreases with x increasing. $K_{u,eff}$ is three times larger for Co / Ni / Co multilayer grown on top of Pt under layer compare with that on top of Ir_xAl_{100-x} alloy. This result is related to crystal orientation, crystal structure and lattice parameter of Co / Ni /Co multilayer. Conventionally, the crystal growth direction of Co / Ni / Co is (111) orientation on top of platinum. We further check the cross-section TEM image of IrAl / Co / Ni / Co full stack in Figure 3.8a. The full layer stack shows [001] orientation following the growth direction of Ir_xAl_{100-x} under layer, which is 45° along the MgO substrate edge. We can see that the lattice constant of Co and Ni follows the epitaxy growth relationship with Ir_xAl_{100-x} under layer. And Co and Ni crystallized in cubic structure.

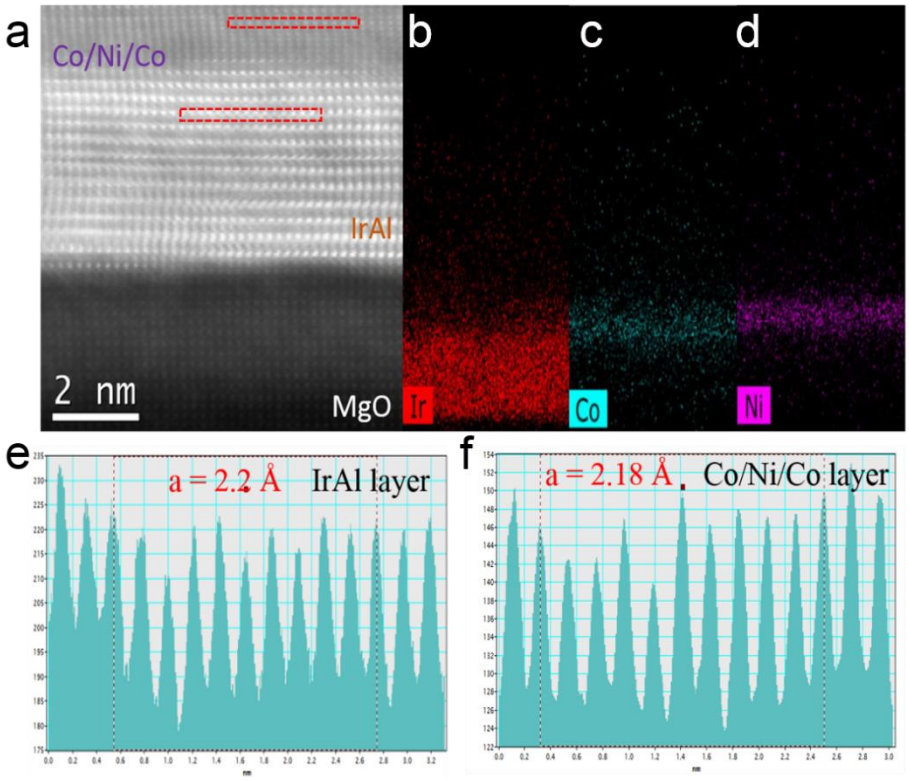

Figure 3.8 (a) Cross section HAADF-STEM images, (b)-(d) Energy dispersive X-ray element mapping and in-plane line scan for a 43 $Ir_{50}Al_{50}$ | 3 Co | 7 Ni | 2.5 Co sample with [100] viewing direction along MgO substrate.

3.5 Domain wall motion of Co / Ni / Co multilayer with [001] orientation

Domain wall can be moved with a threshold current density of $J_c \sim 8 \times 10^7$ A cm^{-2} by using 43 Å platinum as spin Hall effect layer. The motion speed of domain wall saturates at 250 m s^{-1} with a current density of 2.5×10^8 A cm^{-2} in Figure 3.9a. Furthermore, we use 43 Å Ir_xAl_{100-x} thin film as spin-orbit torque sources. It is shown in Figure 3.9b, J_c varies as the composition of Ir_xAl_{100-x} alloy, which is three times smaller compare with that in Pt based racetrack memories. The saturation speed gradually increases with x varying from 35 to 58 atom % at same current density. And J_c changes dramatically from 7 to 2.7×10^7 A cm^{-2} with $v > 10$ m/s. The mobility of domain wall (ξ_{DW}) is defined as the slope of domain wall motion velocity v versus current density near J_c in Figure 3.9e. ξ_{DW} increases from 0.95 to 3.87×10^{-10} m^3 s^{-1} A^{-1} with x varying from 35 to 58 atom %.

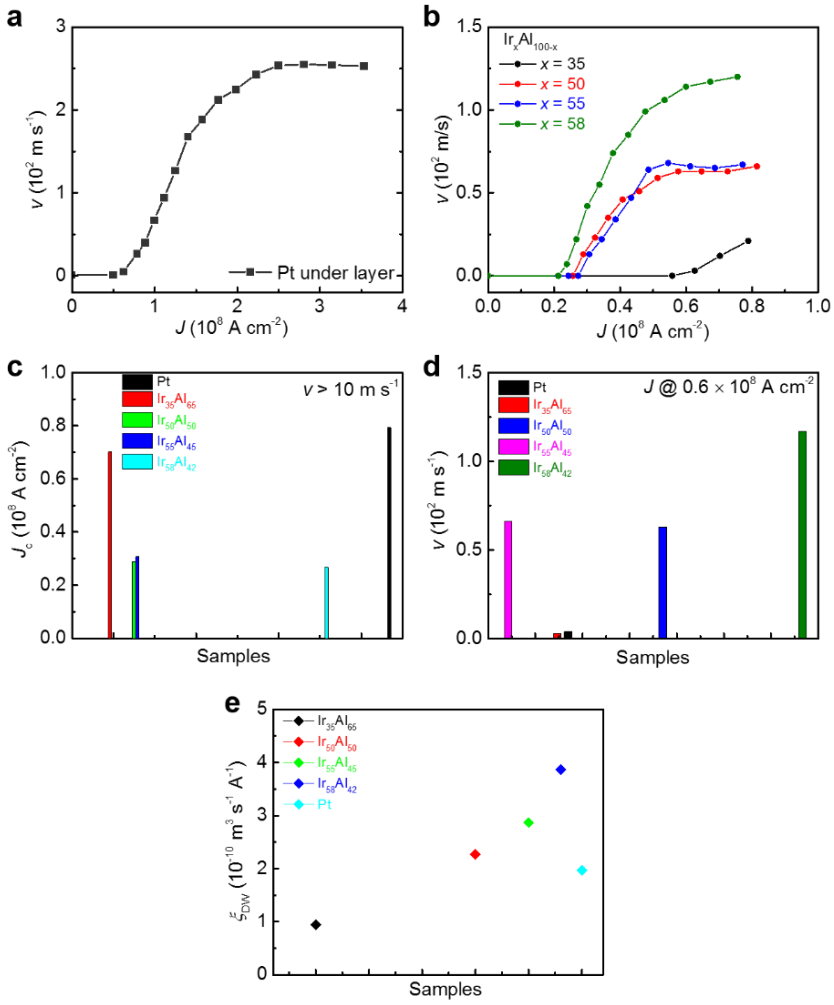

Figure 3.9 DW velocity ***v*** versus pulse current density ***J*** in nanowires formed from 43 Å Pt (a) and 43 Å Ir_xAl_{100-x} / Co / Ni / Co (b) under layer. (c) J_c at $v > 10$ m/s for different under layers (d) v for different under layers with J @ 6×10^7 A cm^{-2}. (e) Domain wall mobility for different under layers.

3.6 [001] orientation synthetic antiferromagnets with $L1_0$ RuAl alloy as space layer

In our work, based on highly efficient domain wall motion in Ir_xAl_{100-x} / Co / Ni / Co multilayer with [001] crystal orientation. We built synthetic antiferromagnet with [001] crystal orientation. We discovered a new kind of $L1_0$ RuAl space layer by magnetron co-sputtering growth. This $L1_0$ RuAl alloy thin film is used as space layer provide exchange coupling between upper and lower magnetic Co / Ni / Co stack, which is different from conventional SAF by using Ru. High-resolution cross section TEM images and XRD result of 10 nm RuAl thin film is shown in Figure 3.10 a - e. XRD result suggests that RuAl is layered compound, which has the same crystal structure as IrAl. The refraction fringe from XRD curve indicates the high degree of crystallinity of RuAl thin film grown on top of (001) orientation MgO substrate.

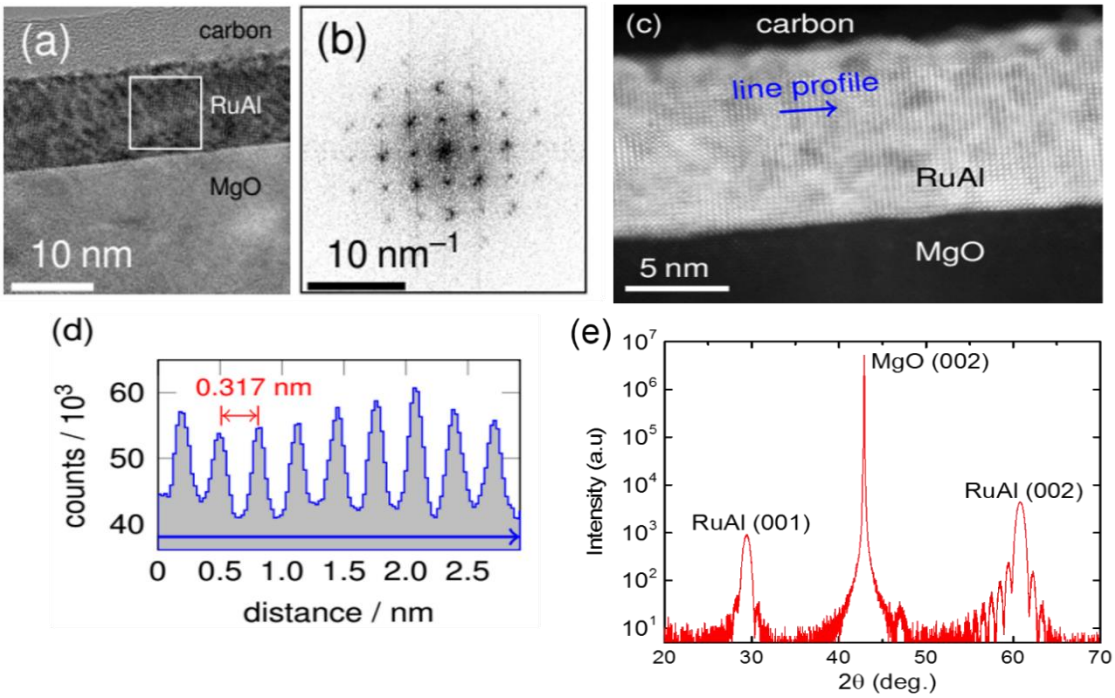

Figure 3.10 (a) Cross section HAADF-STEM images with [100] viewing direction. (b) Fourier transform of the indicated region in each respective TEM image. (c) STEM images for RuAl film taken using a high-angle annular dark-field detector. (d) Intensity line scan measured along the indicated line in each respective STEM image, with the average peak spacing shown. (e) X-ray diffraction of RuAl thin film.

The bottom magnetic layer stack is 3Co / 7Ni / 2.5Co and upper layer is 3Co / 7Ni / 3Co in order to lowering the ratio between M_r and M_s for enlarging the exchange coupling torque. We varied the layer thickness of RuAl, the out-of-plane magnetization hysteresis loop is shown in Figure 3.511a. We minimize the ratio between M_r and M_s with 8 Å RuAl layer.

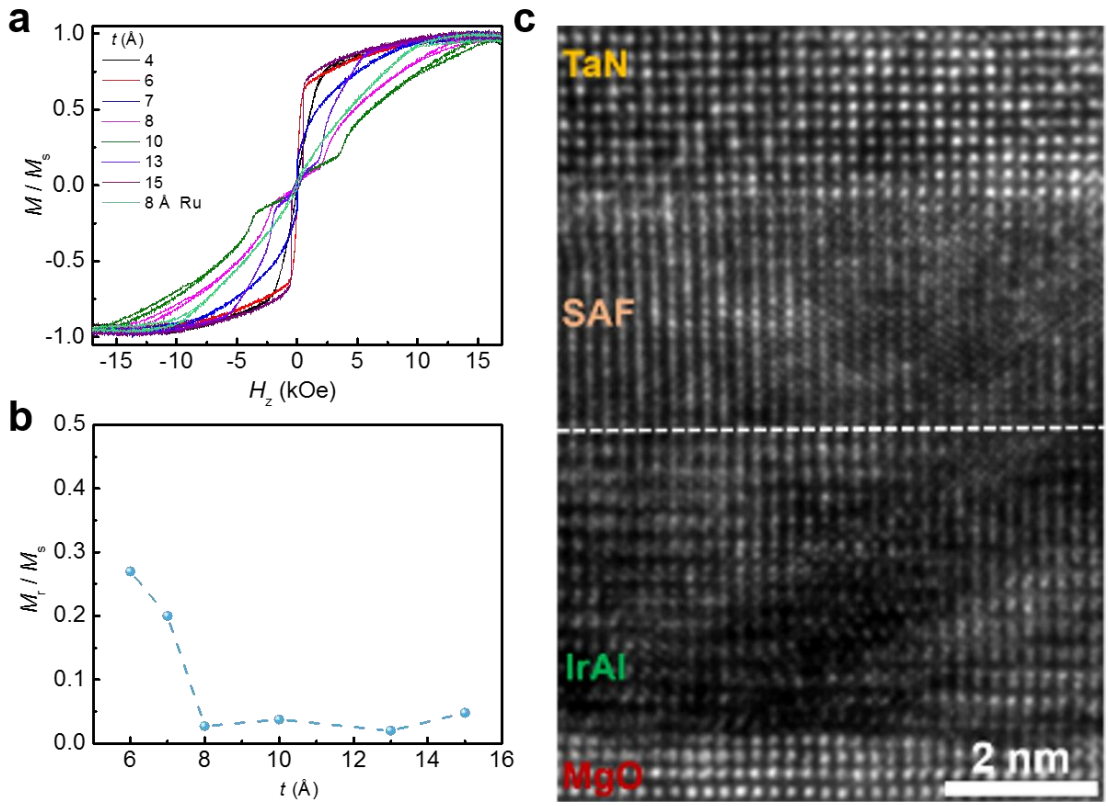

Figure 3.11 (a) Out-of-plane magnetization hysteresis loops for 43 $Ir_{42}Al_{58}$ / 3Co / 7Ni / 2.5Co / *t* RuAl (8 Ru) / 3Co / 7Ni / 3Co samples with different thickness of RuAl. (b) Plot between M_r / M_s versus RuAl layer thickness. (c) HAADF-STEM images for a 43 $Ir_{50}Al_{50}$ | SAFs.

In the meantime, there is no synthetic antiferromagnetic coupling by using 8 Å Ru layer in Ir_xAl_{100-x} / Co / Ni / Co multilayer comparing with $L1_0$ RuAl layer. The crystal structure of Ru is hexagonal, which may show large lattice mismatching with [001] orientation Co / Ni / Co multilayer. Therefore, 8 Å Ru space layer can't provide exchange coupling between bottom and upper Co / Ni / Co multilayer. The cross section HAADF-STEM images in Figure 3.11c shows that growth direction of whole SAF stack is along [001] orientation with cubic structure of Co , Ni and TaN.

We varied the composition of Ir_xAl_{100-x} under layer with synthetic antiferromagnetic films formed on top. Out-of-plane and in-plane magnetization hysteresis loop is shown in Figure 3.12 a and b measured by SQUID - VSM. In Figure 3.12 c and d, plot of M_s versus x for Ir_xAl_{100-x} – SAFs shows M_s is strongly dependent the composition of Ir_xAl_{100-x} thin film. M_s gradually increases with x increasing finally saturated, which is mostly derived from proximity induced magnetic moment from Ir_xAl_{100-x} under layer. Furthermore, the ratio between M_r and M_s is minimum and anisotropy field (H_k) displays the maximum value at x ~ 42 atom %.

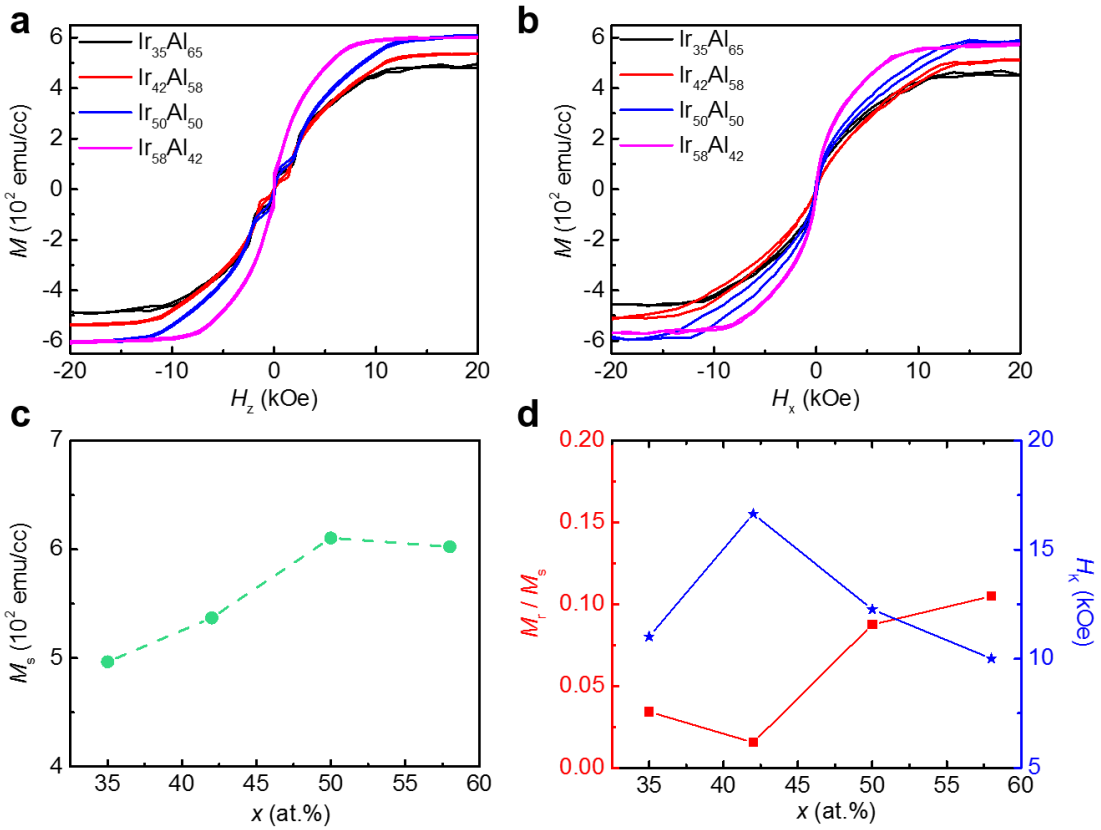

Figure 3.12 (a) Out-of-plane and (b) in-plane magnetization hysteresis loops for 43 Ir_xAl_{100-x} | SAFs as a function of x. (c) Saturated magnetization M_S of 43 Ir_xAl_{100-x} | SAFs structure as a function of x. (d) Value of M_r / M_s and anisotropy field H_K as a function of x.

3.7 Domain wall motion in synthetic antiferromagnets with [001] orientation

We fabricated the nanowires from Ir_xAl_{100-x} – SAFs blanket films as shown in Figure 3.13a. We measured the domain wall velocity of these nanowires with nanosecond current pulses under the time differential mode of Kerr microscope. We monitor the change of domain wall position in Figure 3.13b. The plot of DW velocity versus current density is shown in Figure 3.13c. The maximum velocity of domain wall motion increases from 300 to 650 m s^{-1} with x varying from 35 to 58 atom %. The minimum threshold current density J_c is ~ 7.5×10^6 A cm^{-2} for SAF with $Ir_{35}Al_{65}$ as under layer. The domain wall velocity is maximum at same current density with $Ir_{42}Al_{58}$ as spin-orbit torque sources in Figure 3.14a. The plot of domain wall velocity versus M_r / M_s ratio shows the inverse proportional relationship. The velocity is maximized with lowering M_r / M_s ratio. Furthermore, lowering M_r / M_s ratio can improve the domain wall mobility shown in Figure 3.14b. We found that the maximum domain wall velocity of Ir_xAl_{100-x} – SAF structure is strongly dependent on anisotropy field of SAF structure shown in Figure 3.14d. The plot of DW velocity versus in-plane field in Figure 3.14e shows a completely

different behavior in which the DW velocity is decreased for both positive and negative H_x and the behavior no longer depends on the ↓↑ or ↑↓ DW configuration. The dependence of J_{th} and σ_{SH} on Ir content in Ir_xAl_{100-x} shows that J_{th} decreases with increasing σ_{SH} consistent with an increasing spin-orbit torque (Figure 3.14f).

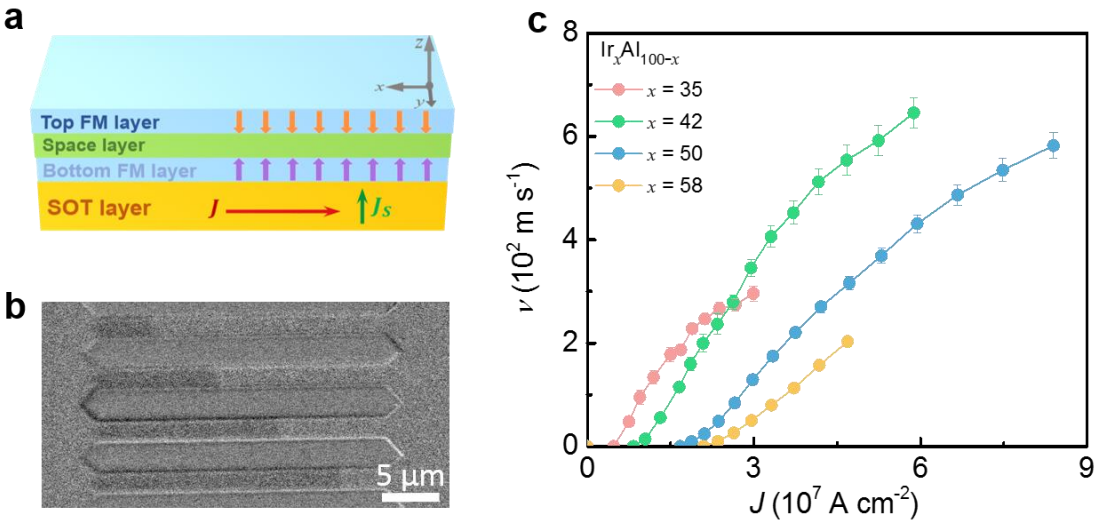

Figure 3.13 (a) Schematic of SAF multilayer with an Ir_xAl_{100-x} underlayer. (b) Kerr microscopy differential images showing the propagation of a single domain wall along the track, in response to a sequence of 5-ns-long current pulses ($J \sim 1.2 \times 10^8$ A cm^{-2}). (c) DW velocity $\boldsymbol{v}$ versus pulse current density $\boldsymbol{J}$ in nanowires formed from 43 Å Ir_xAl_{100-x} | SAFs.

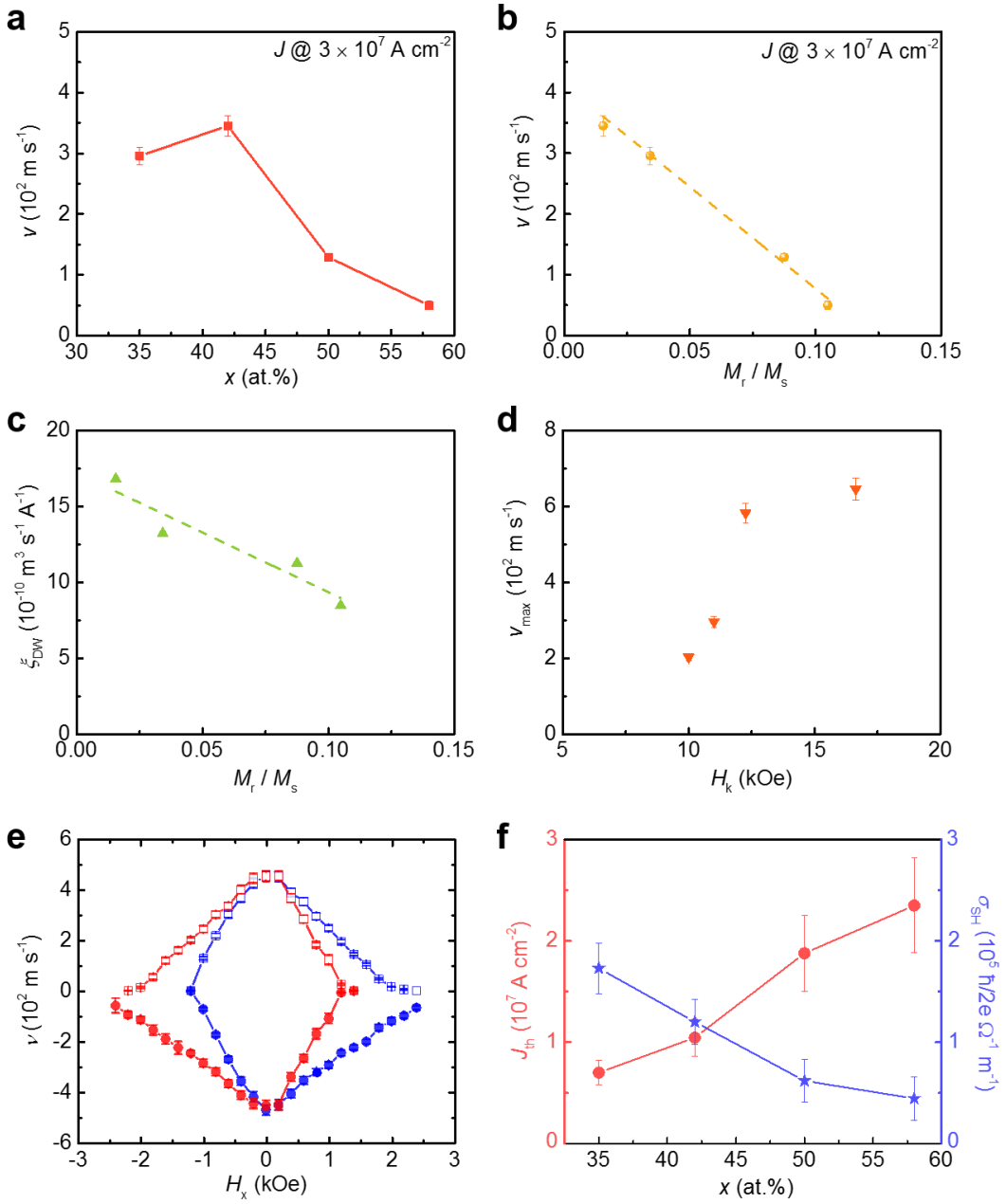

Figure 3.14 (a) Plot of DW velocity versus x for Ir_xAl_{100-x} – SAF at the current density of 3×10^7 A cm^{-2}. (b) Plot of DW velocity versus M_r / M_s *ratio* for Ir_xAl_{100-x} – SAF at the current density of 3×10^7 A cm^{-2}. (c) Plot of DW mobility versus M_r / M_s *ratio* for Ir_xAl_{100-x} – SAF at the current density of 3×10^7 A cm^{-2}. (d) Plot of maximum DW velocity versus anisotropy field for Ir_xAl_{100-x} – SAF at the current density of 3×10^7 A cm^{-2}. (e) Domain wall velocity ν as a function of both positive and negative in-plane (H_x) magnetic field in nanowires formed from 43 $Ir_{42}Al_{58}$ | SAFs. (f) Critical threshold current density (J_{th}) to drive the domain walls in Ir_xAl_{100-x} | SAF structures, and spin Hall conductivity of Ir_xAl_{100-x} as a function of x.

The SOT is known to be very sensitive to the detailed structure of the interface between the SOT layer and the magnetic layer. For example, as shown in Figure 3.15a, 2 Å thick Ir or Al

layers inserted at this interface significantly changes the dependence of v on the current density. The insertion of the Al dusting layer results in a lower terminal value of $v \sim 200$ m s^{-1} while J_c does not change. On the other hand, the insertion of the Ir dusting layer shifts the $v - J$ curve to higher J thus increasing J_c. These observations can be accounted for by: (i) a decrease in the DMI by the insertion of an Al dusting layer as compared with the insertion of an Ir dusting layer ; (ii) a decrease in the exchange coupling torque due to the increased ratio of M_r / M_s for the Al insertion layers as compared with the Ir insertion layers, as shown in Figure 3.15 d; (iii) an increase in spin memory loss ($\delta = t / l_{sf}$, t is the thickness of the dusting layer and l_{sf} is the spin diffusion length) arising from the strong spin-orbit interaction of Ir that degrades the strength of the spin-orbit torque as compared with the weaker spin-orbit interaction from Al which displays a very long spin diffusion length [59,60,61]. The degradation of the spin-orbit torque leads to an increase of J_c for the Ir insertion layers.

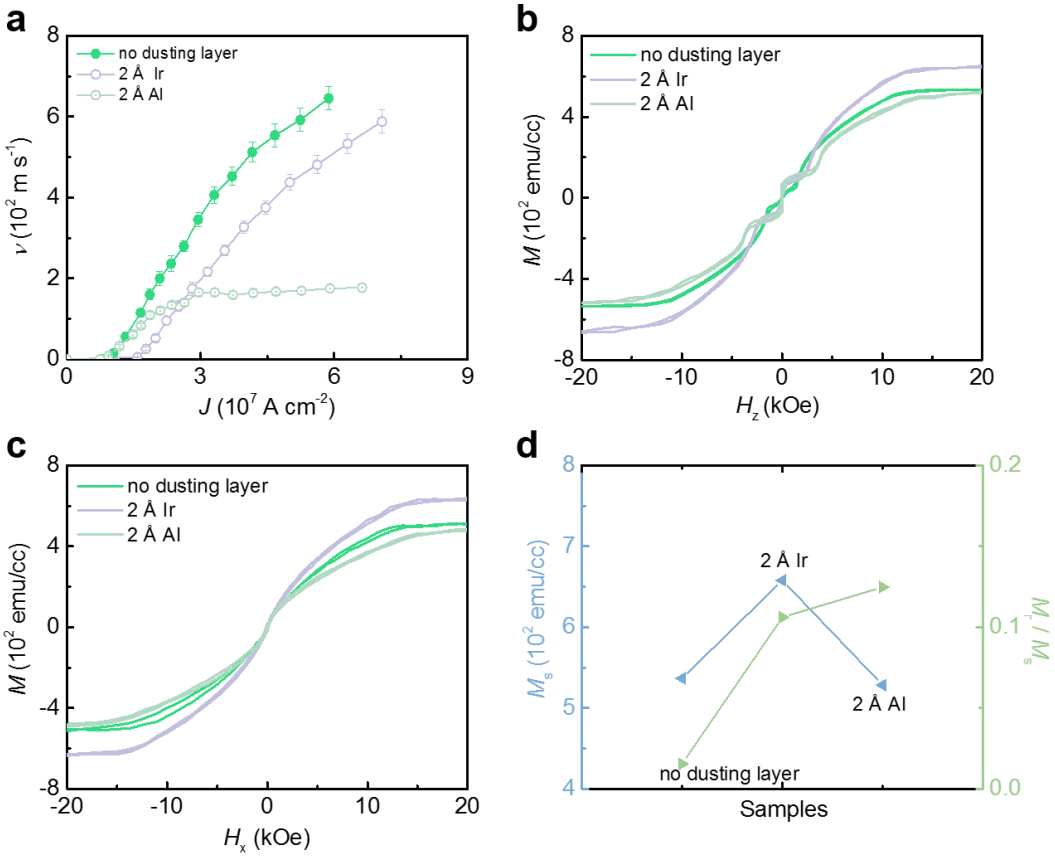

Figure 3.15 (a) DW velocity versus pulse current density in nanowires formed from 43 Å $Ir_{42}Al_{58}$ | no dusting layer and dusting layer of 2 M (M =Ir and Al) | SAFs. (b) Out-of-plane and (c) in-plane magnetization hysteresis loops measured from 43 $Ir_{42}Al_{58}$ | no dusting layer and dusting layer of 2 M (M =Ir and Al) | SAFs. (d) Both the value of M_S and M_R / M_S extracted from 43 $Ir_{42}Al_{58}$ | no dusting layer and dusting layer of 2 M (M =Ir and Al) | SAFs.

3.8 Magnetic properties and domain wall motion performance of $Co_{90}Fe_{10}$ | Ni | $Co_{90}Fe_{10}$ multilayer

Based on our findings about the connection between anisotropy field and maximum domain wall velocity, we replace Co by using $Co_{90}Fe_{10}$ in SAF structure to increase H_k. The schematic of the sample stack is shown in Figure 3.16a, the details about layer thickness is as below:

$43Ir_{42}Al_{58}$ / $3Co_{90}Fe_{10}$ / 7Ni / *t* $Co_{90}Fe_{10}$ / 8RuAl / $3Co_{90}Fe_{10}$ / 7Ni / $3Co_{90}Fe_{10}$ / 50TaN

The magnetization between bottom and upper magnetic layer is fully compensated by tuning the thickness of $Co_{90}Fe_{10}$ layer. The out-of-plane magnetization hysteresis loop is shown in Figure 3.16b with M_r / M_s ratio of 0.02. In Figure 3.16c, H_k is close to 2 T by increasing the thickness of $Co_{90}Fe_{10}$ from 2.5 to 3 Å. The comparison of performance of domain wall motion between $Co_{90}Fe_{10}$ / Ni / $Co_{90}Fe_{10}$-SAF and Co / Ni / Co- SAF is shown in Figure 3.16d. J_c shows no change for two kinds of SAF structure, because of the same $Ir_{42}Al_{58}$ under layer. And interface transparency for IrAl / Co and IrAl / $Co_{90}Fe_{10}$ may be same because of small difference of Fermi surface for Co and $Co_{90}Fe_{10}$. Fully compensated $Co_{90}Fe_{10}$ based SAF structure displays the very high domain wall motion speed with ~ 1000 m s^{-1}. The driving current density is ~ 60 MA/cm^2 which is three times smaller compare with previous studies for high motion speed of domain walls in $Co_{90}Fe_{10}$ based SAF.

3.9 Growth of M_xAl_{100-x} and M_xAl_{100-x} – SAF structure on top of Si (001) wafer

It is shown in Figure3.17a, out-of-plane magnetization hysteresis loop of Co / Ni / Co / RuAl / Co / Ni / Co multilayer shows synthetic antiferromagnetic coupling on top of $Ir_{33}Al_{67}$ under layer, however there is no SAF coupling for another two composition with $Ir_{30}Al_{70}$ and $Ir_{61}Al_{39}$. This result suggests that only in the narrow range $30 < x < 60$ for Ir_xAl_{100-x}, the Co / Ni / Co-RuAl multilayer can displays the synthetic antiferromagnetic coupling, which could be related to the lattice parameter and strain effect. Furthermore, we have seen weak SAF coupling by employing $Os_{41}Al_{59}$ and $Pt_{33}Al_{67}$ as under layer in Figure3.17b.

By using Ta and MgO as buffer layer, we have successfully grew IrAl on top with weak (001) and (002) XRD peak intensity compare with that grown on top of (001) orientation MgO substrate shown in Figure3.17c. High resolution cross section TEM images in Figure 3.17e shows that high crystallinity degree of IrAl. However, there is no synthetic antiferromagnetic coupling for Ir_xAl_{100-x} / Co / Ni / Co / RuAl / Co / Ni / Co grown on top of (001) orientation Si

wafer. This maybe because surface roughness observed from HR-TEM images and/or strain effect from multi grains.

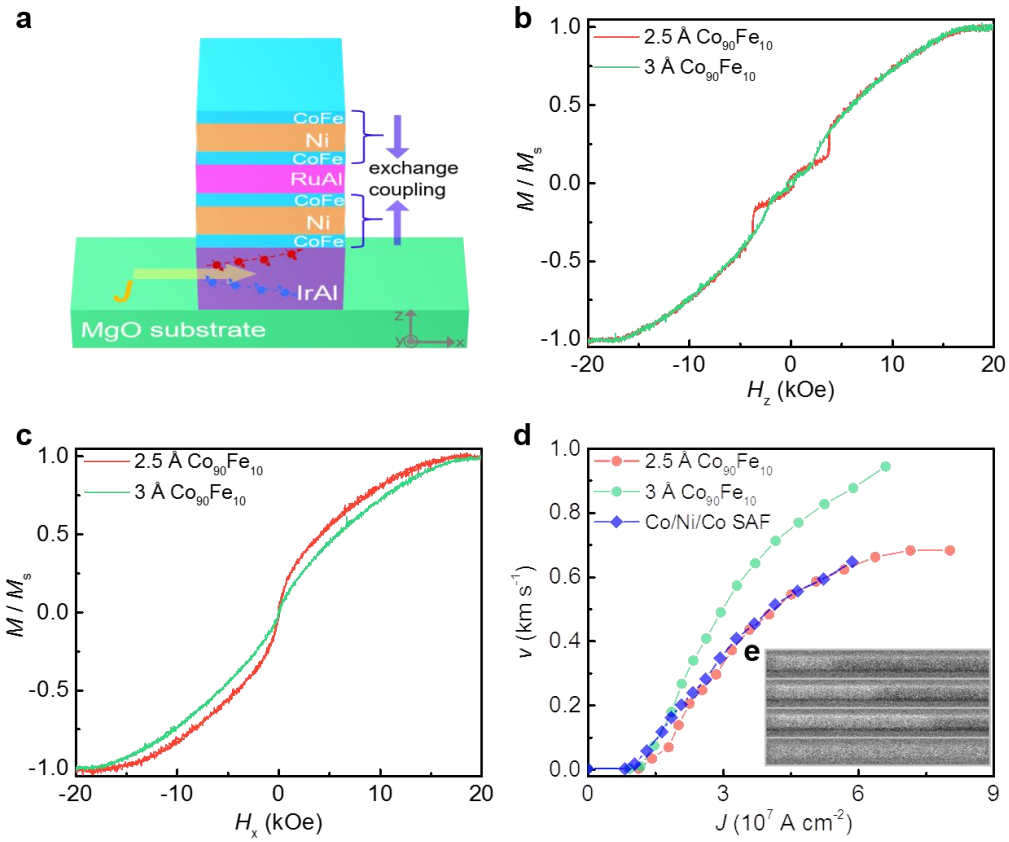

Figure 3.16 (a) Schematic of $Co_{90}Fe_{10}$ based SAF stack. (b) Out-of-plane and in-plane (c) magnetization hysteresis loop for IrAl / $Co_{90}Fe_{10}$ SAF structures. (d) Plot of DW velocity versus current pulse density for IrAl / $Co_{90}Fe_{10}$ and IrAl / Co SAF structures. (e) Kerr microscope images of a single DW moving along a nanowire formed from 43$Ir_{42}Al_{58}$ / 3$Co_{90}Fe_{10}$ / 7Ni / *t* $Co_{90}Fe_{10}$ / 8RuAl / 3$Co_{90}Fe_{10}$ / 7Ni / 3$Co_{90}Fe_{10}$ / 50TaN. Each image (up to down) is taken after applying a train of current pulses.

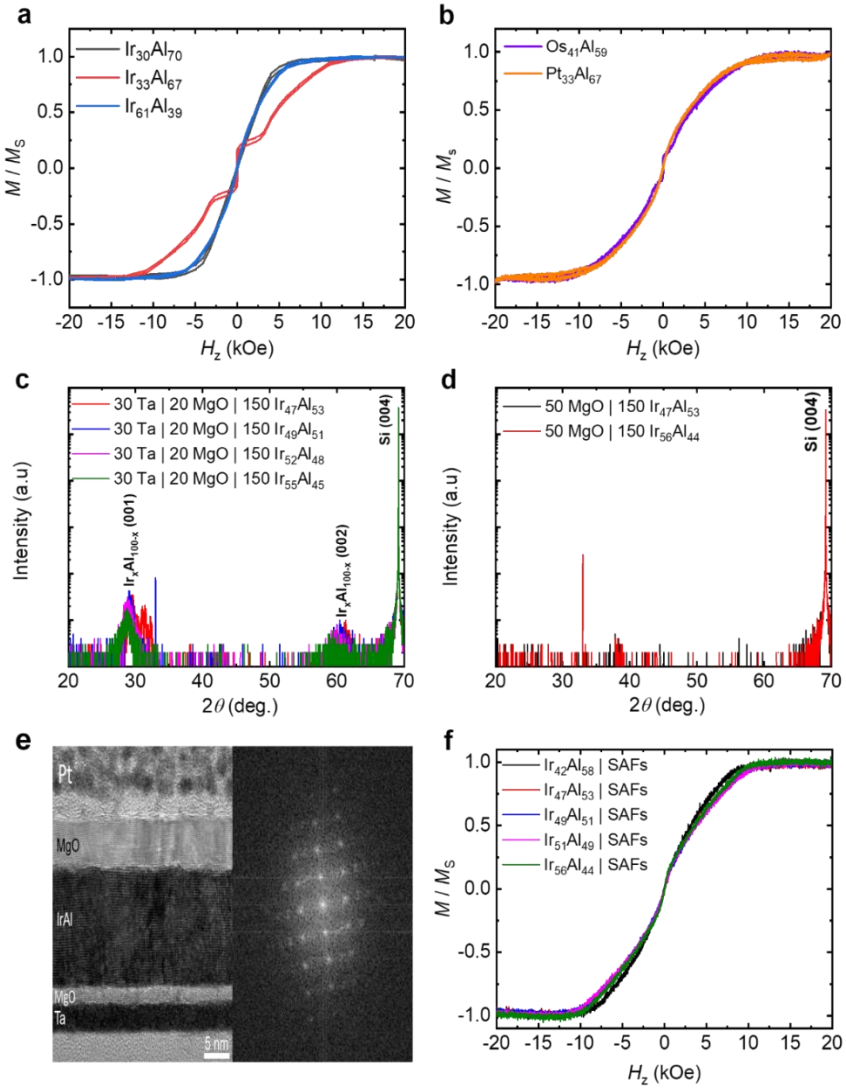

Figure 3.17 Magnetic properties of M_xAl_{100-x} | SAFs structures and crystal structure of Ir_xAl_{100-x} grown on Si (001) wafer. a) The SAFs grown on top of 43 Å Ir_xAl_{100-x} layer with different x. (b) The SAFs grown on top of 43 Å $Os_{41}Al_{59}$ and $Pt_{33}Al_{67}$ layers separately. (c) and (d) *X-ray* diffraction results of 150 Å Ir_xAl_{100-x} thin films with different x value grown on top of buffer layer with 30 Ta and 20 MgO and only 50 MgO layers separately**.** (e) High resolution cross section TEM images of full stack of IrAl grown on top of Si (001) wafer and selected area electron diffraction of IrAl layer. (f) Magnetization hysteresis loops of Ir_xAl_{100-x} | SAFs grown on top of Si (001) wafer.

3.10 Spin-orbit torque switching of IrAl - Co based SAF structures

MRAMs includes spin transfer torque MRAMs and spin-orbit torque MRAMs. We fabricate the Hall bar devices (5 × 5 µm wide) from $Ir_{42}Al_{58}$ / Co / Ni / Co - SAF stack layer structure. We input 1mA current as reading current by sweeping the field from -20 to 20 kOe with field perpendicular to the samples then measure the Hall resistance in *xy* plane. We have observed

typical R_H curve from Figure 3.18b, the orange and purple arrow indicates the pointing direction of magnetic moment in SAF film stack. The spin-flop happens by out of-plane field sweeping. By performing the SOT switching experiment in SAF films stack, first we apply an in-plane magnetic field (~ 0.5 kOe), after field stable, we injected the D.C current pulses with 10 ms pulse duration time, we use 1 mA as reading current.

Figure 3.18c shows the SAF stack is fully switched with critical current density of ~ 7 MA/cm^2, compared with R_H loop measured by field sweeping. Current density we calculate is current flowing through the $Ir_{42}Al_{58}$ layer based on a parallel resistance model, the resistivity of SAF layer stack is 65 μΩ cm. Furthermore, we test more current iteration number in the IrAl – Co / Ni / Co SAF structures to extract their thermal stability. A series of alternative positive and negative current pulses is injected separately. The SAF structure is switch by SOTs from $Ir_{42}Al_{58}$ layer without thermal distortion until 40 number of iterations. Longtime working hours and low operation current density is critical for MRAMs practical application in chip designed devices. We measured ultralong current iteration number more than 10000 times, furthermore we calculated the counts for monitoring the Hall resistance. In the process of more than ten thousand times operation, no any failure (< 1/10000) detected. Therefore, we prove that the IrAl – Co / Ni /Co - SAF stack is good materials candidate for MRAM chip structure.

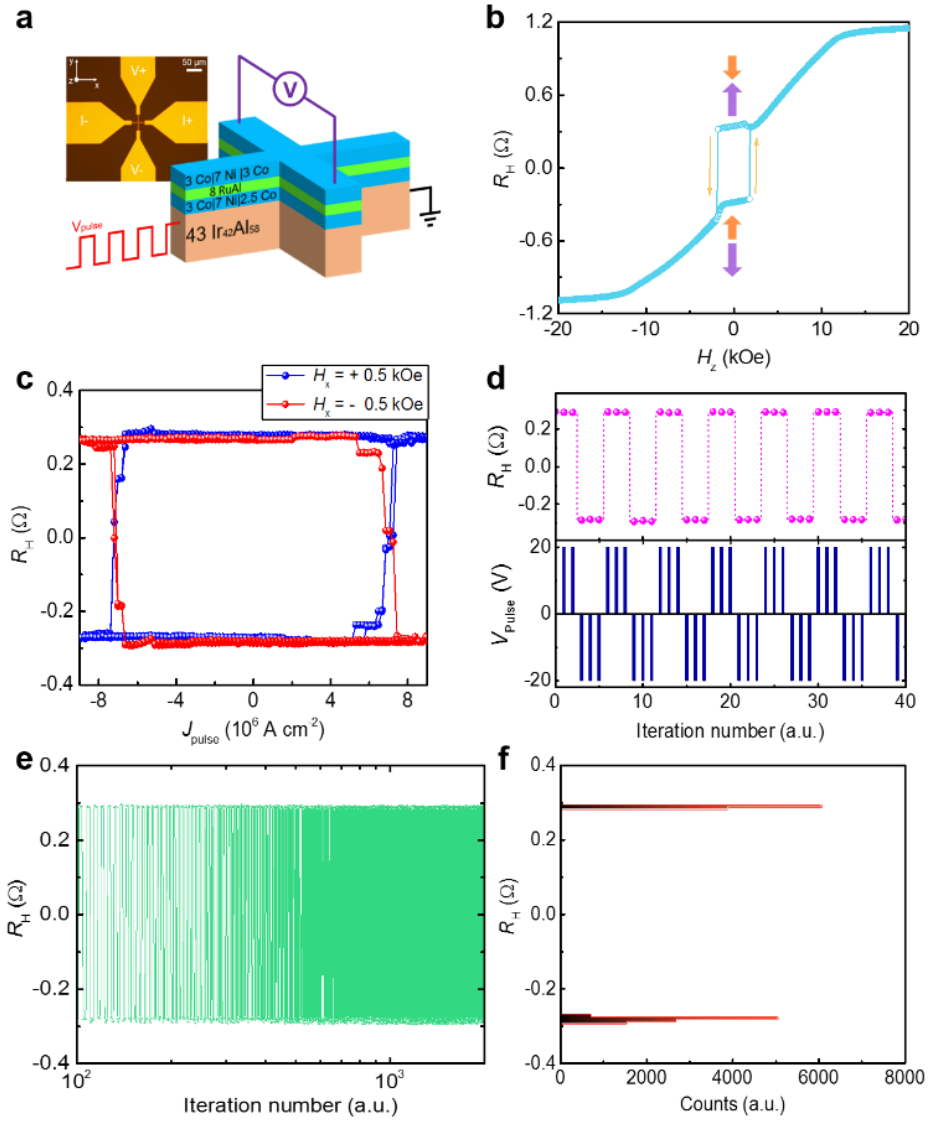

Figure 3.18 (a) Schematic diagrams of sample stack and Hall bar devices. (b) Anomalous Hall resistance (R_H) as a function of out-of-plane magnetic field H in 43 Å $Ir_{42}Al_{58}$ | SAF structures measured at 300 K. (c) Magnetization switching of 43 Å $Ir_{42}Al_{58}$ | SAF with in-plane field of ±500 Oe at 300 K. (d) Deterministic magnetization switching in 43 Å $Ir_{42}Al_{58}$ | SAF devices by a series of ~ ±20 V pulses. (e) Anomalous Hall resistance switched by a series of positive and negative voltage pulses as a function of iteration number. (f) Deterministic switching of anomalous Hall resistance.

We fabricate the pillar with 5 μm diameter on top of IrAl spin-orbit torque generator from same $Ir_{42}Al_{58}$ - SAF stack shown in Figure 3.19 a. R_H is measured by field sweeping perpendicular to the sample, the R (H) loop shows the spin-flip transition with small coercivity ~ 700 Oe. We obtain the thermal stability factor by applying the out-of-plane magnetic field pulses. We plot the switching probability as a function of field pulses. We can extract its thermal stability factor $\Delta \sim 80\ k_BT$ through the calculation of the changes of coercivity.

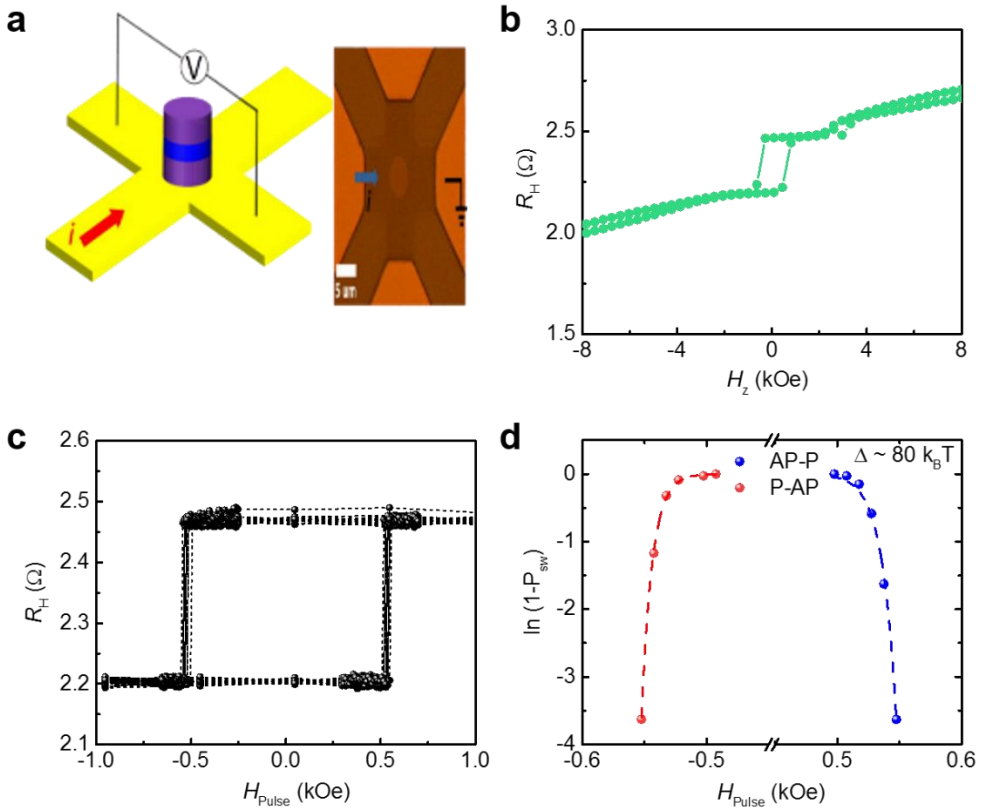

Figure 3.19 (a) Electronic transport measurement schematic of IrAl | SAFs pillar with 5 μm diameter. (b) Anomalous hall resistance measurement of 43 $Ir_{42}Al_{58}$ | SAFs pillar as a function of out-of-plane magnetic field. (c) Anomalous hall resistance measurement of 43 $Ir_{42}Al_{58}$ | SAFs pillar as a function of out-of-plane magnetic field pulse. (d) Probability of magnetization switching as a function out-of-plane magnetic field pulse.

3.11 Exploration of magnetic tunnel junction with $Ir_{42}Al_{58}$ under layer

The writing and reading parts of MRAMs include the bit-line used for current pulses injection and magnetic tunnel junction (MTJ) for data reading. The MTJ is consisted of two thin magnetic layers separated by 1 to 2 nm insulating materials such as MgO, AlN et al.. The magnetoresistance of MTJ depends on the magnetic moment separated by the insulating tunnel barrier. Tunneling resistance R of MTJ is larger when the magnetizations are antiparallel (R_{AP}) compare with parallel magnetizations (R_P). TMR effect is the change of resistance related to the magnetization orientation of magnetic layers.

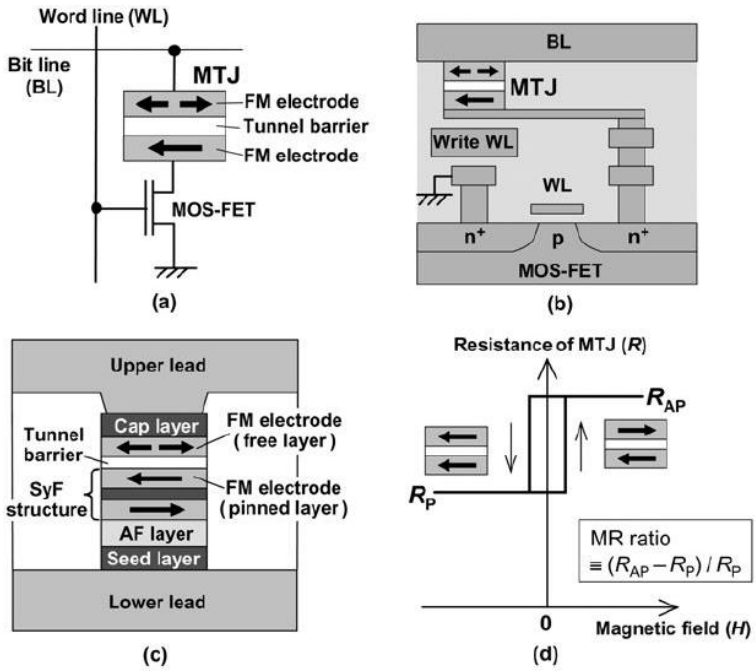

Figure 3.20 (a) - (c) Schematic of components of memory cells. (d) Plot of resistance of MTJ versus magnetic field.

Conventionally, the MRAMs includes two types: spin transfer torque MRAMs (STT-MRAMs) and spin-orbit torque MRAMs (SOT-MRAMs) [63, 64]. SOT-MRAMs display the advantage of low operational current density, fast reading and writing speed and low writing error rate compare with STT-MRAMs [64]. The cells of MRAM is shown in Figure 3.20 d. High and low resistance state is used to represent the status of "0" and "1" for MRAMs by TMR effect and write-line is used to inject nanoseconds or picoseconds current pulses. Normally in-plane magnetized MTJ stack needs large field to break magnetization state. However, we came up with new concept of out-of-plane magnetized MTJ stack with synthetic antiferromagnet as bottom layer. Based on the results about high speed domain wall motion and low critical current density driving by large SOTs from Ir_xAl_{100-x} under layer in Co / Ni / Co SAF and $Co_{90}Fe_{10}$ / Ni / $Co_{90}Fe_{10}$ SAF, we grew MgO tunnel barrier on top then we found giant TMR results.

We grow the full MTJ stack as shown in Figure 3.21a, the details of full stack is 300 $Ir_{42}Al_{58}$ / 5 Co / 7 Ni / 4 Co / 8 RuAl / 7 $Co_{90}Fe_{10}$ / 4 Mg / 20MgO / 11 $Co_{20}Fe_{60}B_{20}$ / 5 Ta / 3.4 Co/ 10.5Pt / [3.1Co / 8.5Pt]×7 / 100 Ru, (all number units are Å) which is used to check TMR results by CIPT. We grow Co / Ni / Co / RuAl / $Co_{90}Fe_{10}$ SAF as bottom layer then $Co_{20}Fe_{60}B_{20}$ as free layer, MgO as tunnel barrier. 4 Å Mg is used to protect $Co_{90}Fe_{10}$ from being oxidized by oxygen ion. We did in-situ annealing after the deposition of Ta layer to improve the crystallinity degree of MgO tunnel barrier in order to improve TMR ratio. The sample ID is related to different in-situ annealing temperature (A2478- 56 ^oC, A2479- 65 ^oC, A2480- 75 ^oC, A2481- 85 ^oC,

A2482- 93 ºC, A2483- 100 ºC). The growth of high quality MgO is by off-axis radio-frequency sputtering gun, shown in Figure 3.21 b. *X*-ray diffraction results of annealing temperature dependent full MTJ sample stack suggests high degree of crystallinity of layered IrAl compound shown in Figure 3.21 c. The average roughness of full MTJ stack measured by AFM is 2.7 Å shown in Figure 3.21 d, with scanning range of 10 × 10 μm. The out-of-plane and in-plane magnetization hysteresis loop in Figure 3.21e and f shows typical spin-flop transition behavior of MTJ structure. Spin-flop transition field and effective anisotropy field show strong dependence on the in-situ annealing temperature of MTJ stack.

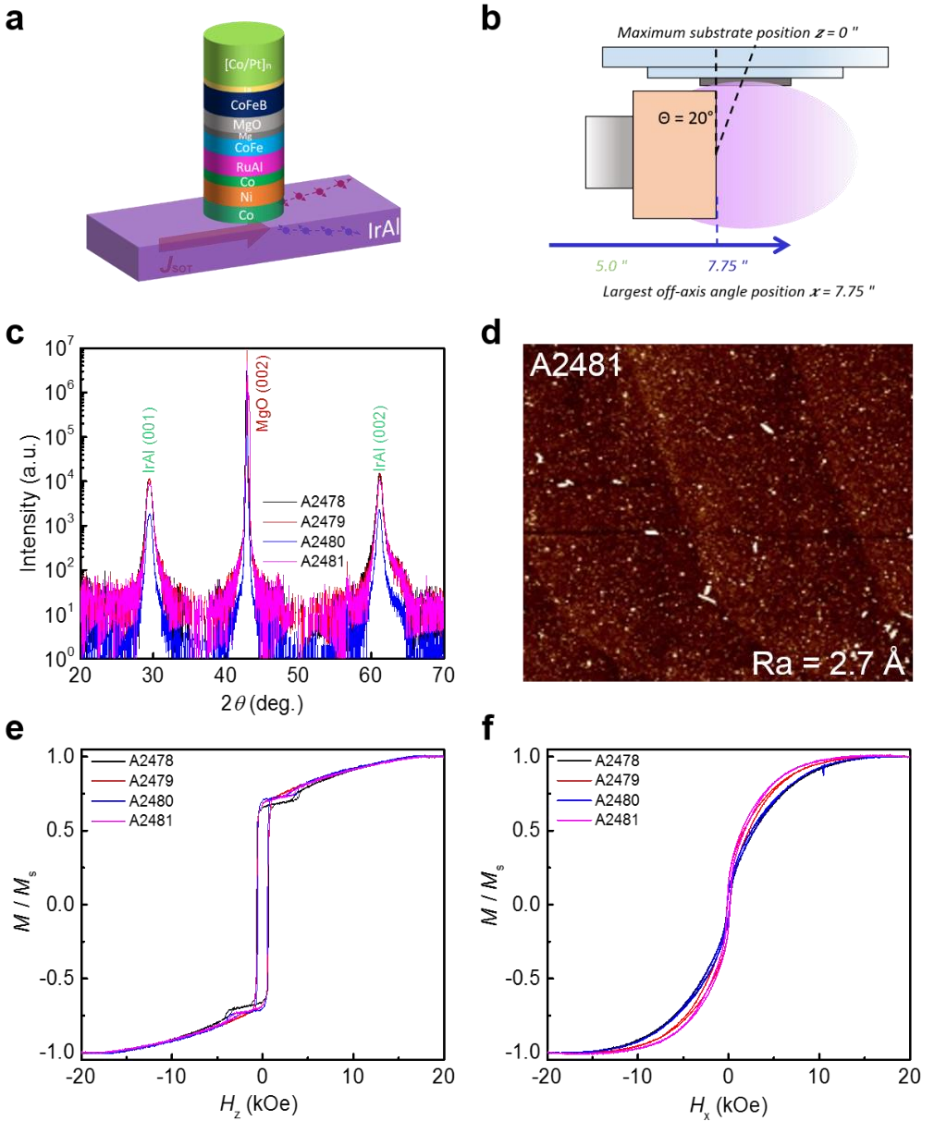

Figure 3.21 (a) Structure schematics of IrAl based full magnetic tunnel junction. (b) The schematic of off-axis rf - MgO gun configuration. (c) X-ray diffraction results of IrAl based full MTJ with different in-situ annealing temperature. (d) AFM image of IrAl – MTJ blanket film. Out-of-plane (e) and in-plane (f) magnetization hysteresis loop of IrAl – MTJ blanket films with different in-situ annealing temperature

The sheet resistance of full IrAl-MTJ stack is measured by CIPT with field perpendicular to the samples shown in Figure 3.22. The results of TMR gradually increases with in-situ annealing temperature increasing. When the in-situ annealing temperature exceeds the critical point, the out-of-plane $M-H$ loop shows some in-plane characteristics with TMR dramatically decreases from 83.5 to 7 % in Figure 3.23. This is most probably because the lattice structure of magnetic layer distorted. Then based on sample A2481, we shrink the thickness of IrAl layer from 300 Å to 43 Å. We fabricate MTJ pillar on top of IrAl under layer by e-beam lithography shown in Figure 3.24. The patterned design, optical and scanning electron micrpscopy images of magnetic tunnel junction devices is displayed in Figure 3.24. The MTJ device mapping and successful rate of fabricated devices is shown in Figure 3.25. The MTJ device yield rate for high TMR is 50 ~ 75 % which is strongly dependent on the size of MTJ pillar. The maximum TMR varies in the range of 70 ~ 86 % shown in Figure 3.25. And resistances of MTJ gradually increases with MTJ size decreasing.

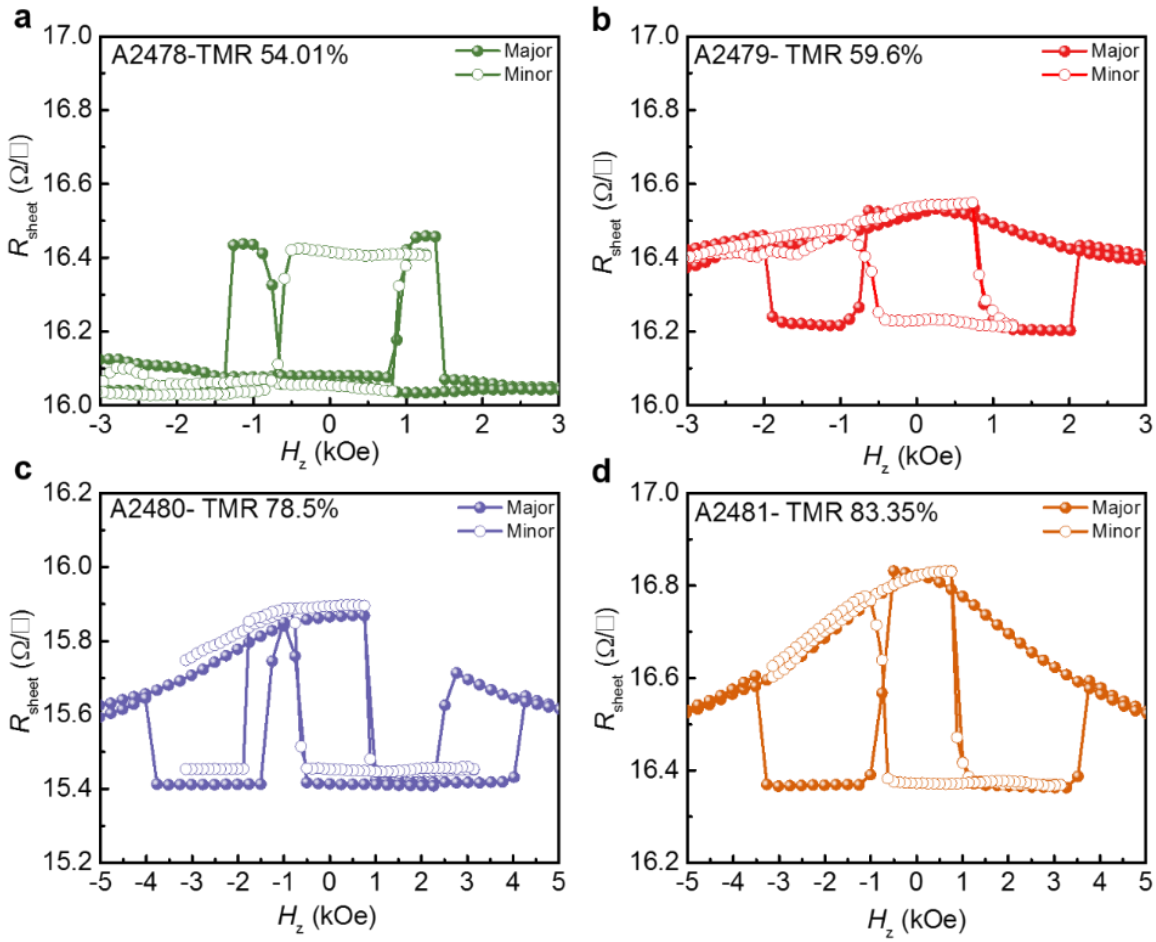

Figure 3.22 Plot of resistance versus out-of-plane magnetic field with TMR results measured by CIPT from IrAl-MTJ blanket film with different in-situ annealing temperature.

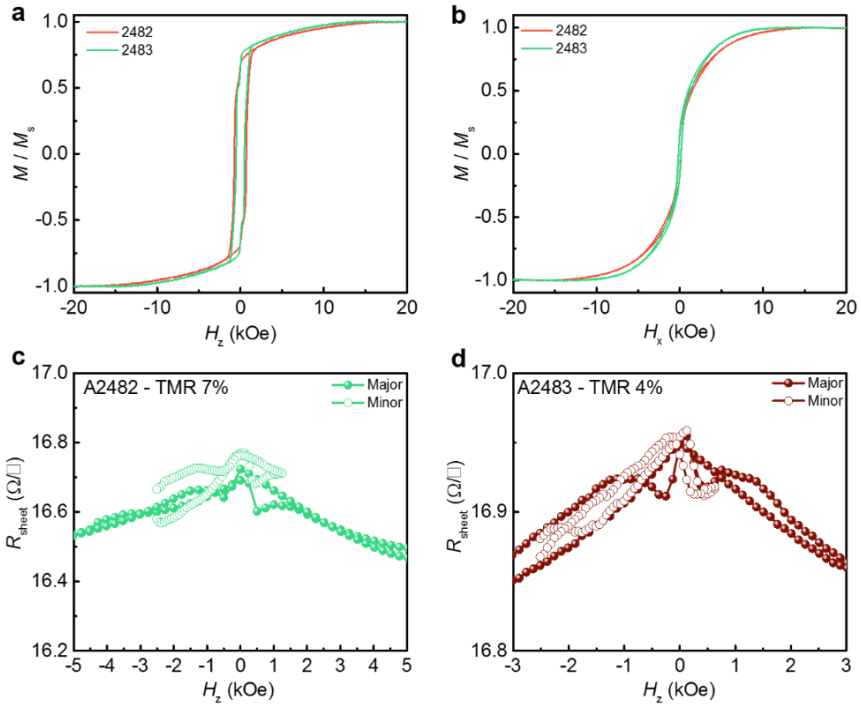

Figure 3.23 Out-of-plane (a) and in-plane (b) magnetization hysteresis loop for IrAl-MTJ blanket film with different in-situ annealing temperature. (c) and (d) Plot of resistance versus out-of-plane magnetic field with TMR results measured by CIPT from IrAl-MTJ blanket films with different in-situ annealing temperature.

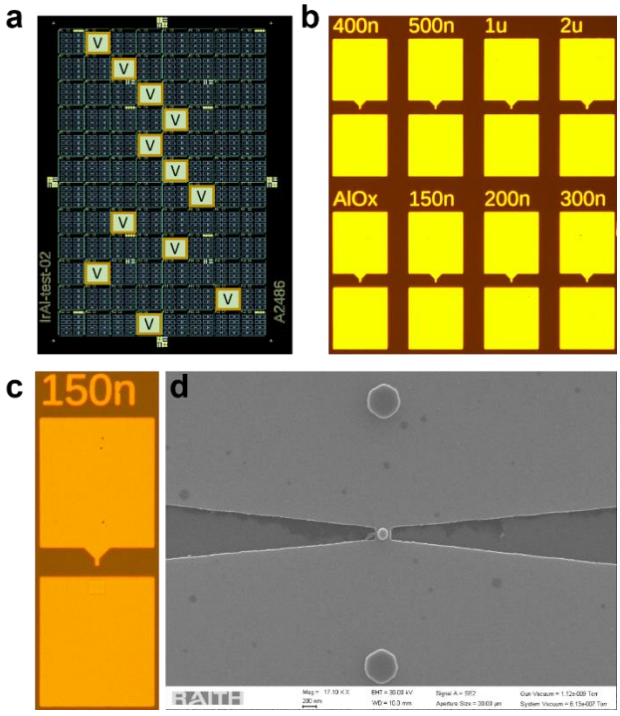

Figure 3.24 (a) Layout design for MTJ devices measurement. (b) and (c) Optical images of full MTJ devices structure design with different pillar size of MTJ. (d) Scanning electron microscopy images of MTJ devices.

a

R1C2		R2C3		R3C4		R4C5	
2um	300nm	2um	300nm	2um	300nm	2um	300nm
1um	200nm	1um	200nm	1um	200nm	1um	200nm
500nm	150nm	500nm	150nm	500nm	150nm	500nm	150nm
400nm	AlOx	400nm	AlOx	400nm	AlOx	400nm	AlOx

R5C4		R6C5		R7C6		R8C3	
2um	300nm	2um	300nm	2um	300nm	2um	300nm
1um	200nm	1um	200nm	1um	200nm	1um	200nm
500nm	150nm	500nm	150nm	500nm	150nm	500nm	150nm
400nm	AlOx	400nm	AlOx	400nm	AlOx	400nm	AlOx

R9C5		R10C2		R11C7		R12C4	
2um	300nm	2um	300nm	2um	300nm	2um	300nm
1um	200nm	1um	200nm	1um	200nm	1um	200nm
500nm	150nm	500nm	150nm	500nm	150nm	500nm	150nm
400nm	AlOx	400nm	AlOx	400nm	AlOx	400nm	AlOx

	Working MTJ (showing > 40% TMR)
	Shorted MTJ (showing low TMR)
	Not working MTJ (no TMR at all)

b

Nominal diameter	Success rate (12 sampling)	TMR max [%]	TMR median [%]	Nominal diameter	Success rate (12 sampling)	TMR max [%]	TMR median [%]
2um	5	86.82	26.31	300nm	9	75.04	52.49
1um	8	83.83	55.35	200nm	6	78.07	52.03
500nm	6	70.51	32.28	150nm	5	71.94	33.30
400nm	7	78.05	49.79				

Figure 3.25 (a) Statistic results of MTJ pillar device mapping of MTJ and (b) yield rate of MTJ with high TMR.

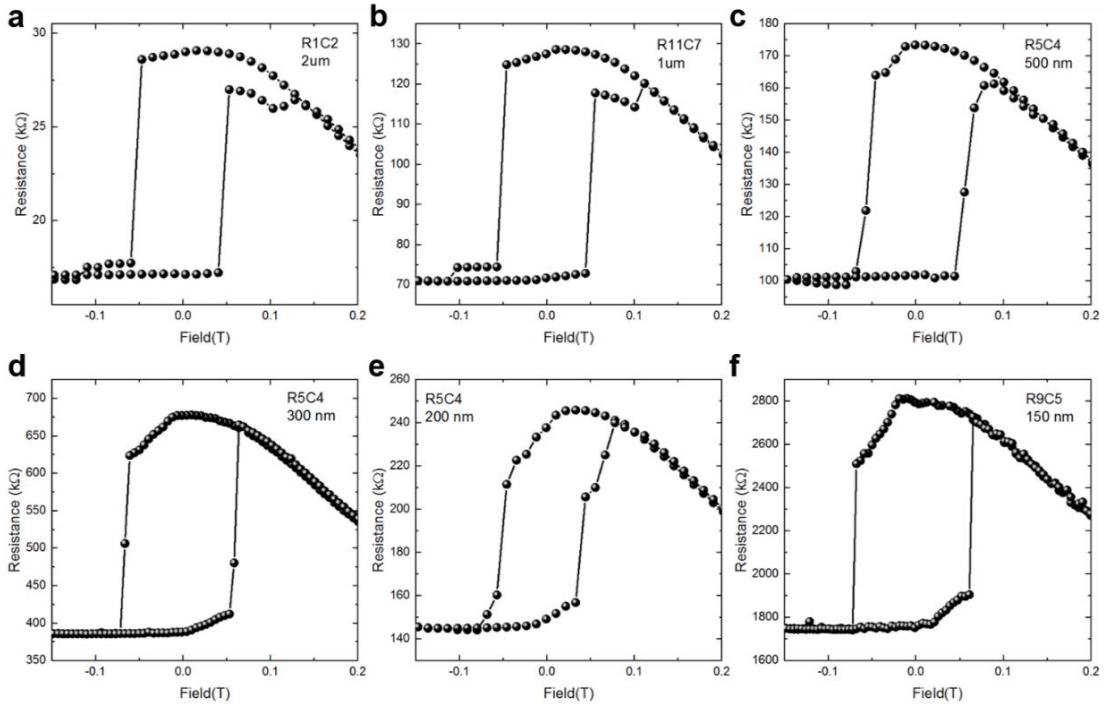

Figure 3.26 Plot of resistance of MTJ pillar with different diameter versus out-of-plane magnetic field.

Non-linear I-V characteristics in Figure 3.27b indicates the tunneling behavior of electron flowing through MgO tunnel barrier. Furthermore, the TMR linearly decreases as input voltage increasing, which suggests the MgO barrier is breakdown because of high input potential electric field. By applying continuous magnetic field pulses, the magnetization state is switch from parallel to antiparallel continuously shown in Figure 3.28. By extract the widen area of coercivity, according to formula:

$$P(\tau) = 1 - exp(-\frac{\tau}{\tau_0} exp(-\frac{E}{k_B T}(1 - \frac{H_p}{H_k^{eff}})^2)) \quad (4)$$

We can obtain the thermal stability factor Δ (E/k_BT) shown in Figure 3.28. The IrAl-MTJ structure shows reasonable thermal stability factor with $\Delta > 70$ k_BT, which suggests its promising application used for MRAMs.

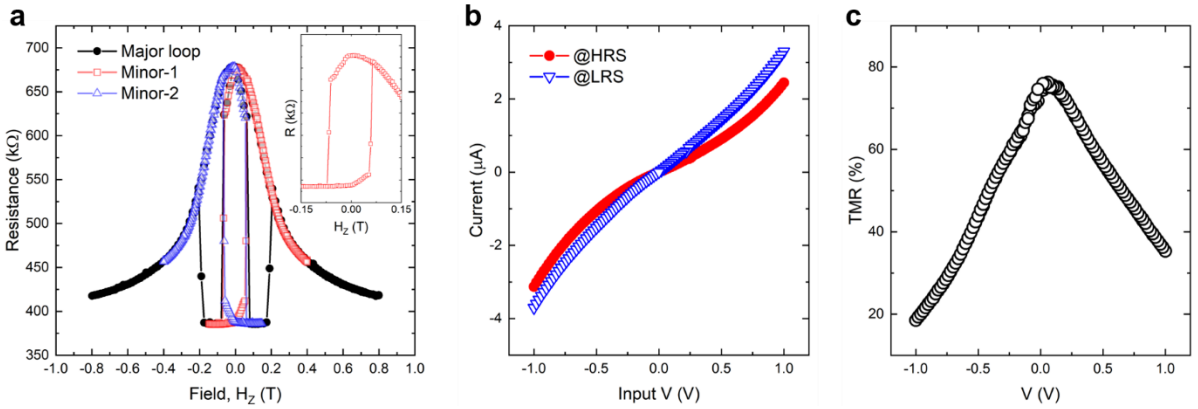

Figure 3.27 (a) Plot of resistance of IrAl-MTJ pillar with 300 nm diameter versus out-of-plane magnetic field. (b) *I* – *V* characteristics of IrAl-MTJ pillar. (c) Plot of TMR results versus input voltage.

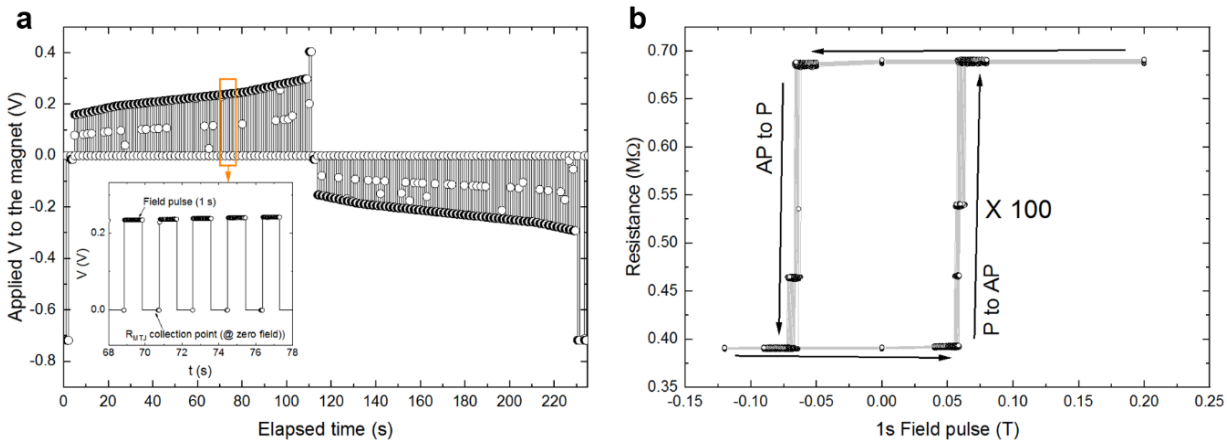

Figure 3.28 (a) Magnetic field pulses from input voltage into magnet. (b) Plot of resistance of MTJ versus field pusles.

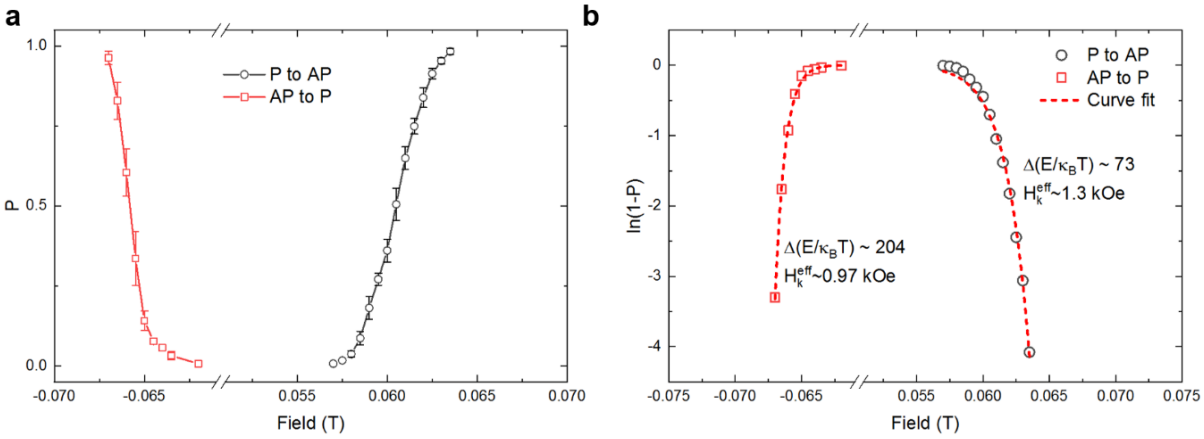

Figure 3.29 (a) and (b) plot of probability of magnetization switching versus out-of-plane magnetic field.

3.12 Summary

We built PMA films and synthetic antiferromagnets with [001] crystal orientation by using Co, $Co_{90}Fe_{10}$, Ni multilayer formed on top of Ir_xAl_{100-x} under layer as spin-orbit torque sources, which is used for racetrack memories. The maximum motion speed of domain walls reach ~ 1 km s^{-1} with a driving current density several times lower compare with that in previous report. The critical current density for domain wall motion in Ir_xAl_{100-x} – SAF structure is heavily dependent on the spin Hall conductivity of Ir_xAl_{100-x} under layer. The interfacial DMI, ratio of M_r / M_s and anisotropy field (H_k) plays important role in improving the performance of domain wall motion. Full MTJ films stack by using $Ir_{42}Al_{58}$ alloy thin film displays large TMR ~ 85% at room temperature, which shows promise of practical application for MRAMs. Furthermore, the successful growth of Ir_xAl1_{00-x} on top of Si wafer shows its compatible capability with CMOS technology.

4. Thin film structure design for skyrmions

4.1 Skyrmions concept

British theory scientist Tony Skyme came up with the concept of skyrmions in particle physics field to explain the non-linear sigma model with a solution from the point-of-view of topology [65]. Bogdanov and his collaborators predicted the existence of skyrmions can be realized in the ferromagnets with chiral lattice including the finite Dzyalonshniskii-Moriya interaction and the lack of inversion symmetry [66, 67]. The keen competition between Dzyalonshniskii-Moriya interaction and Heisenberg interaction in ferromagnets can give rise to various kinds of spin textures such as vortices, domain walls, bubbles, spirals, skyrmions, merons, and antiskyrmions et al [53]. These spin textures can be utilized as information carrier in rich varieties of memories. The skyrmions hosting materials have attracted more and more attention. Furthermore, the non-trival physics phenomenon from skyrmions has attracted great research interest from the point view of both science and practical device applications. For example, the domain walls and vortex can be driven by the spin-polarized current in ferromagnets and spin-orbit toques from adjacent strong spin-orbit coupling materials [68]. It is found these spin textures can be used in data storage devices like racetrack memories. In addition to these spin structures, the skyrmions, vortex-like swirling spin structures has a quantized topological number, which are attracting considerable attention because of their peculiar response to the external magnetic fields [69, 70]. A magnetic skyrmion comprise of spins pointing all directions wrapping a sphere similar as a hedgehog, which is shown in Figure 4.1a [71]. The number of such wrappings in Skyrmions corresponds to a topology invariant, therefore the skyrmions are topologically protected spin spiral textures, include the Bloch-type, Néel-type and antiskyrmion, which is shown in Figure 4.1 b, c and d [72 - 76]. Recently, the prediction of skyrmions has been experimentally discovered in chiral lattice ferromagnets such as *B*20 compounds without inversion symmetry (MnSi [69], FeGe [70], $Fe_{1-x}Co_xSi$ [77] et al.) and Copper oxoselenite Cu_2OSeO_3 [78]. Interfacial DMI generated at the interface between ultrathin ferromagnetic (FM) layers and materials with strong spin-orbit coupling (SOC) can host Néel type skyrmions with a diameter less than 100 nm at room temperature [79, 80]. The ultrathin thickness of multilayer of FM and strong SOC thin films pose the challenges for the technological application with concern of thermal stability. Centrosymmetric tetragonal magnet with triangular lattice displays very tiny skyrmion lattice (~ 2 nm) at low temperature (8 K) also biskyrmion discovered in centrosymmetric magnet [81, 82].

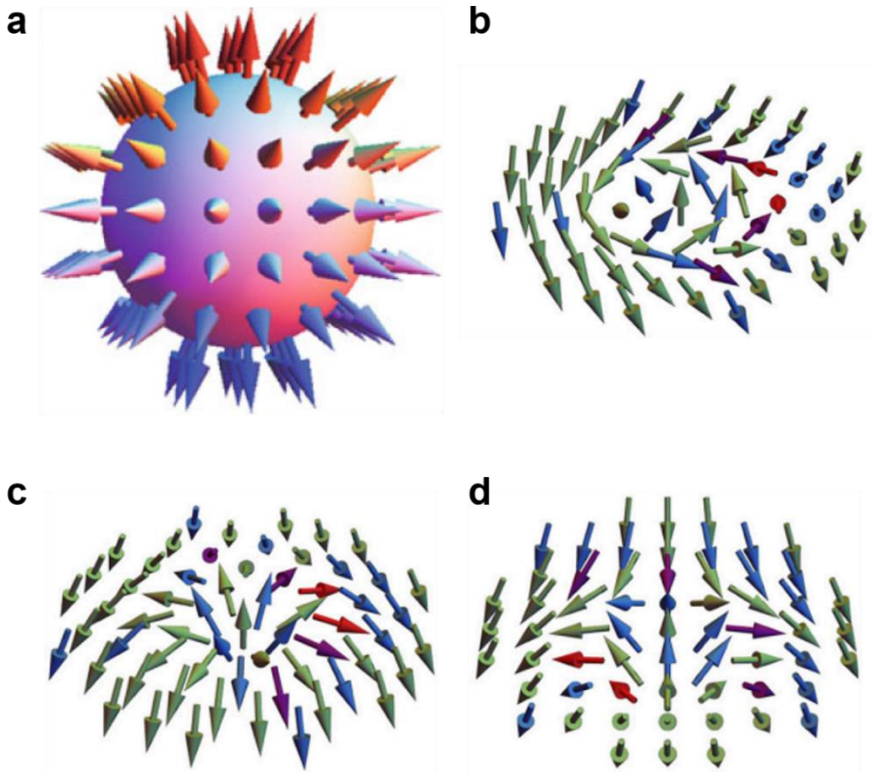

Figure 4.1 (a), Schematic of the original hedgehog-type skyrmion proposed by Tony Skyrme in the 1960s, whose magnetizations point in all directions wrapping a sphere. (b), and (c) Bloch and Néel skyrmions with topological charge Q = 1 and polarity *P* = 1. (d), Antiskyrmion with topological charge Q = -1 and *P* = 1. This figure is reploted from Ref [71].

4.1.1 Skyrmions in noncentrosymmetric magnets

The Dzyalonshinskii-Moriya interaction (DMI) in non-centrosymmetric magnets favors canted spin moment orientation because of inversion symmetry breaking. All materials hosting skyrmions with inversion symmetry breaking has been reported are chiral cubic ferro-/ ferrimagnets so far. One representative cluster of materials is a series of *B*20 alloys including such as MnSi [69], FeGe [70], $Fe_xMn_{1-x}Ge$ [83], $Fe_{1-x}Co_xSi$ [77] et al., which are metallic and / or semiconducting. The itinerant electron-mediated long-ranged interaction and DMI are two main mechanisms to explain the phenomenon about skyrmions. Another example is insulating Cu_2OSeO_3 [78], the magnetic Cu^{2+} ion with a distinctive sites, showing the local ferromagnetic arrangement among them. All these two systems are chiral cubic system, which belongs to cubic space group $P2_13$. The global symmetry and overall nature of Dzyalonshinskii-Moriya interaction are common in them. The breakthrough in skyrmions discovery in these crystal structures is that finding them in thin lamella cut from bulk crystal samples. The Lorentz transmission electron microscopy is employed for this purpose. When the electron beam pass through the magnetic samples, each electron slightly change their propagation route by the

*L*orentz force from the magnetization of samples. By taking over and under focused images, we can obtain the real-space distribution of spin moments of local magnetizations of crystals.

4.1.2 Skyrmions in centrosymmetric magnets

The skyrmions in centrosymmetric magnet is from the competition between magnetic dipole-dipole interaction and uniaxial magnetic anisotropy rather than Dzyalonshinskii-Moriya interaction. Magnetic dipole-dipole interaction also calls the dipole coupling, refers to the interaction between two magnetic dipoles [84]. Suppose $\mathbf{m_1}$ and $\mathbf{m_2}$ are two magnetic dipole moments that are far enough apart that they can be treated as point dipoles in calculating their interaction energy. The potential interaction energy *H* is given by:

$$A = \frac{\mu_0}{4\pi|r|^3}\,[3(\boldsymbol{m_1}\cdot\hat{r}\,)(\boldsymbol{m_2}\cdot\hat{r}\,) - \boldsymbol{m_1}\cdot\boldsymbol{m_2}] + \mu_0\frac{2}{3}\boldsymbol{m_1}\cdot\boldsymbol{m_2}\,\delta(\mathbf{r}) \qquad (1)$$

where μ_0 is the magnetic moment, **r** is a unit vector parallel to the line joining the centers of the two dipoles, and |**r**| is the distance between the centers of $\mathbf{m_1}$ and $\mathbf{m_2}$. Last term with δ- function vanishes everywhere but the origin, and is necessary to ensure that **B** vanishes everywhere. In conventional ferromagnets, the dipole - dipole interaction favors a closed loop of magnetization alignment, however the magnetic anisotropy prefer the out-of-plane spin point direction, the competition between the two interaction result in various kinds of spin textures. The formation of a cylindrical domain with magnetization inside (outside) pointing parallel (antiparallel) to the application of magnetic field is called magnetic bubble for a thin film with strong magnetic easy-axis anisotropy perpendicular to the sample plane, shown in Figure 4.1.2 a ,b and c. Thus the boundary of bubble is 180^o magnetic domain wall. When the domain wall is composed of Bloch wall with spin helicity sustaining through the cylindrical boundary, this magnetic bubble is called “soft bubble”. The soft bubble is considered as a type of skyrmion texture with a topological winding skyrmion number of -1. Skyrmions or soft bubbles have either type of spin helicity at random. Because of the spin helicity at random, the soft bubble can be moved by the gradient field. The existence and absence of the soft bubbles can be viewed as “0/1” in the storage of information used as bubble memories, which was commercialized in 1970 and 1980s. The recent advancement LTEM technique has revealed the several unique spin textures associated with soft bubbles i.e. skyrmions.

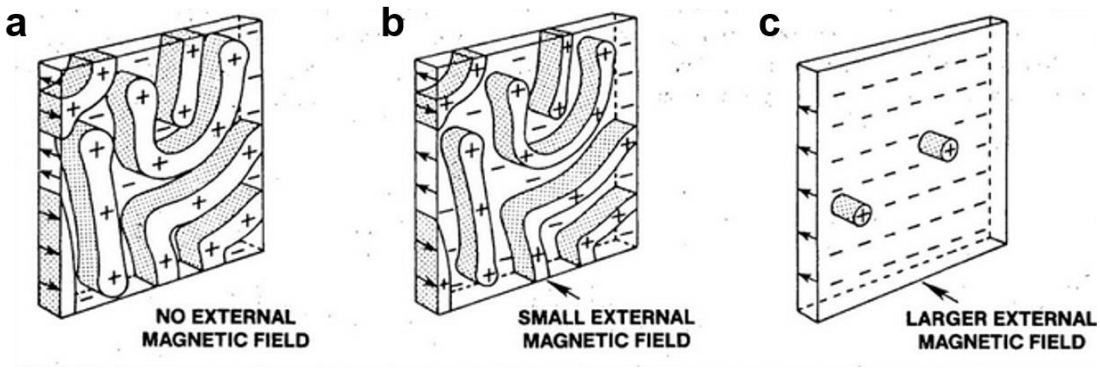

Figure 4.2 (a), (b) and (c) Schematic of magnetic bubble domain under the field.

For example, in the case of skyrmions in M-type hexaferrite $BaFe_{12-x-0.05}Sc_xMg_{0.05}O_{19}$ (x = 0.16), the spin texture at a cylindrical domain wall region shows Bloch-wall-like screw magnetisation rotation but with multiple helicity reversals [85]. The in-plane component of magnetization changes their spin rotation with the distance from bubble center shown in Figure 4.1.2 d - i. Another interesting example is bilayered perovskite $La_{2-2x}Sr_{1+2x}Mn_2O_7$; in this material, two skyrmions with opposite spin helicities spontaneously make a pair and form a molecule-like structure called a biskyrmion shown in Figure 4.1.2 j-m [86]. When neighbouring skyrmions has the same spin helicity, the overlap area causes the magnetization in an antiparallel manner over a short distance, thereby causing a large increase in exchange energy. This difference makes the observed the biskyrmion spin texture relatively stable. Because each single-skyrmion particle has a skyrmion number of -1, the skyrmion number of a biskyrmion is -2. Biskyrmions further form an anisotropic triangular lattice spontaneously and can be driven by external electric current two orders of magnitude smaller ($< 10^8$ A m^{-2}) than that for a conventional ferromagnetic domain wall.

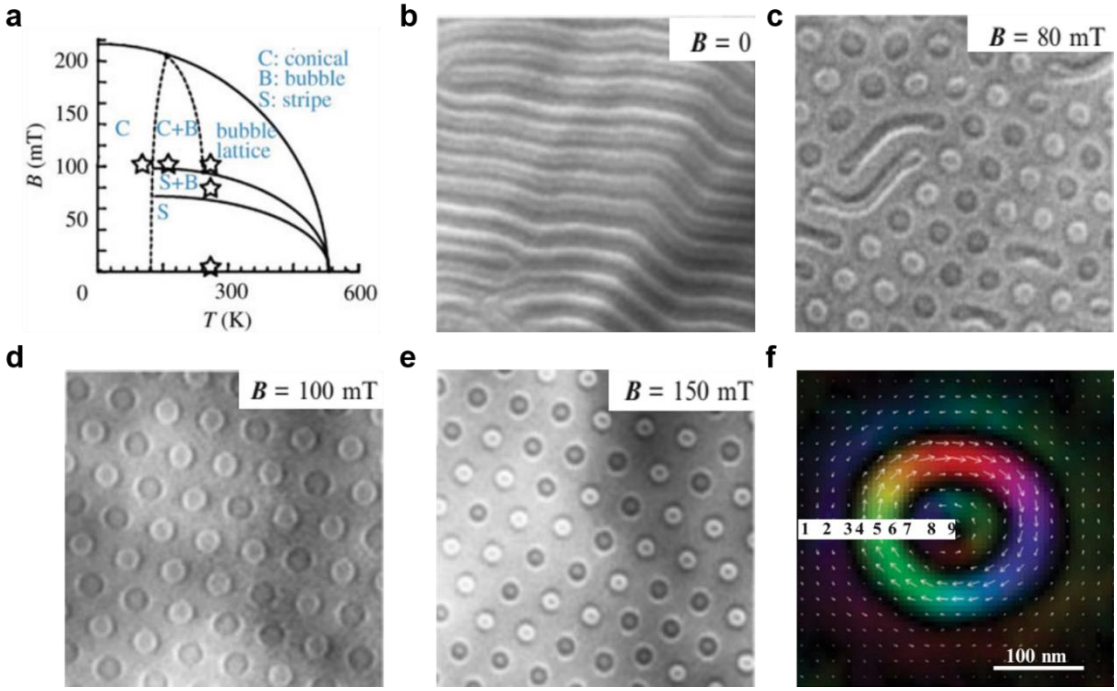

Figure 4.3 LTEM data for $BaFe_{12-x-0.05}Sc_xMg_{0.05}O_{19}$ ($x = 0.16$). (a) Temperature versus magnetic field phase diagram of magnetic domain structure. (b) – (e) Magnetic field dependence of domain structure at room temperature, where B is normal to (001) plane of the sample. (f) Lateral magnetization distribution for the observed skyrmion (*soft bubble*). This figure is replotted from Ref [85].

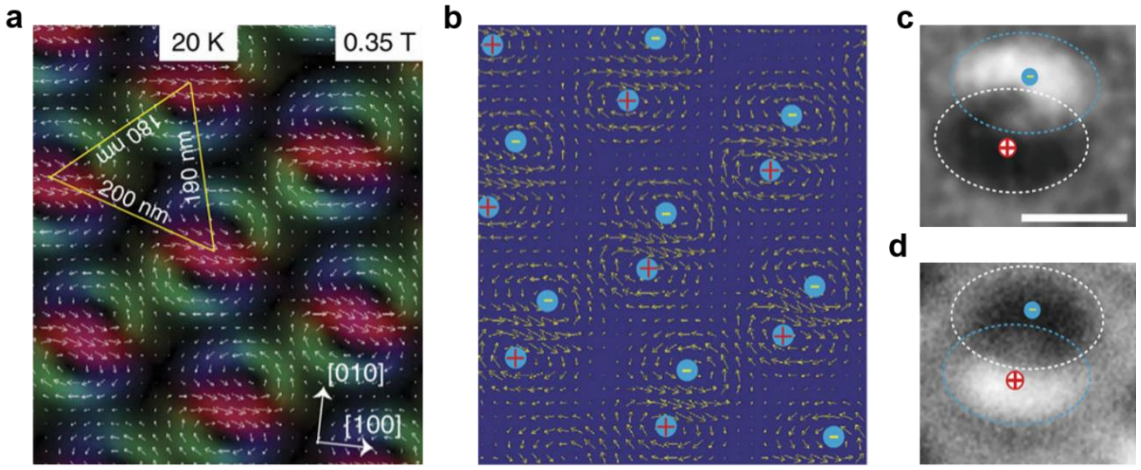

Figure 4.4 LTEM data for $La_{2-x}Sr_{2+x}Mn_2O_7$ (a) Lateral magnetization distribution for a biskyrmion lattice derived from the TIE analysis of LTEM data. (b) The in-plane magnetic component (yellow arrows) distribution in the biskyrmion lattice. (c) Over-focused and (d) under-focused LTEM images. This figure is replotted from Ref [86].

4.1.3 Skyrmions in multilayer thin films

Interfacial Dzyaloshinskii-Moriya interaction exist in between ultrathin ferromagnetic materials and adjacent films with strong spin-orbit coupling can stabilize the non-collinear spin

textures like Néel skyrmion et al. For example, these include multilayer of Co/Pd [48], [Ir/Fe/Co/Pt] × n [79], [Pt/Co/Ta] × n, [Pt/CoFeB/MgO] × n [87] and monolayer, bilayer cases like Fe monolayer on top of Ir (111) surface [88] and a (ii) PdFe bilayer on an Ir (111) surface [89]. The large lattice mismatching between Co and Pd give rise to the symmetry breaking at interfaces and provide a mechanism for non-zero DMI to stabilize Néel skyrmion shown in Figure 4.5. By utilizing the opposite sign of DMI for FM sandwiched by different SOC materials, sub-50 nm skyrmion is achieved in Ir/Fe/Co/Pt multilayer with tunable properties at room temperature shown in Figure 4.6. The motion of skyrmion is driven by the bipolar current pulse has been observed in Pt/Co/Ta and Pt/CoFeB/MgO multilayer stack because of large spin Hall effect and high spin-orbit torque efficiency shown in Figure 4.7. The ultrathin Fe (PdFe) layer provides magnetic moments with a ferromagnetic exchange interaction and Ir underlayer can lead to strong spin-orbit coupling because of large nuclear number, which can serve as a source of Dzyaloshinskii-Moriya interaction. Because the magnitude difference of magnetic moments in these two different materials system, each system shows distinctive resultant spin texture under the development of an external magnetic field. The spin-polarized scanning tunneling microscopy has been employed to explore the detail of the spin texture at the surface of a magnetic mono/bilayer. The tip used for measurement is magnetized along some specific direction and spin-polarized tunneling current scales as the cosine of the angle between the tip and the magnetization of the sample shown in Figure 4.8. The pioneering work by Wiesendanger et al. for a Mn monolayer on a W (110) surface reveal the emergence of a helical spin texture of fixed spin helicity with the period of 12 nm, which confirms the importance of the Dzyaloshinskii-Moriya interaction at the surface or interface [90].

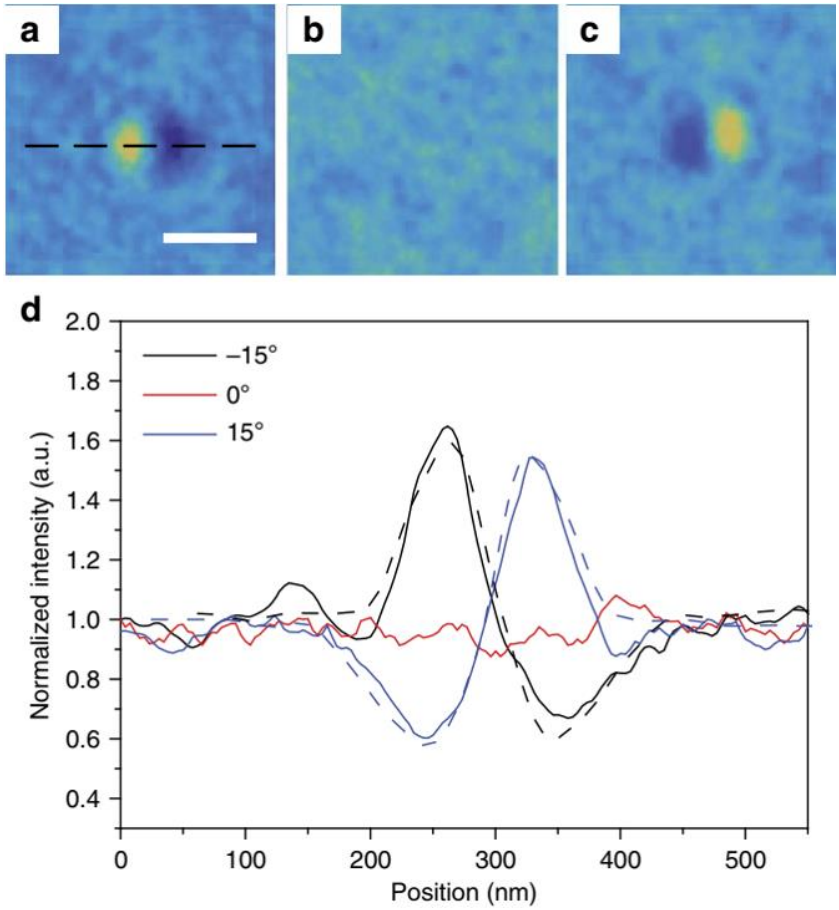

Figure 4.5 Experimental L-TEM images of a Néel skyrmion at varying tilt angles. (a - c) Tilt sequence of a magnetic skyrmion with a radius of 90 nm, taken at (a) -15^{o}, (b) 0^{o} and (c) 15^{o} of tilt showing the disappearance of contrast at 0^{o} tilt and reversal of contrast for opposite tilt angles. The tilt axis is indicated by the dashed line with a scale bar of 200 nm. (d) Line profiles of the three images, along the direction of the dashed line in a, showing the difference in contrast. The direction of asymmetry (bright-dark or dark-bright) in indicative of the skyrmion polarity. In this case, the imaged skyrmion polarity is +1. The skyrmion extent is determined by the distance between the maximum and minimum for the tilted samples. The dashed lines correspond to simulated intensity profiles of an 86 nm skyrmion, showing good qualitative agreement. This figure is replotted from Ref [48].

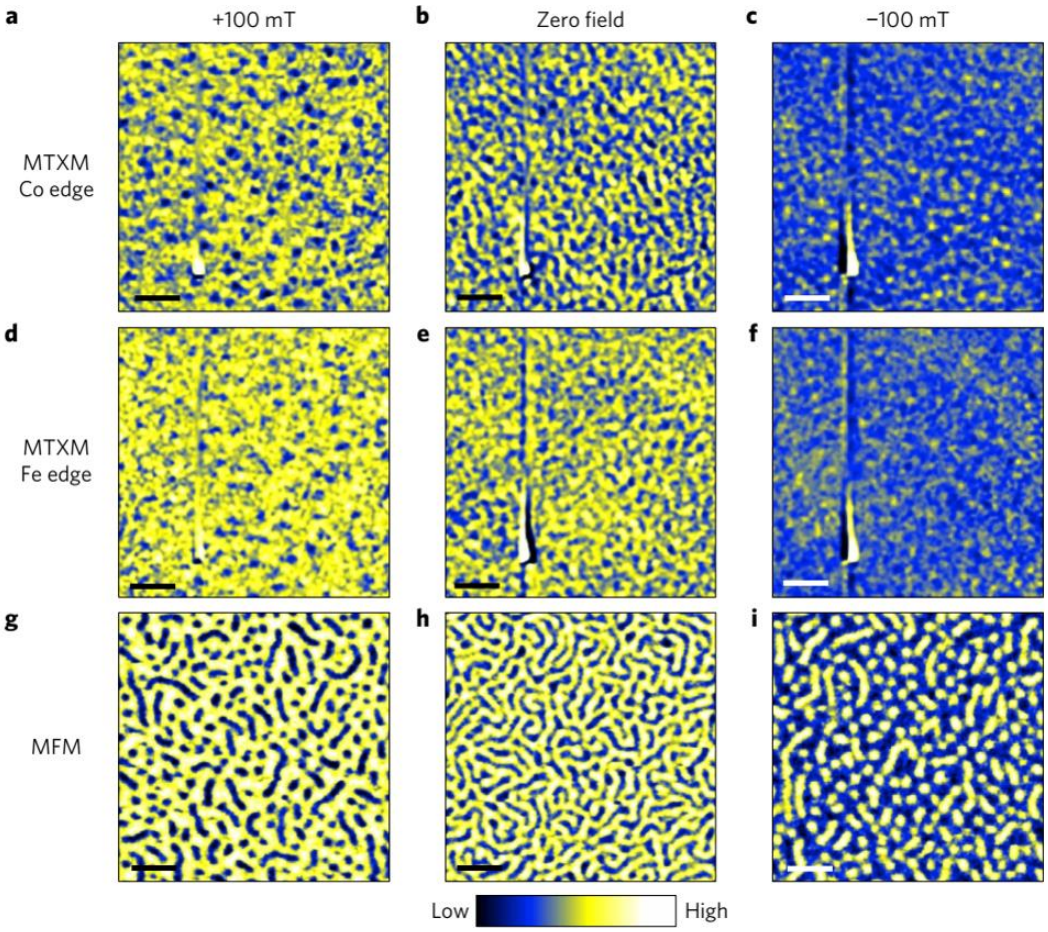

Figure 4.6 Magnetic microscopy of RT skyrmions. a – i, Microscopic imaging (scale bar, 0.5 μm) of sample Fe (3) / Co (6) at RT with MTXM (on Si_3N_4 membrane) at the Co L_3 edge (a-c), MTXM at the Fe L_3 edge (d-f), over the same sample edge (a-c), and with MFM (on SiO_2 substrate, g-i). Images shown are acquired at ~ +100 mT (a,d,g), 0 T (b,e,h) and ~ -100 mT (c,f,i), respectively, after saturation at ~ +250 mT, and display similar evolution in magnetic contrast with applied field. A dead pixel on the MTXM CCD (a-f: bottom left) does not affect our analysis. This figure is replotted from Ref [79].

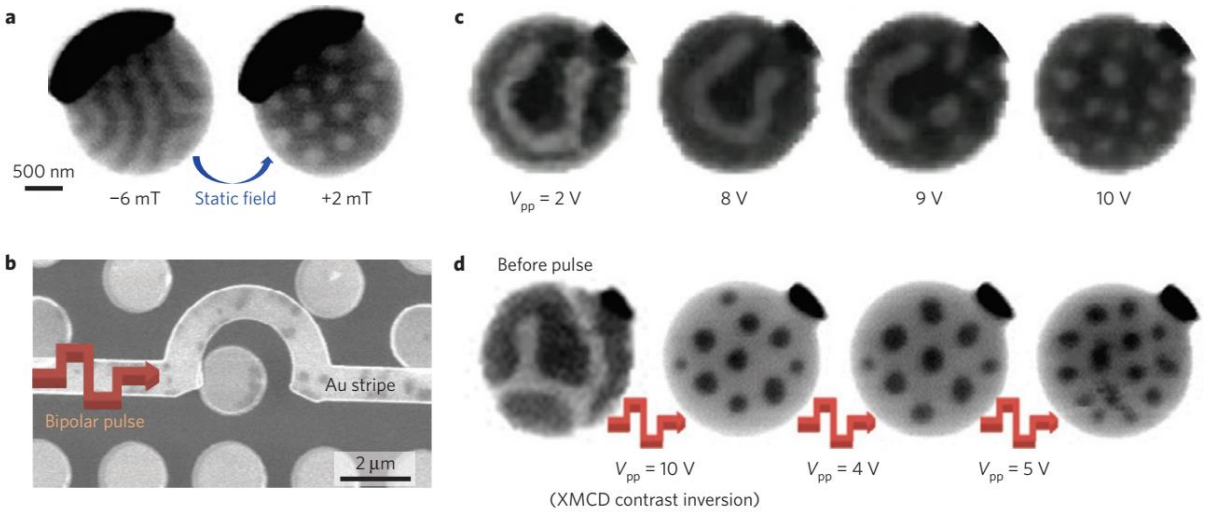

Figure 4.7 a, STXM images of the domain state in a 2 µm Pt/Co/Ta disc at B_z = -6 mT (left) and after subsequently applying B_z = 2 mT (left). b, Scanning electron micrograph of a magnetic disc array with a Au microcoil patterned around one disc. c, Sequence of STXM images after applying bipolar pulse trains (peak-to-peak voltage amplitude V_{pp}) with microcoil, showing transformation from labyrinth stripe domain into skyrmion lattice. d, An initial labyrinth state was generated by static field (first image) and then transformed into a hexagonal skyrmion by applying a bipolar pulse train with V_{pp} = 10 V (second image). The last two images were acquired after applying V_{pp} = 4 V, and V_{pp} = 5 V, respectively. Dark (light) contrast corresponds to up (down) magnetization in all STXM images except for the last three in d, where the X-ray magnetic circular dichroism (XMCD) contrast was inverted. This figure is replotted from Ref [87].

Furthermore, they discovered the formation of a lattice square of skyrmions (with skyrmion number +1) for the Fe / Ir (111) system by taking the SP-STM images with different directions of tip magnetization. Without external magnetic field, the unique skyrmion spin texture also appears and characterized by two orthogonal magnetic modulation vectors. This typical size of square skyrmion is as small as ~ 1 nm, with the underlying crystalline lattice. The short-ranged four-spin interaction as well as the Dzyaloshinskii-Moriya interaction play crucial roles in the stabilization of observed skyrmion lattice [71].

$$\mathcal{H}_{four} = \sum_{ijkl} K_{ijkl} [(\mathbf{M_i} \cdot \mathbf{M_j})(\mathbf{M_k} \cdot \mathbf{M_l}) + (\mathbf{M_i} \cdot \mathbf{M_l})(\mathbf{M_j} \cdot \mathbf{M_k}) - (\mathbf{M_i} \cdot \mathbf{M_k})(\mathbf{M_j} \cdot \mathbf{M_l})] \quad (2)$$

the magnetic behavior of PdFe/Ir (111) system is different from chiral-lattice ferromagnetic films. The system shows a helical spin order with a spin modulation period of 6 ~ 7 nm in the absence of external magnetic field,. When the field H is ~ 1.4 T normal to the film leads to the formation of a hexagonal lattice of skyrmions, furthermore, the increase of B (> 2 T) stabilizes the uniform ferromagnetic state, while the single skyrmion is often survived through the pinning of atomic defects shown in Figure 4.9. Notably, when B is tuned around the phase boundary between ferromagnetic and skyrmion spin states, the local injection of electron current through a ferromagnetic tip can enable the generation and deleting of single magnetic skyrmions. The probablity of skyrmion formation after current injection depends on the sign and magnitude of applied electric current. The above procedures enable the local “writing” and “reading” of individual skyrmion particles of an extremely small size, i.e. less than 10 nm, which demonstrates the potential of magnetic skyrmions as information carrier in the high density magnetic logic storage memories devices. Furthermore, skyrmions can also be stabilized at room temperature in ultrathin oxides bilayer like $BaTiO_3$ / $SrRuO_3$ [91], $SrIrO_3$ / $SrRuO_3$ [92]. Moreover, skyrmions or skyrmion bubble has been found in two-dimensional materials like Fe_3GeTe_2 [93], and bilayer of WTe_2 / Fe_3GeTe_2 [94] because of defects, layered crystal structure and interfacial DMI.

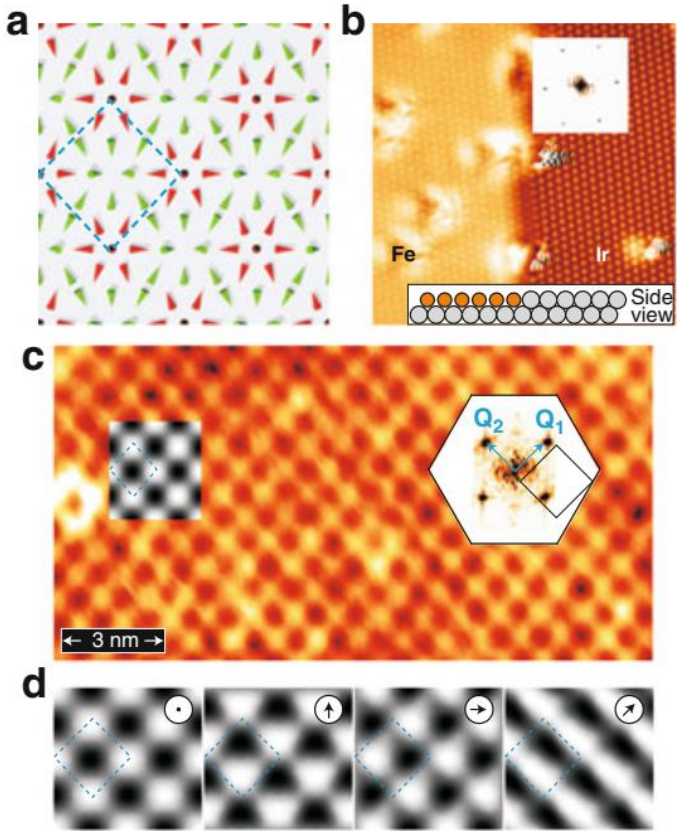

Figure 4.8 Skyrmion lattice observed by a spin-polarised scanning tunneling microscopy (SP-TEM) measurement for the Fe monolayer on Ir(111). (a) Sketch of the nanoskyrmion lattice: cones represent atoms of a hexagonal Fe layer and point along their magnetization directions; *red* and *green* represent up and down magnetization components, respectively. (b) Atomic-resolution STM image s of a pseudomorphic hexagonal Fe layer at an Ir step edge. *Upper inset*: The Fourier-transformed image. Lower inset: A side view of the system. (c) and (e) SP-STM images obtained with a tip magnetized along the (c) out-of-plane and (e) in-plane directions, respectively. Bright (dark) spots indicate areas with magnetization parallel (anti-parallel) to tip magnetization. In the latter case, images corresponding to three 120^{o} rotational domains are obtained for different square regions shown in *upper panel*. The tip magnetization direction is indicated by arrows. In (c), the Fourier transformation of the experimental SP-STM image is also indicated. (d) Simulations of SP-STM images of a skyrmion lattice with the tip magnetized in different directions as indicated. Here, the image size and unit-cell position are identical to those in (a). Simulated patterns are also overlaid on experimentally obtained images (c) and (e), which agree well with each other. This figure is replotted from Ref [88].

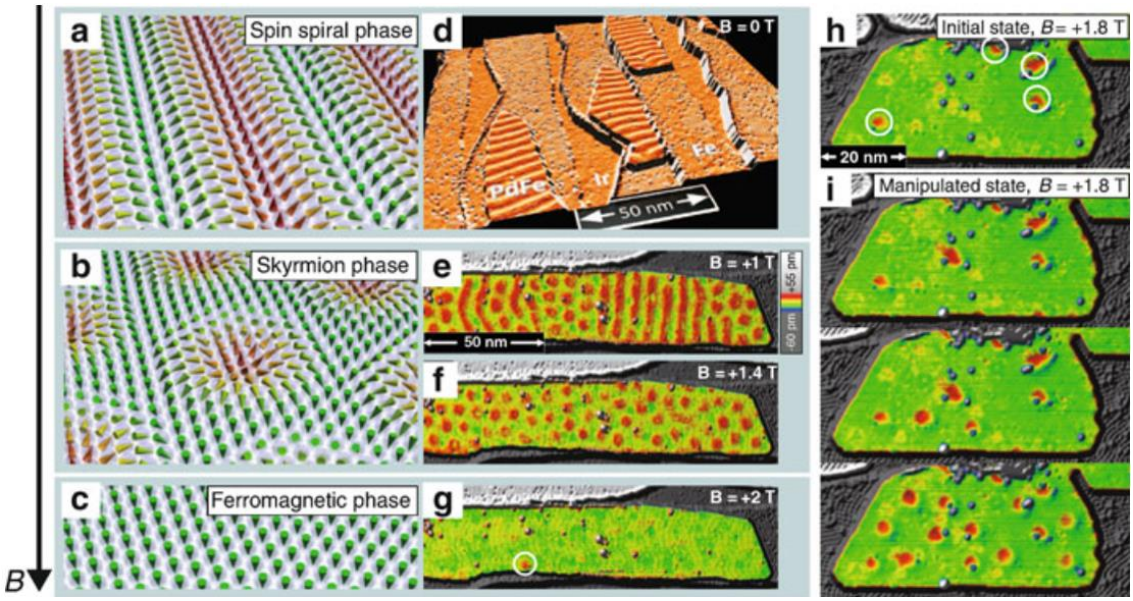

Figure 4.9 Magnetic field dependence of a PdFe bilayer on the Ir (111) surface at 8K. (a) – (c) Perspective sketches of magnetic phases. (d) Overview image obtained by SP-STM, perspective view of constant-current image colorized with its derivate. (e) – (g) Distribution of the out-of-plane component of magnetization for a PdFe bilayer at different magnetic fields along the out-of-plane direction. (e) Coexistence of spin spiral and skyrmion phases. (f) Pure skyrmion phase. (g) Ferromagnetic phase. A remaining skyrmion is marked on by the *while circle*. In (h) and (i), the manipulation of magnetic states by a local current injection through a magnetic tip is demonstrated at 4.2 K. (h) SP-STM image of the initial state at B = +1.8 T after sweeping the magnetic field down from +3 T. Four skyrmions are marked by *circles*. (i) Scuccessive population of an island with skyrmions by injecting higher-energy electrons through local voltage sweeps. This figure is replotted from Ref [89].

4.2 Skyrmions in Co_xAl films

4.2.1 Crystal structure, magnetic and electrical properties of Co_xAl films

CsCl type *B*2 cubic AB intermetallics compound is widely used in various fields such as structural materials [95], corrosion resistant coatings [96], high temperature thermal barrier coating [97], spin-orbit torque sources, chemical templating layer [98] et al.. IBM group reported by using nonmagnetic *B*2 structure CoX (X = Al, Ga, Ge and Sn) as chemical templating layer to grow unit cell thick binary Mn_3Sn (Sb, Ge) Heusler thin film with perpendicular magnetic anisotropy [98]. The *B*2 CoAl, $L1_2$ Co_3Al, as well as Co_xYAl ternary compound crystal structure schematic is shown in Figure 4.10 a with $x > 1$ and Y can represent Co and / or some other transition metal element.

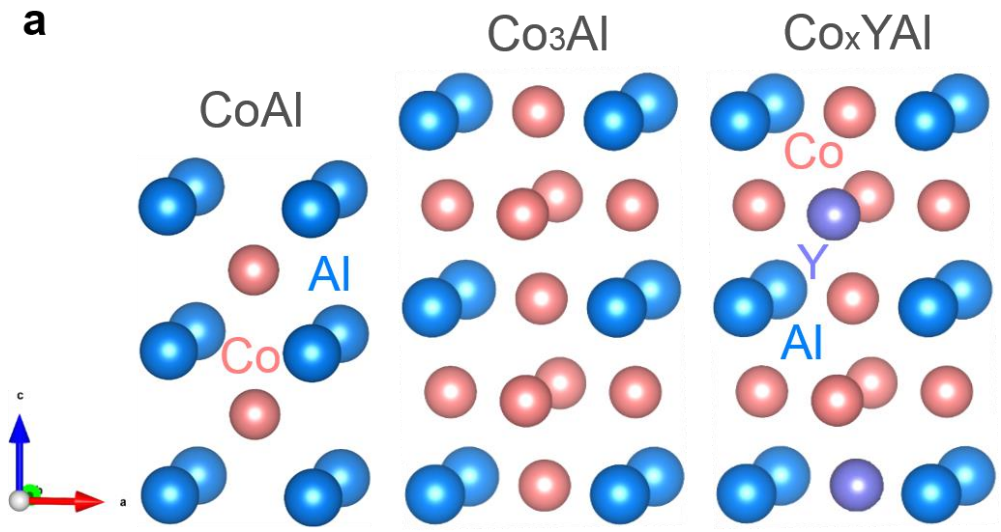

Figure 4.10 a Schematics of structure transition from nonmagnetic *B*2-CoAl to ferromagnetic $L1_2$ Co_3Al and Co_xYAl with [010] viewing direction.

As more Co atoms added inside *B*2-CoAl structure, the structure changes from *B*2 to $L1_2$. Furthermore, 5*d* transition metal elements like Pt and Ir can also be doped into to increase strength of spin-orbit coupling. We use (001) orientation MgO substrate to grow Co_xAl with different composition by co-sputtering from Co and Al targets separately. By tuning the power, the composition ratio between Co and Al is changed from 1 to 2.9. We grew 30 nm Co_xAl thin films with 5 nm TaN as capping layer to prevent it from oxidation. The out-of-plane magnetization hysteresis loop for 30 nm Co_xAl (x = 1.75, 2.15, 2.3 and 2.9) is shown in Figure 4.11 a and b. *M* (H) loop of Co_xAl films shows perpendicular magnetic anisotropy with spin spiral along *z* axis. From magnetic hysteresis loop, we know that Co_xAl films are ferromagnetic with saturated magnetization larger than 400 emu/cc. The saturation magnetization M_s increases from 400 to 780 emu/cc with very tiny coercivity as *x* varying from 1.75 to 2.9.

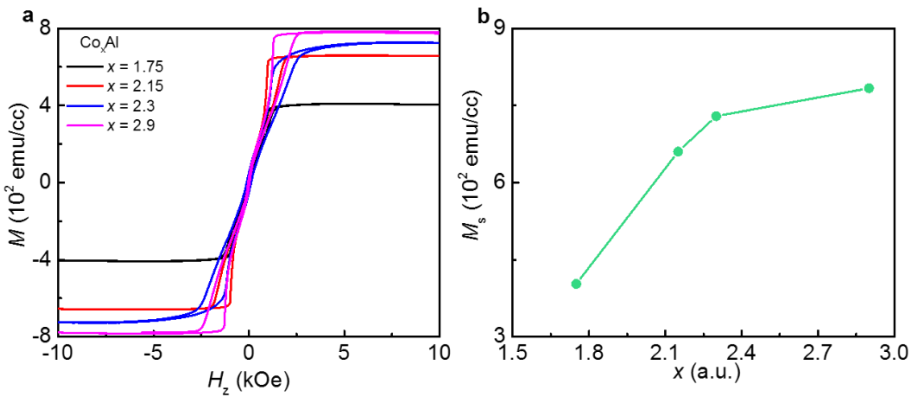

Figure 4.11 (a) Out-of-plane magnetization hysteresis loop of 30 nm Co_xAl. (b) Plot of saturation magnetization versus *x*.

We choose $Co_{2.3}Al$ compound as our target goal to investigate its electronic and magnetic properties. We changed the thickness of $Co_{2.3}Al$ film from 3 to 30 nm then we measured its magnetic hysteresis loop and electronic transport properties. The XRD results of thickness dependent $Co_{2.3}Al$ thin films is shown in Figure 4.12 a. We have calculated the out-of-plane lattice parameter *c* and grain sizes of $Co_{2.3}Al$ films by using Bragg's law and Laue equation shown in Figure 4.12 b. The size of grain increases from ~ 5.3 to 10 nm with *c* increasing from 2.75 to 2.77 Å.

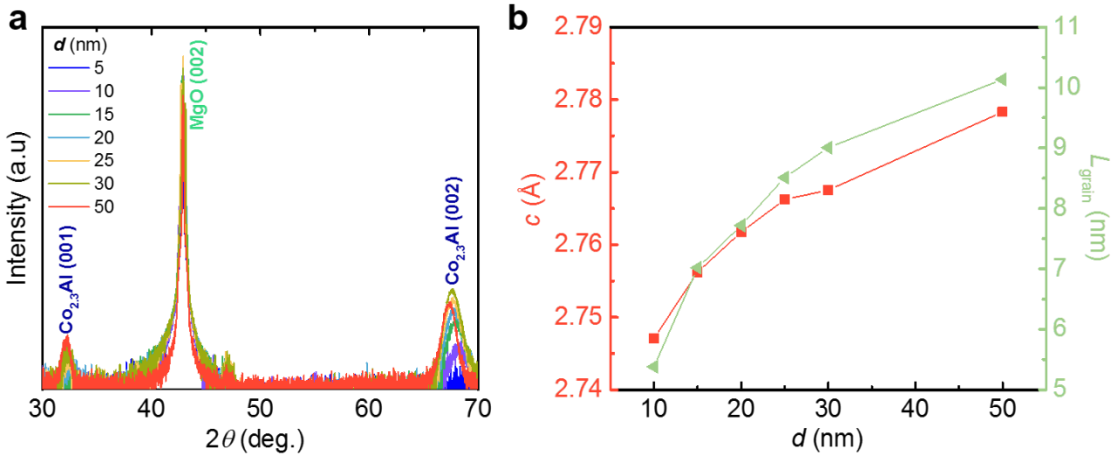

Figure 4.12 (a) XRD curve of $Co_{2.3}Al$ films with different thickness. (b) Plot of out-of-plane lattice parameter *c* and the size of grains versus thickness of $Co_{2.3}Al$ films.

The out-of-plane magnetic hysteresis loop of thickness dependent $Co_{2.3}Al$ thin films is shown in Figure 4.13a. $Co_{2.3}Al$ shows strong perpendicular magnetic anisotropy when *d* is 3 nm with a large saturation magnetization of 800 emu/cc. M_s changed from 800 to 950 emu/cc with thickness increasing from 3 to 10 nm, then M_s gradually decreases with thickness increasing. Hall resistivity of thickness dependent $Co_{2.3}Al$ thin films is displayed in Figure 4.13c. Hall resistivity gradually decreases with thickness increasing.

To determine Hall resistivity as a signature of skyrmion, we perform magnetotransport measurements by Van-der-Pauw method with the same 30 nm $Co_{2.3}Al$ film used in VSM measurements. We took the great care to eliminate the field offset from the electrical transport and magnetization hysteresis loop. The contributions for accounting ρ_H contain three components, defined by:

$$\rho_H = \rho_{OHE} + \rho_{AHE} + \rho_{THE} \quad (1)$$

ρ_{OHE} is from ordinary Hall effect caused by Lorentz force on carriers, presented by R_0H, R_0 is the conventional Hall coefficient. While ρ_{AHE} is the contribution from anomalous Hall effect

including the side-jump, skew scattering and intrinsic Berry curvature, represented by R_sM (H), R_s is the anomalous Hall coefficient, M (H) is the magnetization data obtained from VSM measurements. The topological Hall resistivity originates from the conduction electrons experienced through the effective magnetic flux generated by non-collinear spin textures [99]. By analyzing the Hall resistivity, we substract the ρ_{OHE} by fitting the slope at high field to obtain R_0 (See Figure 4.14a). ρ_{AHE} is fitted by fitting M (H) loop in Figure 4.14b then we derived R_s by the ratio between $\rho_{AHE+THE}$ and M (H) at saturated field showing no spin textures. The difference between ($\rho_{AHE+THE}$) and ρ_{AHE} is shown in Figure 4.13e. By minusing the ρ_{AHE}, then we derived topological Hall resistivity ρ_{THE}. We observe a maximum topological Hall resistivity peak of ~ 0.1 μΩ cm in the finite magnetic field range. The ρ_{THE} curve shows the typical hump shape with small magnitude at zero field, which corresponds to one dimensional magnetic domain stripes shown in Figure 4.13f.

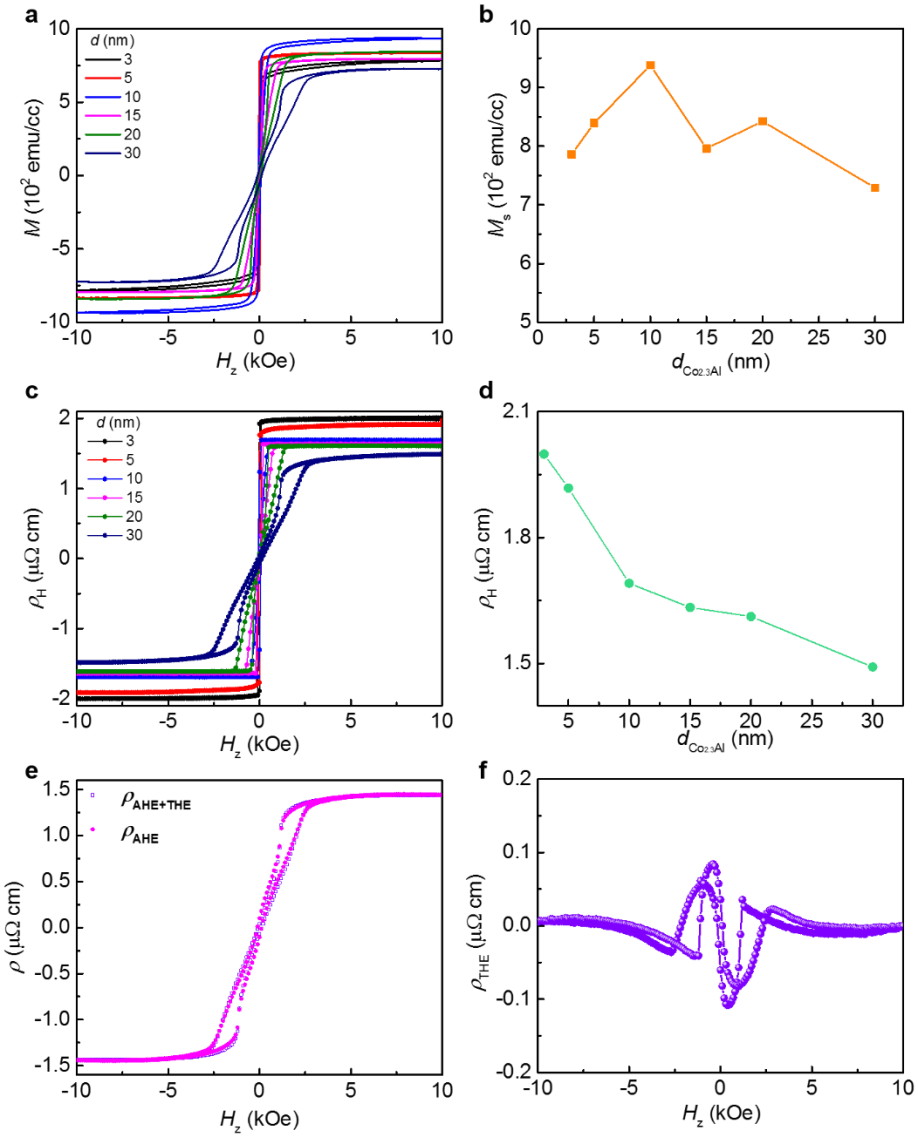

Figure 4.13 (a) Out-of-plane magnetization hysteresis loop of $Co_{2.3}Al$ films with different thickness. (b) Plot of saturation magnetization versus thickness for $Co_{2.3}Al$ films. (c) Hall resistivity of $Co_{2.3}Al$ films with different thickness measured within the interest range of the field. (d) Plot of Hall resistivity versus thickness for $Co_{2.3}Al$ films. (e) Comparison between the sum of anomalous and topological Hall resistivity ($\boldsymbol{\rho}_{AHE+THE}$) and anomalous Hall resistivity ($\boldsymbol{\rho}_{AHE}$) at 300 K. (f) Topological Hall resistivity extracted from the difference between $\boldsymbol{\rho}_{AHE+THE}$ and $\boldsymbol{\rho}_{AHE}$.

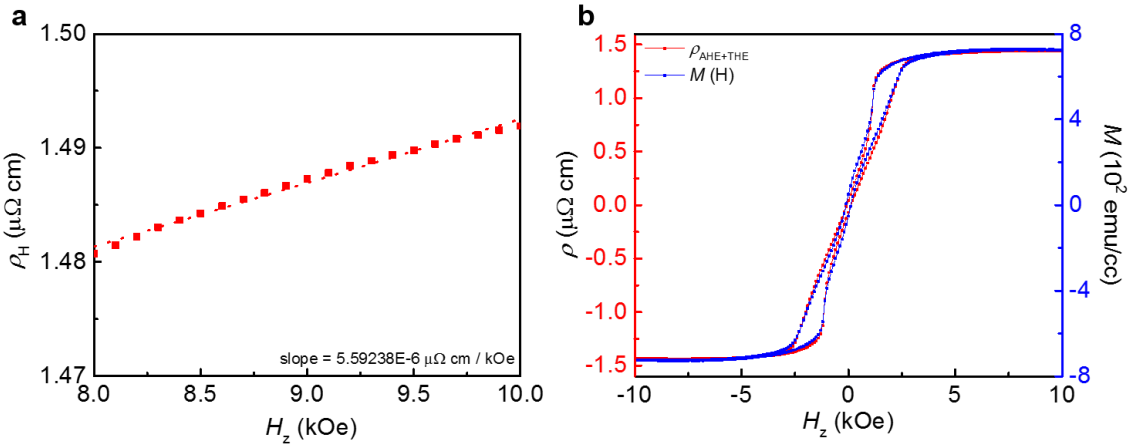

Figure 4.14 (a) Linear fitting between ρ_H and magnetic field. (b) The plot of ρ_H and magnetic hysteresis loop M (H) as a function of out-of-plane magnetic field.

4.2.2 Magnetic spin textures of 30 nm $Co_{2.3}Al$ film

The significant ρ_{THE} suggests it may exit non-collinear spin textures in centrosymmetric $Co_{2.3}Al$ films. Figure 4.15 a – h show the representative magnetic microscopy images recorded at 300 K with varying out-of-plane field, imaging by magnetic force microscopy (MFM). We have observed the labyrinth magnetic domain structure with zero field in Figure 4.15. Dark and bright regions correspond to the magnetization pointing up and down, which is parallel and antiparallel along z axis. The dark area gradually enlarge with field increasing, and the labyrinth is broken into isolated round nano spin objects at high field, which is shown in Figure 4.15 e, f and g. Figure 4.15h shows the magnetic saturated state of $Co_{2.3}Al$ films achieved at 3.5 kOe. The size of nano objects varies from 300 to 100 nm, which is dependent on the field.

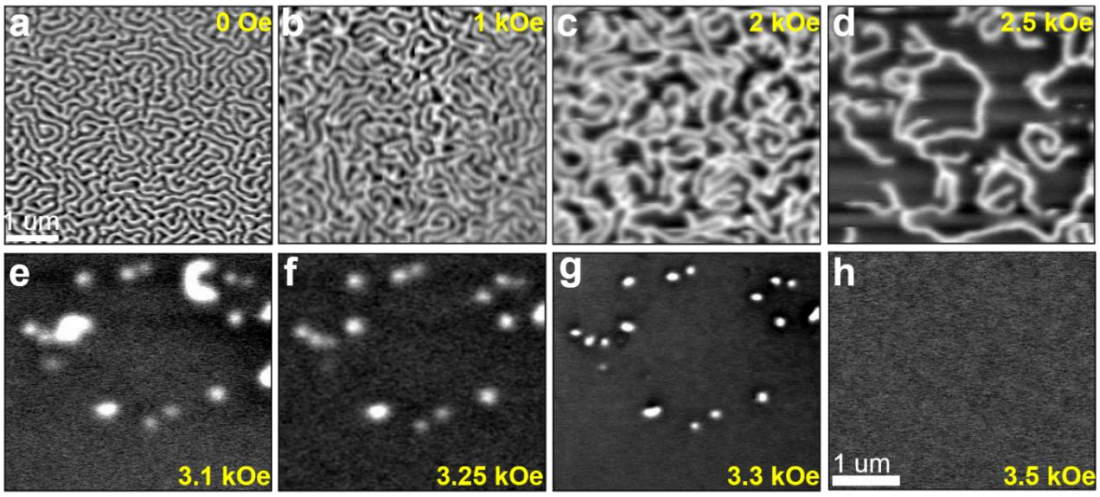

Figure 4.15 Evolution of the magnetic spin textures as the magnetic field increased from 1 to 3.3 kOe and finally to the field polarized state at 3.5 kOe in (h), all the field is applied along z axis perpendicular to the sample. The bright and dark contrast correspond to magnetization up and down domains respectively. The scale bar is given in (a) and (h).

In order to obtain the real space spin textures of $Co_{2.3}Al$ thin film, we perform the under-focused Lorentz-TEM (L-TEM) experiments using the plane view lamella prepared by conventional Ar-ion milling. Since L-TEM is also sensitive to the in-plane component, which is distinct from MFM. The magnetic field is applied along *z* axis which is normal to the sample plane and the under focus distance is 1.5 mm. The helical stripe domain with frequent magnetic reversal showing a periodicity of λ = 130 nm observed in the absence of field at room temperature. When the field increased to 2.56 kOe, the helical stripes is break into circularly shaped fragments with random distribution. As field is up to 2.88 kOe, the density of fragments decreases. To scrutinize the detailed structure of the spin texture, the magnified picture of red square identified objects from Figure 4.16 d with analysis is shown in Figure 4.16e. We can confirm this nano object is skyrmion bubble discovered in centrosymmetric $Co_{2.3}Al$ films, which can be stabilized by the competition between itinerant electron-mediated long-ranged interaction and perpendicular magnetic easy-axis anisotropy. The normalized size of skyrmion bubble is around 100 nm. Since, an interesting question emerging "Is there any possibility to stabilize Néel skyrmion in centrosymmetric magnetic material with strong interfacial spin-orbit coupling from under layer?"

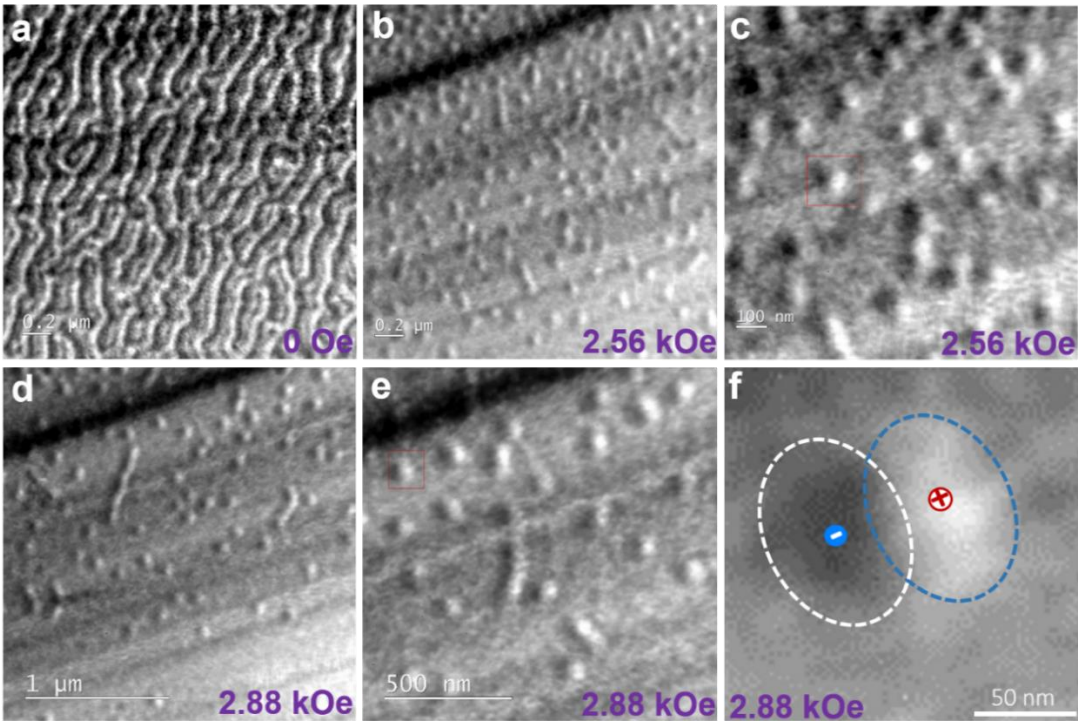

Figure 4.16 (a), (b), and (c) Under-focused (1.5 mm) Lorentz-TEM images recorded room temperature with perpendicular field of 0 Oe (a), and (b and c) 2.56 kOe for 30 nm $Co_{2.3}Al$ thin film. The scale bar is given inset the image. (d), and (e), Under-focused (1.5 mm) Lorentz-TEM images recorded room temperature with perpendicular field of 2.88 kOe, and (f) is the magnified picture of red square identified spin texture in (e).

4.3 IrAl / $Co_{2.3}Al$ bilayer structure

4.3.1 Crystal structure, magnetic and electric properties of IrAl / $Co_{2.3}Al$ bilayers

We use 4.5 nm $L1_0$ IrAl compound with strong spin-orbit coupling as seeded layer grown on top of [001] orientation MgO substrate, then $Co_{2.3}Al$ layer with different thickness is grown on top. The high resolution cross section TEM image of IrAl / $Co_{2.3}Al$ bilayer is shown in Figure 4.17a with [100] viewing direction along MgO substrate. Both IrAl and $Co_{2.3}Al$ layer grows with 45^o normal to the MgO lattice edge shown in Figure 4.17a. The pattern of selected area electron diffraction proves high degree of crystallinity of $Co_{2.3}$ Al layer. Typical (001) and (002) XRD peak shows that both IrAl and Co2.3Al grows with layer-by-layer mode in Figure 4.17d.

The out-of-plane and in-plane magnetization hysteresis loop for $Co_{2.3}Al$ films with varying thickness is shown in Figure 4.18. Its magnetization state changes from strong perpendicular magnetic anisotropy into spin spiral along *z* axis with thickness varying from 3 to 30 nm shown in Figure 4.18a and b. And saturation magnetization gradually increases from 500 to 650 emu/cc in Figure 4.18c. Furthermore, its effective crystalline anisotropy (K_u) first increases to 0.17 MJ/m^3 then gradually decreases with $Co_{2.3}Al$ thickness increasing. We use the Van-der-Pauw method to measure Hall resistivity (ρ_H) of IrAl / $Co_{2.3}Al$ bilayer structures in Figure 4.18 e and f. The ρ - H loop changes from square to spiral shape with thickness increasing from 5 to 30 nm. ρ_H increases from 1.1 to 1.8 μΩ cm as $Co_{2.3}Al$ film thickness increasing. The temperature dependent longitudinal resistivity of bilayer structure with 30 nm $Co_{2.3}Al$ increases to 440 uΩ cm. The Hall resistivity at 300 K for bilayer structure is 1.66 μΩ cm, which is little higher compare with that in single $Co_{2.3}Al$ film. By extracting ρ_{AHE} and ρ_{OHE} from ρ_H, we obtain the maximum topological Hall resistivity peak with a magnitude of 0.1 μΩ cm, which is similar in single $Co_{2.3}Al$ film. The insertion of IrAl shows no significant effect on their topological Hall feature compare with single $Co_{2.3}Al$ film. The helical magnetic domain stripes and nano spin objects were recorded at room temperature by performing magnetic force microscopy imaging for bilayer structure, which is shown in Figure 4.19 d - h. The red and blue colored regions correspond to the magnetization domain with pointing up and down direction normal to the sample surface. The periodical domain width is ~ 120 nm with frequent magnetic reversal. As field increasing, the helical stripe domain at zero field gradually break into round shaped fragments with field of 1.8 kOe and the size of spin objects is sub-100 nm in Figure 4.19g. And sample is magnetic saturated at 2.5 kOe showing no spin textures.

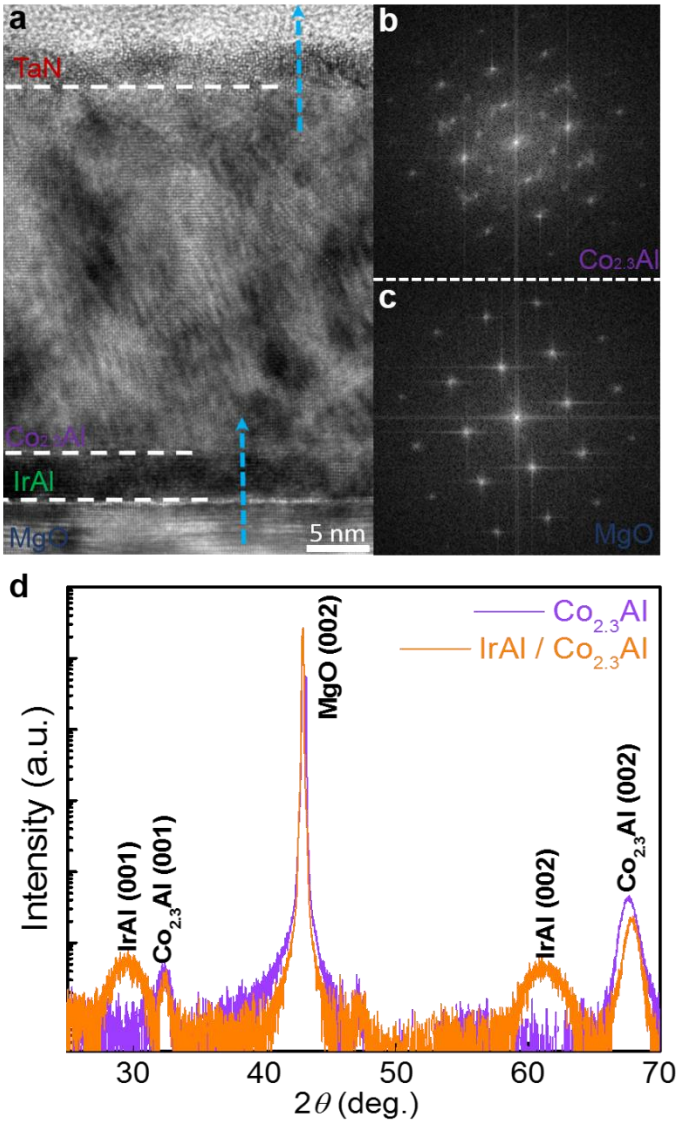

Figure 4.17 (a) High resolution cross section TEM images for IrAl / $Co_{2.3}Al$ bilayer structures with [100] viewing direction along [001] oriented MgO substrate. (b) and (c) Selected area electron diffraction of $Co_{2.3}Al$ layer and MgO substrate. (d) *X*-ray diffraction results of single $Co_{2.3}Al$ films and IrAl / $Co_{2.3}$ Al bilayer sample.

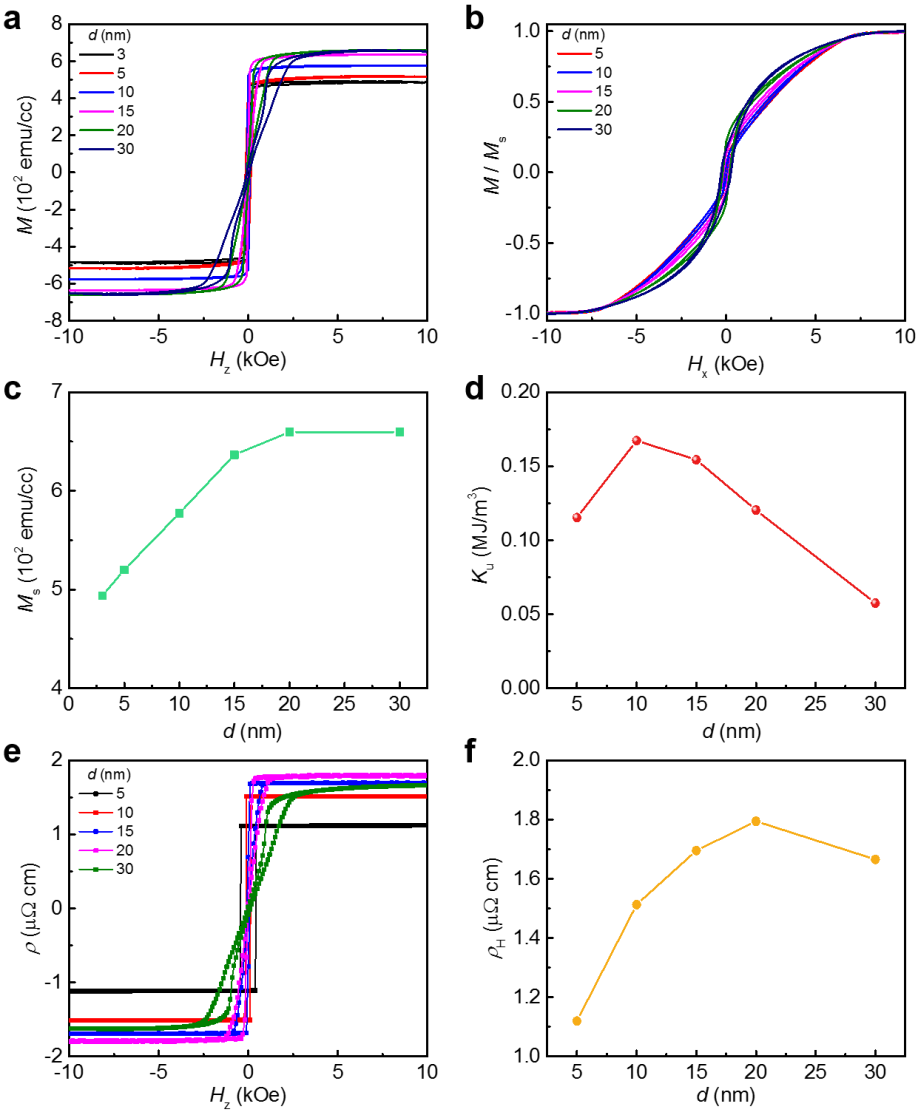

Figure 4.18 Magnetic and electric transport properties of IrAl / *d* $Co_{2.3}Al$ bilayer structures. Room temperature out-of-plane (a) and in-plane (b) *M* (H) loop for $Co_{2.3}Al$ layer with different thickness. (c) Plot of saturation magnetization (M_s) versus thickness of $Co_{2.3}Al$ layers. (d) Plot of effective crystalline anisotropy versus thickness of $Co_{2.3}Al$ layers. (e) Hall resistivity of IrAl / $Co_{2.3}Al$ bilayers with different thickness of $Co_{2.3}Al$ layers. (f) Plot of Hall resistivity versus thickness of $Co_{2.3}Al$ layers.

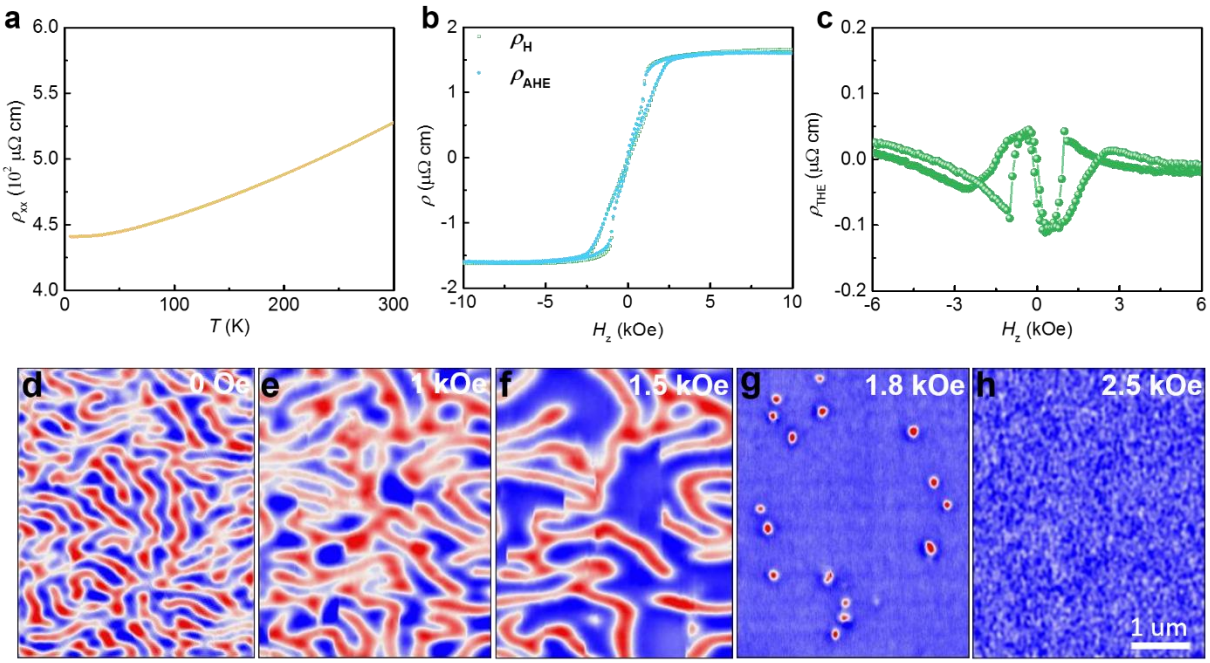

Figure 4.19 (a) Temperature dependent longitudinal resistivity of IrAl / $Co_{2.3}$ Al bilayer thin film measured at zero magnetic field. (b) Comparison between the total Hall resistivity ($\boldsymbol{\rho}_H$) and anomalous Hall resistivity ($\boldsymbol{\rho}_{AHE}$) at 300 K. (c) $\boldsymbol{\rho}_H$ extracted from the difference between $\boldsymbol{\rho}_H$ and $\boldsymbol{\rho}_{AHE}$. (d) MFM image recorded at 300 K and zero magnetic field. (d - h) Evolution of the magnetic spin textures as the magnetic field increased from 1 to 1.8 kOe and finally to the field polarized state at 2.5 kOe. The blue and red colors correspond to up and down domains respectively. All MFM images are at the same scale: a scale bar is given in h.

Conventionally, in Néel type skyrmion their spins radially rotate either pointing in or pointing out, which is shown in Figure 4.20 b. Therefore, the total reflection of electron beam is compensated, leading to zero Lorentz contrast. When the sample tilts with different angle in regard to *z* axis of the lamella. The asymmetric deflection of electrons from the projection of the magnetization contributes to *L*orentz contrast. We performed under focused with 1.5 mm distance Lorentz TEM imaging on IrAl / $Co_{2.3}$Al bilayer structures in Figure 4.20 c - l. When the tiling angle is 0 degree, it shows no contrast in Figure 4.20 d. When the sample is titled along the *y* axis with +30 and -30 degrees, it shows magnetic helical stripe domain in the absence of magnetic field in Figure 4.20 c and e. When the out-of-plane field increased to 1.6 kOe, the bilayer structure still shows zero contrast without tilting angle. However, with sample tilting at +30 and -30 degrees, the helical stripe is broken into numerous round objects with the dimension of sub-100 nm in Figure 4.20 f and h. In order to scrutinize its spin texture, the magnified picture of spin round object is put inset in Figure 4.20h. It shows half bright and half dark contrast depending on the sign of tilting angle. Here our observation is consistent with the discovery of Néel skyrmion rather than biskyrmion or bubbles. The contrast can be found

in these biskyrmions, bubbles or Bloch skyrmions even without sample tilting. Furthermore, it is shown that the size of Néel type skyrmion increases at 100 K compare with that recorded at 300 K. Also the magnetic contrast is opposite between the under-focused (1.5mm) and over-focused (1.5mm) LTEM images in Figure 4.20 n and o, and there is no contrast at in-focus state.

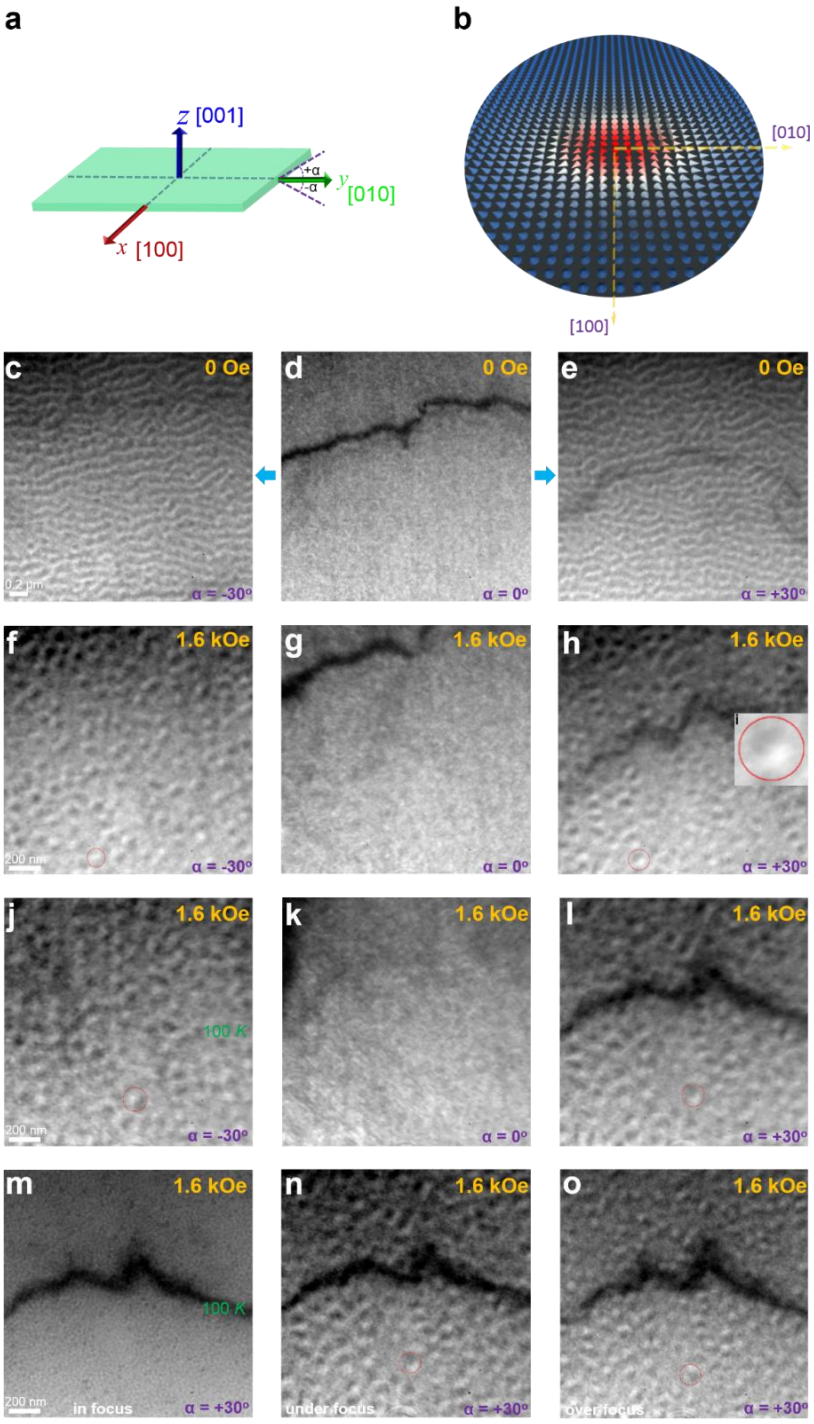

Figure 4.20 Lorentz TEM images of IrAl / $Co_{2.3}Al$ bilayer thin films recorded at room temperature. (a) Schematic representation of sample tilting along the *y* axis defining positive and negative α tilted angles. (b) Spin texture of a Néel skyrmion. (c – i) Room temperature under-focused (1.5 mm) LTEM images of IrAl / $Co_{2.3}Al$ bilayer structure sample recorded with tilting angles from *xy*-plane, (c) -30° at 0 Oe and (f) -30° with 1.6 kOe, (d) 0° Oe and (g) 0° with 1.6 kOe, (**e**) + 30° at 0 Oe and (h) + 30° with 1.6 kOe, the field is applied along *z* axis. **i,** Magnified picture of spin textures with red circle identified in h**.** j, k, and l, under-focused (1.5 mm) LTEM images recorded at 100 K with 1.6 kOe field at different tilting angles. m, n and o The variation of spin texture at different focused state, m, in-focused, n, under-focused, and o, over focused.

4.4 Electric, magnetic properties and domain structures of $Co_2Pt_{0.45}Al$ thin film

We doped platinum into $Co_{2.3}Al$ films to increase the strength of spin-orbit coupling. We grew 35 nm $Co_2Pt_{0.45}Al_1$ thin film by magnetron co-sputtering from three individual targets. The *X*-ray diffraction results with typical (001) and (002) peak can prove the 35 nm $Co_2Pt_{0.45}Al$ are layered centrosymmetric materials with c = 2.764 Å in Figure 4.21a. It is shown that in Figure 4.21b, saturation magnetization of $Co_2Pt_{0.45}Al$ is 660 emu/cc, which is similar for IrAl / $Co_{2.3}Al$ bilayer structure. The Hall resistivity is up to 2.6 μΩ cm larger than that in $Co_{2.3}Al$ film and IrAl / $Co_{2.3}Al$ bilayer structure, which is mainly because of strong spin-orbit coupling induced by platinum. Its longitudinal resistivity increases a lot compare with that in single $Co_{2.3}Al$ film.

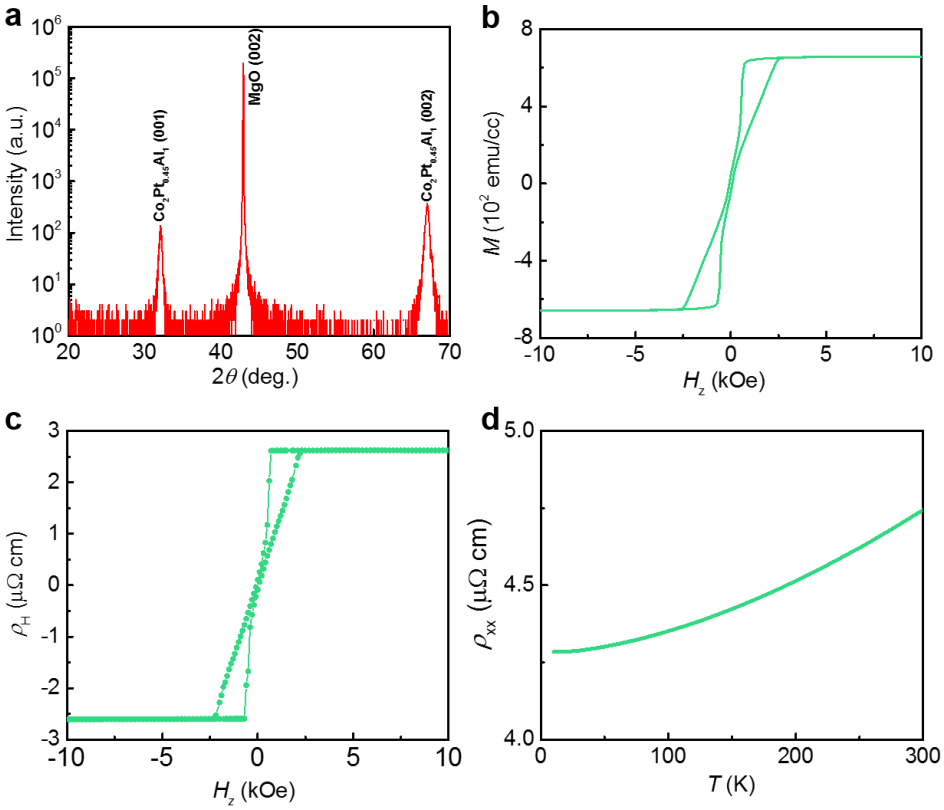

Figure 4.21 Crystal structure, magnetic and electrical properties of 35 nm $Co_2Pt_{0.45}Al$ thin film grown on [001] orientation MgO substrate. (a) *X*-ray diffraction results of single $Co_2Pt_{0.45}Al$ film. (b) Room temperature out-of-plane *M* (H) loop for $Co_2Pt_{0.45}Al$ film. (c and d) Room temperature Hall resistivity and temperature dependent longitudinal resistivity of $Co_2Pt_{0.45}Al$ film.

The plane view lamella of 35 nm $Co_2Pt_{0.45}Al$ thin film for LTEM imaging is prepared by conventional Ar-ion milling from the backside of MgO substrate. The evolution of magnetic

spin textures of $Co_2Pt_{0.45}Al$ thin film as a function of field is shown in Figure 4.22. It is shown that in Figure 4.22a, c and e, the magnetic contrast remains the same upon the tilting angle of the sample. Furthermore, there is helical magnetic domain stripes with dark and bright sharp contrast in the absence of the magnetic field in Figure 4.22a. This proves that the spin objects discovered in $Co_2Pt_{0.45}Al$ is still skyrmion bubble even though increase of spin-orbit coupling in the centrosymmetric materials system. The normalized size of skyrmion is 150 nm. These results suggest that the interfacial spin-orbit coupling in IrAl / Co2.3Al bilayer structures play an important role in stabilizing Néel skyrmion.

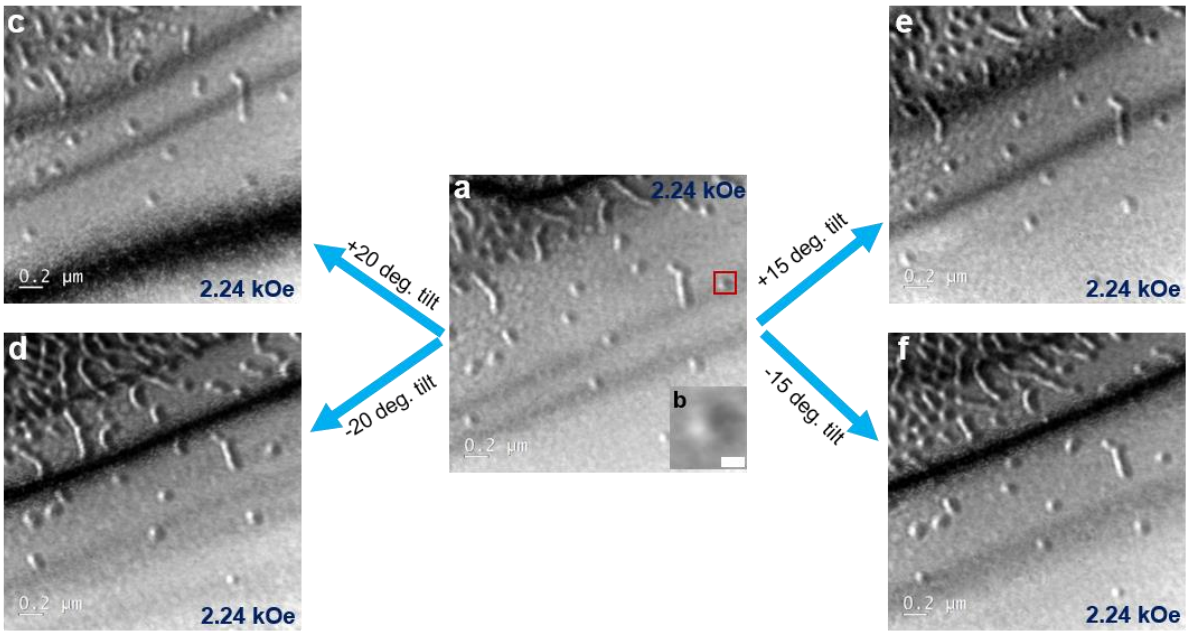

Figure 4.22 Lorentz-TEM images recorded at room temperature for 35 nm $Co_2Pt_{0.45}Al$ thin film. (a) Magnetic spin textures of $Co_2Pt_{0.45}Al$ film recorded with out-of-plane field of 2.24 kOe. (b) The magnified picture of red squared identified spin texture in (a) with half bright and half dark contrast. (c and d) Spin textures of $Co_2Pt_{0.45}Al$ film with positive and negative 20 degrees tilting angle with regard to sample plane. (e and f) Spin textures of $Co_2Pt_{0.45}Al$ film with positive and negative 15 degrees tilting angle with regard to sample plane.

4.5 Summary

We discovered small size skyrmion bubble (~ 100 nm) in Co_xAl thin film with $L1_2$ centrosymmetric crystal structure. The skyrmion bubble transformed into Néel skymion by harnessing the strong spin-orbit coupling and interfacial DMI in between IrAl under layer and $Co_{2.3}Al$. The significant topological Hall resistivity (ρ_{THE} ~ 0.1 μΩ cm) has been found in both $Co_{2.3}Al$ film and IrAl / $Co_{2.3}Al$ bilayer structure. The characteristics of skyrmion bubble of $Co_{2.3}Al$ thin film did not change with platinum doping. The small diameter of Néel skyrmion observed at room temperature in thin films system with large spin Hall angle of IrAl as under layer provides a promising route towards the practical application of skyrmions into racetrack memories.

5. Magnetization switching of tetragonal distorted Mn_xSn (Sb) Heusler alloys by seeded IrAl

5.1 Introduction of current induced magnetization switching

Energy efficiency magnetoresistive random-access memories (MRAMs) requires materials such as strong spin-orbit coupling heavy metals, Weyl semimetals, and topological insulators et al. with large spin-orbit torques and magnets having low magnetic moment values, high thermal stability for lowering the power consumption in the procedure of current writing and reading operation and reducing device size [4,11,14,101-107]. The spin current originates from intrinsic spin Hall effect in strong spin-orbit coupling materials and/or interfacial Rashba-Edelstein effect can exert torques called spin-orbit torques on the adjacent ferro- and ferrimagnetic materials, causing the magnetic state reversal by charge current [101-107]. Two magnetic direction with up and down can be used to represent the status of "0" and "1" respectively as prototype in MRAMs [1,2]. Low magnetic moment ferrimagnets with large perpendicular magnetic anisotropy (PMA) can lower the symmetry and allow injected current writing and reading as digital bits in magnetic logic memory devices more easily [101-107]. It is of great important in technology application with field-free current induced switching in magnetic units, because the integration of external magnetic field sources is harmful for scaling down the size of nanometer devices and thus undesirable.

Heusler compounds represent a large cluster of materials with more than 2000 members, which displays the highly tunable electrical, magnetic, optical, and thermal properties et al [108-111]. Heuslers are kinds of alloys with chemical formula of X_2YZ and X_3Z, wherein X and Y are metal elements in the transition group including rare-earth metals and Z is the element in the main group [109-111]. Ferrimagnetic X_3Z binary Heusler alloys exhibits the features of adjustable magnetic properties in the field of atomic scale ordering of elements such as large perpendicular magnetic anisotropy, high curie temperature, low ratio of saturated magnetization (M_s), fast domain wall motion and application in electrical induced magnetization switching [98,112-116]. The parent phase of conventional Mn_3Z Heuslers are cubic crystal structure, which can't show magnetic anisotropy [108,109,110]. The compounds are found to display PMA and sizable anomalous Hall signal when they are tetragonally distorted [108,109,110].

Damping-like SOTs from charge current flowing through materials with strong spin-orbit interaction, accumulated spin ($\vec{\sigma}$) aligns in the y direction, therefore the SOTs is restricted in

the in-plane direction, which can't tilt or reverse the magnetic moment direction. Furthermore, the symmetry breaking in *y* axis induced by vacancies, crystal lattice distortion from strain as well as heterojunction of atomic steps from bilayer structures can cause $\vec{\sigma}$ ($\pm\vec{\sigma} \parallel \pm\vec{z} = \vec{x} \times \vec{y}$) aligns along *z* axis direction when transport charge current is along *x* direction, therefore out-of-plane SOTs favors one of the two magnetization direction, which cause the reversal of magnetic state [117-120]. Here, we demonstrate that tetragonal distortion Mn_xSn (Sb) ($2 \leq x < 3.1$) Heulser thin films with varying thickness from unit cells scale to large thickness (9 nm) can be prepared by magnetron sputtering on top of new kind of spin Hall effect materials of IrAl with alternating layered structure [121]. Both in-plane and out-of-plane orbitals can split owing to tetragonal distortion, therefore the Van-Hove singularity removes from E_F, and the *DOS* peaks reduces, then it displays anisotropy in magnetic properties [110]. The magnetic states of the two nonequivalent Mn spin sub-lattices can be detected by standard ferromagnetic measurement techniques, such as anomalous Hall effect and magneto-optic methods et al [116, 122, 123]. Initial experimental results shows that the magnetization switching of Mn_3Ge, Mn_3Ga, and $Mn_2Ru_{1-x}Ga$ Heusler layers is by SOTs arising from Pt layer with a large current density and magnetic field for breaking the in-plane symmetry, which are not good choices for the application in nanometer size devices [105,123,124]. The successful heterogeneous epitaxy growth of Mn_xSn (Sb) on top of alternating layered Co-X (X= Al, Sn, Ga, and Ge) compound, which exhibits highly efficient domain wall motion in racetrack memories is reported by IBM group [98]. Therefore, the utilization of these unit cells ferrimagnetic Heusler alloys as information storage elements remains need to be explored. Minimizing the critical switching current density (J_c) at the same time maintaining good thermal stability are major challenges for the application of Heusler alloys in magnetic memory logic devices.

In this chapter, we present the highly efficient spin-orbit torque switching in low magnetic moment Mn_xSn (Sb) ferrimagnetic films with ultralow current density ($J_c \sim 10^6$ A cm^{-2}). Field-free current induced magnetization switching is successful with 10 ms. width direct current pulses. The switching efficiency is heavily dependent on the number of vacancies in Heusler layers, the disordering of interface structure, atomic step heterojunction between IrAl and Mn_xSn (Sb) layers and the intrinsic strength of SOTs. Furthermore, the atomically flat Heusler thin films as well as sharp interface between Heuslers and the above tunneling MgO barrier indicates the high matching degree of lattice parameter from high resolution-scanning transmission electron microscopy (HR-STEM), which shows its promising application as reference layer in magnetic tunnel junction.

5.2 Magnetic properties and Hall effect of IrAl / *t* Mn_xSn (Sb) samples

The thickness of IrAl seeded layer is 53 Å, which is directly grown on top of [001] orientation $MgAl_2O_4$ substrate with 2 nm MgO buffer layer by magnetron sputtering at room temperature. Then the varying thickness and composition of Mn_xSn (Sb) Heusler alloy can be successively epitaxy growth on top with perpendicular magnetic anisotropy, which displays in Figure 5.1a and b. The saturation magnetization of 15 Å $Mn_{3.05}Sn$ thin films is ~ 130 emu/cc and M_s varies slightly with x for Mn_xSn Heusler thin film. Both anomalous Hall resistance (R_H) and coercivity (H_c) gradually increases with *x* varying from 2.15 to 3.05 for Mn_xSn films in Figure 5.1d. R_H gradually shrinks from 0.9 to 0.7 Ω as *x* varies from 3.05 to 2.15 in 15 Å Mn_xSn thin films with a tiny coercivity (H_c ~ 40 Oe). 11 Å Mn_xSb film shows weak perpendicular magnetic anisotropy compare with Mn_xSn alloy thin film in Figure 5.1e. The magnitude of R_H for Mn_xSb is smaller compare with that in Mn_xSn films. Also the spin polarization direction is opposite from the sign of dR_{xy} / dH. The spin polarized electrons whose spins are antiparallel to the magnetization of Mn_xSb film, therefore giving rise to a negative anomalous Hall signal.

5.3 High resolution cross section TEM images of IrAl / Mn_xSn (Sb) bilayer structures

High resolution cross section TEM images of 53 IrAl / 45 $Mn_{2.15}Sn$ bilayer structures is shown in In Figure 5.2a, the viewing direction is [100] orientation along the $MgAl_2O_4$ substrate. The clear atomic step with 5 Å height between IrAl and $Mn_{2.15}Sn$ layers is observed. Furthermore, in Figure 5.2d, line-scan profile of energy-dispersive *X*-ray element analysis suggests that there is intermixing between IrAl and $Mn_{2.15}Sn$ at interface. The inversion symmetry breaking and crystalline disordered in the heterostructure interface may play an important role in current induced magnetization switching of IrAl / $Mn_{2.15}Sn$ bilayer structures. From selected area electron diffraction (SAED) in Figure 5.2b and c, both IrAl and $Mn_{2.15}Sn$ layer displays high degree of crystallinity. From energy-dispersive *X*-ray element mapping analysis in Figure 5.2 e – h, we know that the film is distributed homogeneously.

Furthermore, in order to check the crystal structure of IrAl / Mn_xSb samples, the sample stack that we used to investigate the crystal structure is 53 IrAl / 30 Mn_2Sb. We obtain the high atomic resolution images of the stack by HR-STEM, which is shown in Figure 5.3a. The epitaxy growth relationship between IrAl and [001] oriented $MgAl_2O_4$ substrate is 45°. It is shown in Figure 5.3a both in-plane (a_{IrAl} = 2.18 Å and a_{Mn2Sb} = 4.33 Å) and out-of-plane (c_{IrAl} = 3.08 Å and c_{Mn2Sb} = 6.18 Å) lattice parameter between IrAl and Mn_2Sb are highly matching with mismatching degree less than 1%. Both two layers grow along [001] orientation, the tiny lattice mismatching

between IrAl and Heusler layers suggests small strain in them, also the hetero-interfaces is atomically sharp in between as indicated by HR-STEM [125]. Because of lower *Z* atomic contrast of Sn compare with Sb element, the IrAl / $Mn_{2.15}Sn$ bilayer sample exhibits poor atomic resolution in Figure 5.2a. Furthermore, the MgO tunneling barrier on top of Mn_2Sb films displays the high quality of crystal structure with small lattice mismatching (a_{MgO} = 4.21 Å) compare with Mn_2Sb, which suggests the promising application in full Heusler magnetic tunnel junction structure. The atomic structure schematics of IrAl / Mn_xSn (Sb) bilayer displays its atomic step in Figure 5.3b.

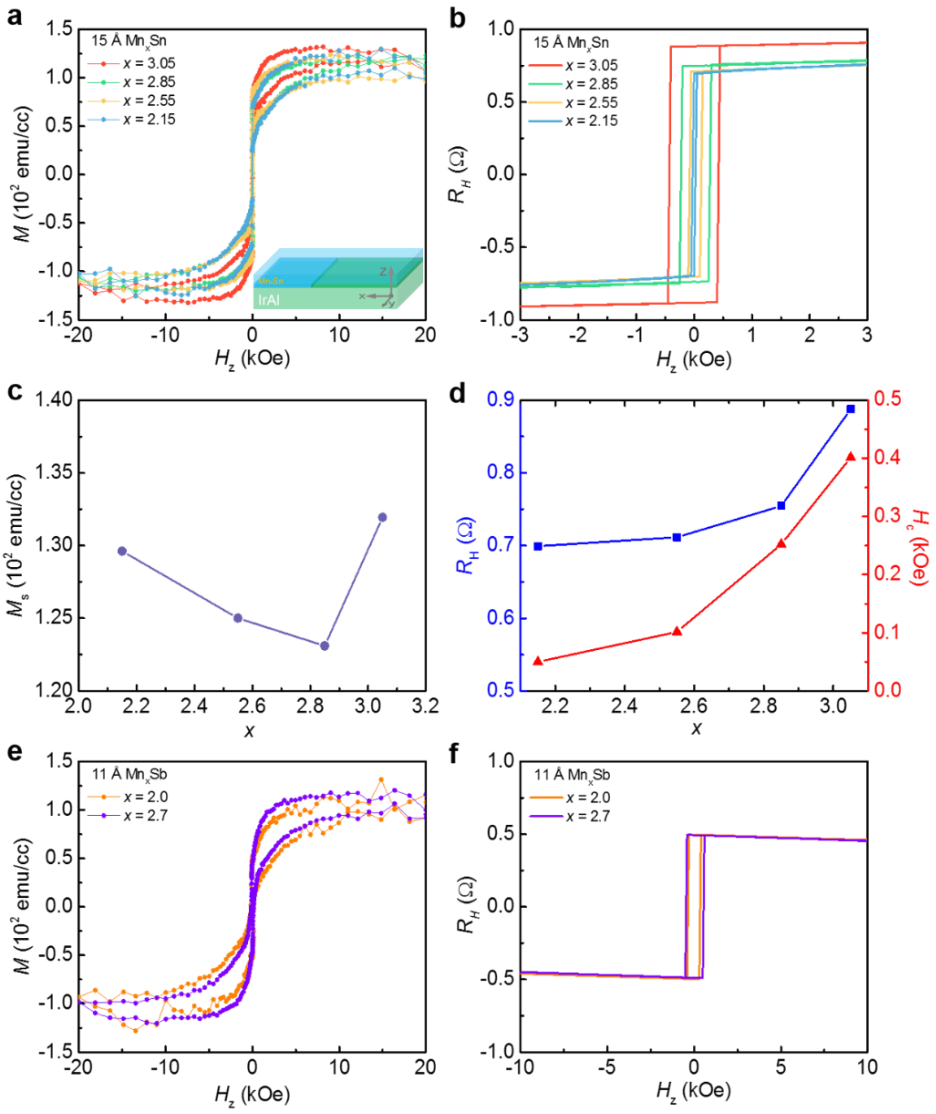

Figure 5.1 Crystal structure, magnetization and electronic properties. (a) Magnetization *M* and (b) anomalous Hall resistance R_H of 53 IrAl / 15 Mn_xSn bilayer samples (all numbers in layers are Å) as a function of out-of-plane magnetic field. (c) Plot of saturation magnetization versus *x* for 53 IrAl / 15 Mn_xSn bilayer samples. (d) Plot of anomalous Hall resistance (R_H) and coercivity (H_c) versus *x* for 53 IrAl / 15 Mn_xSn bilayer samples. (e) Magnetization *M* and (f) anomalous Hall resistance R_H of 53 IrAl / 11 Mn_xSb bilayer samples as a function of out-of-plane magnetic field.

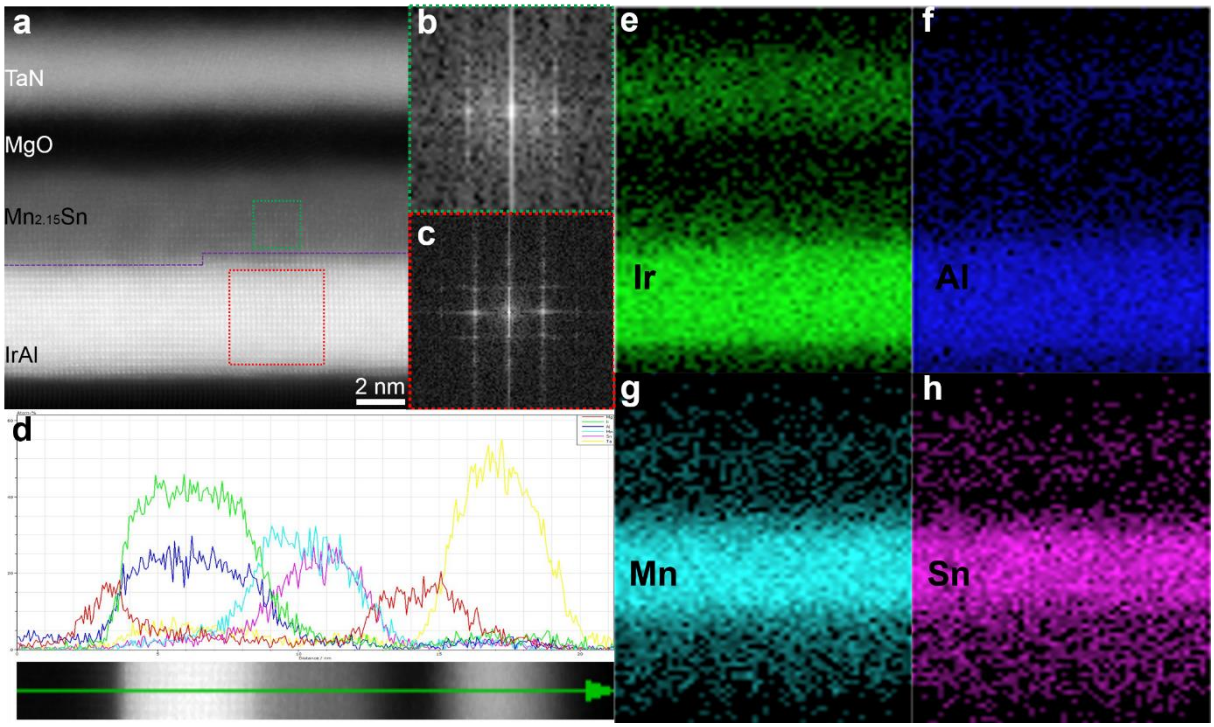

Figure 5.2 (a) High resolution cross section TEM images of 53 IrAl / 45 $Mn_{2.15}Sn$ bilayer structure with [010] viewing direction. (b and c) Selected area electron diffraction of $Mn_{2.15}Sn$ and IrAl layers, respectively. (e – h) Energy dispersive *X-ray* mapping of 53 IrAl / 45 $Mn_{2.15}Sn$ bilayers, all samples is capped with 2 nm MgO and 5 nm TaN insulating protective layer.

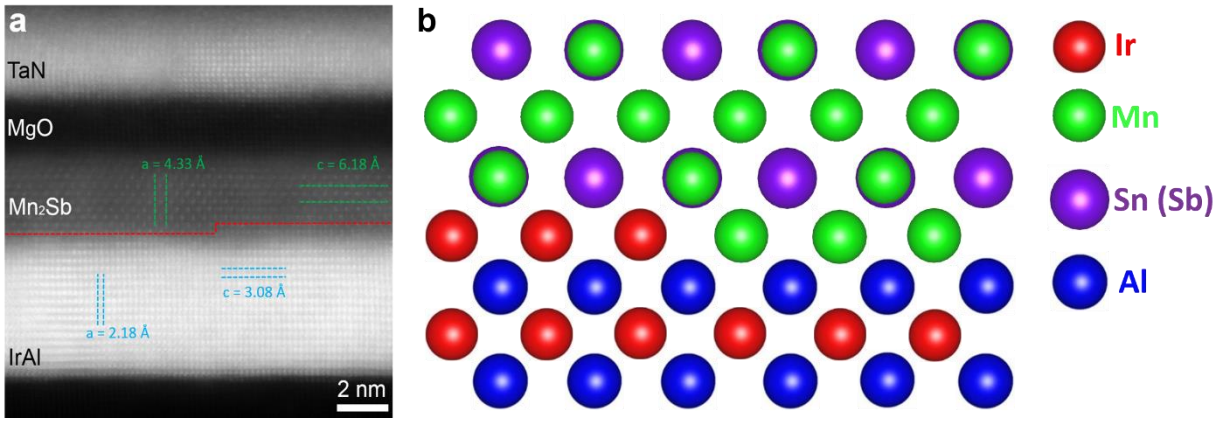

Figure 5.3 (a) High-angle annular dark field cross section TEM images for 53 IrAl / 30 Mn_2Sb bilayer structure. (b) Schematics of IrAl / Mn_xSn (Sb) bilayer crystal structure represent with atomic ball.

5.4 Current induced magnetization switching in IrAl / Mn_xSn (Sb) bilayer samples

In order to achieve current induced magnetization switching, we applied the magnetic field along the d.c current direction to assist its magnetization state reversal by field. The input current is 1 mA, the field that used to reverse the magnetization state for IrAl / Mn_xSn increases

as x increasing in Figure 5.4a. The results suggest that large number of Mn vacancies is beneficial to reduce the switching field. However, the switching field changes slightly for IrAl / Mn_xSn bilayer structures in Figure 5.4b, which is mainly related with atomic number of Sn and Sb element.

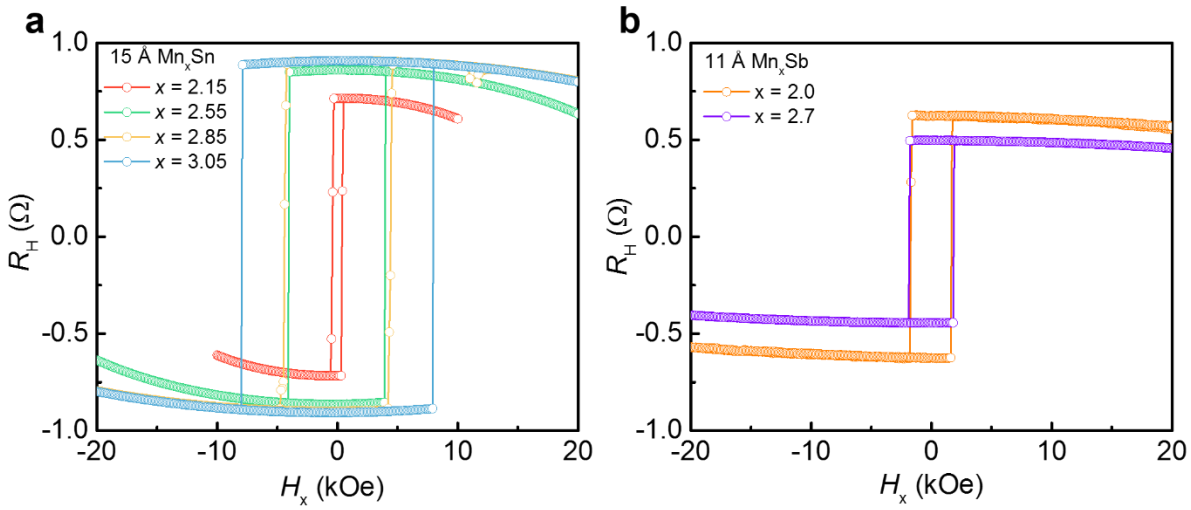

Figure 5.4 (a) and (b) Hall resistance for IrAl / Mn_xSn (Sb) as a function of in-plane magnetic field.

In order to electrically switch the magnetization of the unit cells Mn_xSn Heusler thin films, we successively injected D.C pulses with 10 ms. duration into Hall bar devices, in the meantime, 1 mA current is used for sensing the variation of R_H to detect the change of its magnetization state. Magnetization of 15 Å Mn_xSn films can be switch with up and down direction in the absence of magnetic field. However, the magnitude of R_H in current induced switching figures in Figure 5.5a is smaller compare with $R_H - H$ loop measured from magnetic field sweeping in Figure 5.1a. This result suggests that its magnetization is partially switching rather than completely. Field-free magnetization switching is mostly derived from the large spin-orbit torques including H_z^{FL}, H_y^{FL} and H_y^{DL}, which arises from the inversion symmetry breaking at atomic step heterojunction shown in Figure 5.2 and Figure 5.3. We define J_c as the value of J_x at which R_H crosses zero. The switching current density is the current flowing through both IrAl and Heusler layers and MgO and TaN insulating protective layer. It is shown in Figure 5.6b, the switching current density gradually decreases from 12 to 3 (10^6 A cm^{-2}) with x varying from 3.05 to 2.15. The result suggests that Mn vacancies in Mn_xSn thin film can make a contribution to the decrease of J_c. Both J_c and H_c decrease as x shrinks from 3.05 to 2.15 in Figure 5.5b. The switching polarity is reversed when we change the applied field from $+H_x$ to $-H_x$ shown in

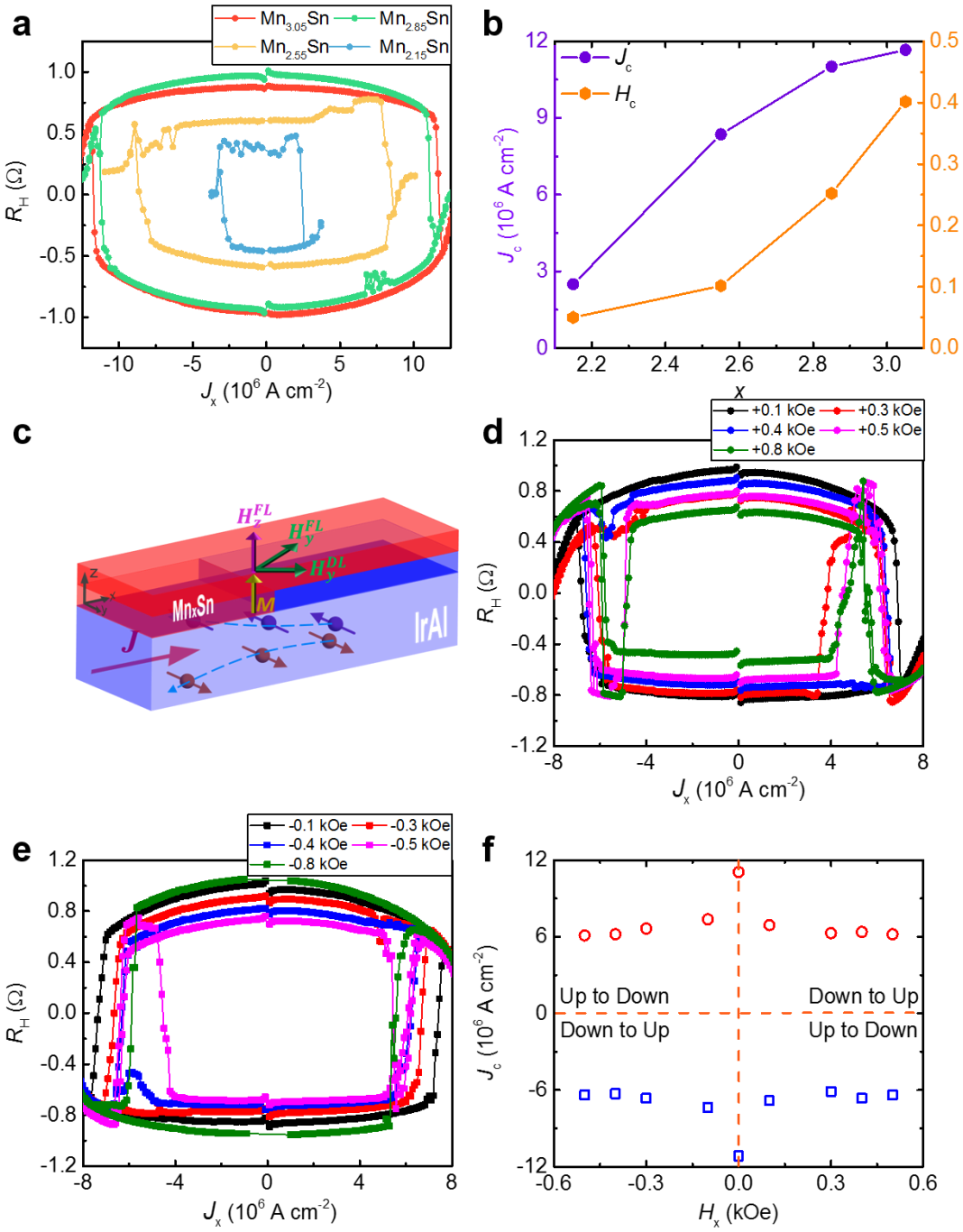

Figure 5.5 Magnetization switching in IrAl / Mn_xSn bilayer structures. (a) Current induced magnetization switching in 53 IrAl / 15 Mn_xSn bilayers at zero field. (b) Field-free critical switching current density and coercivity as a function of *x* in 53 IrAl / 15 Mn_xSn bilayer samples. (c) Schematics of current induced magnetization switching of IrAl / Mn_xSn bilayer structures by spin-orbit torques. (d and e) Current induced magnetization switching in 53 IrAl /15 Mn2.85Sn under different positive and negative magnetic field. (f) Threshold current density as a function of applied in-plane magnetic field in 53 IrAl / 15 $Mn_{2.85}Sn$ sample.

We measured the anomalous Hall resistance of 15 Å $Mn_{2.15}Sn$ films under different temperature. Both R_H and coercivity (H_c) gradually increases as temperature decreasing shown in

Figure 5.6a and b. Then we increase the thickness of $Mn_{2.15}Sn$ layer from 15 to 45 Å. Both R_H and H_c increases with thickness increasing, which is mainly because of increased defects with thin film thickness increasing. At the same time, we also measured the field switching of magnetization for $Mn_{2.15}Sn$ layer with different thickness in Figure 5.6e. The switching field (H_{sw}) increases dramatically from 500 to 3600 Oe with thickness varying from 15 to 30 Å. These results prove that the magnetization of thinner film can be switch easily with low energy.

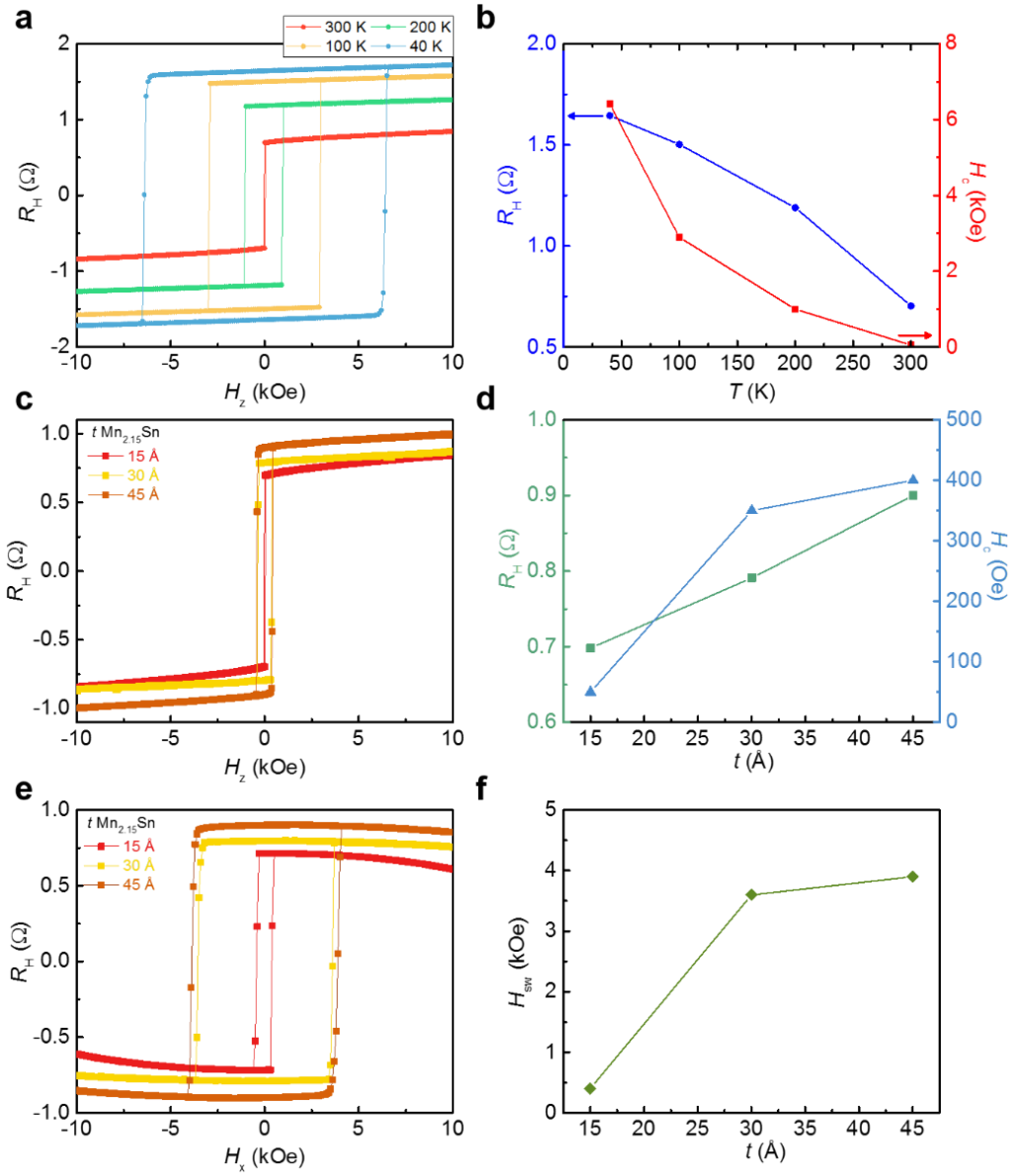

Figure 5.6 (a) Plot of anomalous Hall resistance (R_H) versus out-of-plane magnetic field (H_z) measured at different temperature for IrAl / $Mn_{2.15}Sn$ films. (b) Plot of R_H and H_c versus temperature. (c) Plot of anomalous Hall resistance (R_H) versus out-of-plane magnetic field (H_z) for $Mn_{2.15}Sn$ films with different thickness. (d) Plot of R_H and H_c versus thickness of $Mn_{2.15}Sn$ films. (e) Hall resistance for $Mn_{2.15}Sn$ films with different thickness measured with field along the current direction. (f) Plot of switching field (H_{sw}) versus thickness of $Mn_{2.15}Sn$ films.

It is shown in Figure 5.7a, magnetization of 11 Å Mn_2Sb film is switched with a critical current density (J_c) of 8×10^6 A cm^{-2} which is larger compared with that in magnetization switching of $Mn_{2.15}Sn$. The anomalous Hall resistance (R_H) for Mn_2Sb film with different thickness is shown in Figure 5.7b. Both the magnitude of R_H and coercivity (H_c) gradually increases as film thickness increasing. In the meantime, we also measured magnetization switching of Mn_2Sb thin film with different thickness by field in Figure 5.7c. The switching field (H_{sw}) increases dramatically from 1.4 to 15.8 kOe with thickness varying from 11 to 22.5 Å then decreases when the thickness is 30 Å. These results prove that magnetization of thinner film can be switched easily with low energy and increased defects with thin film thickness increasing.

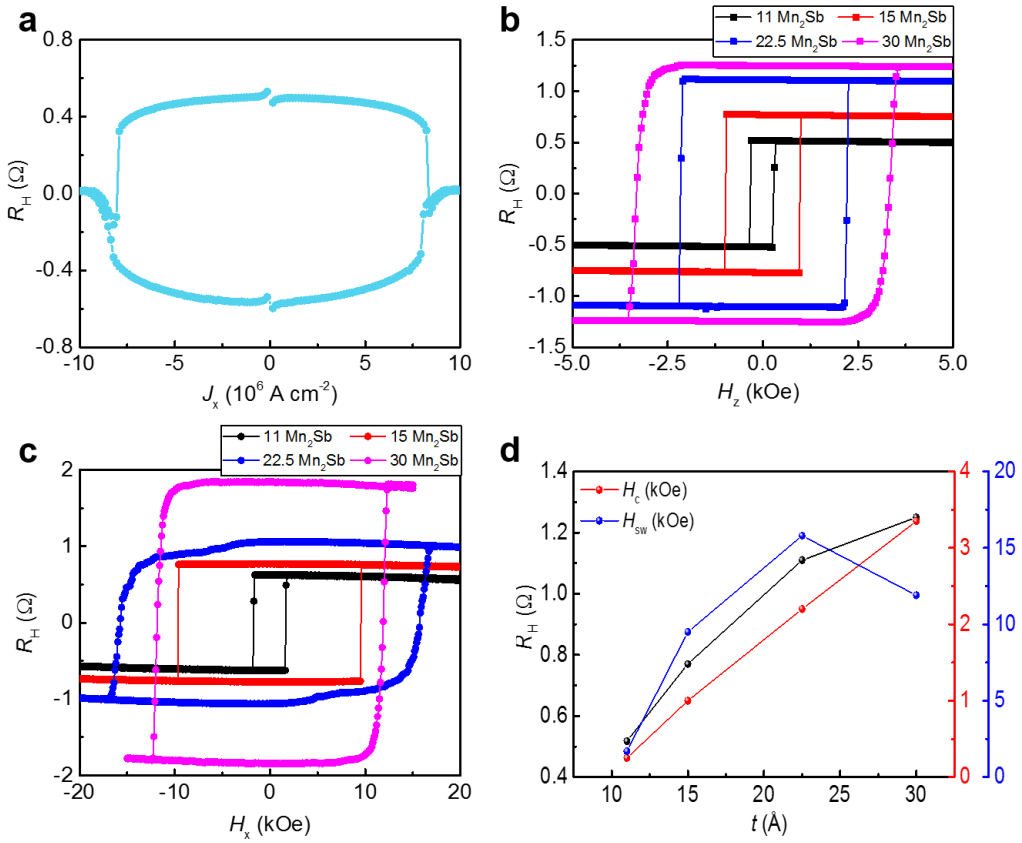

Figure 5.7 (a) Magnetization switching of 11 Å Mn_2Sb film by d.c current pulses. (b) Plot of anomalous Hall resistance (R_H) versus out-of-plane magnetic field (H_z) measured for Mn_2Sb films with different thickness. (c) Hall resistance for $Mn_{2.15}Sn$ films with different thickness measured with field along the current direction. (d) Plot of R_H , H_c and H_{sw} versus thickness of $Mn_{2.15}Sn$ films.

We measured the *X*-ray diffraction results of *d* IrAl / 15 $Mn_{2.15}Sn$ bilayer structure with varying thickness of seeded IrAl layer. The typical (001) and (002) XRD peak is shown in Figure 5.8a. The anomalous Hall resistance of *d* IrAl / 15 $Mn_{2.15}Sn$ bilayer structure with out-of-plane and in-plane field sweeping direction is shown in Figure 5.8b and c. Both magnitude of R_H and H_c

gradually decreases with seeded IrAl layer thickness increasing. The reason why R_H decreasing is because current redistribution in IrAl and $Mn_{2.15}Sn$ layers with varying resistance of IrAl layers with different thickness. The decrease of H_c suggests less defects in $Mn_{2.15}Sn$ layer by high degree of crystallinity from IrAl layer.

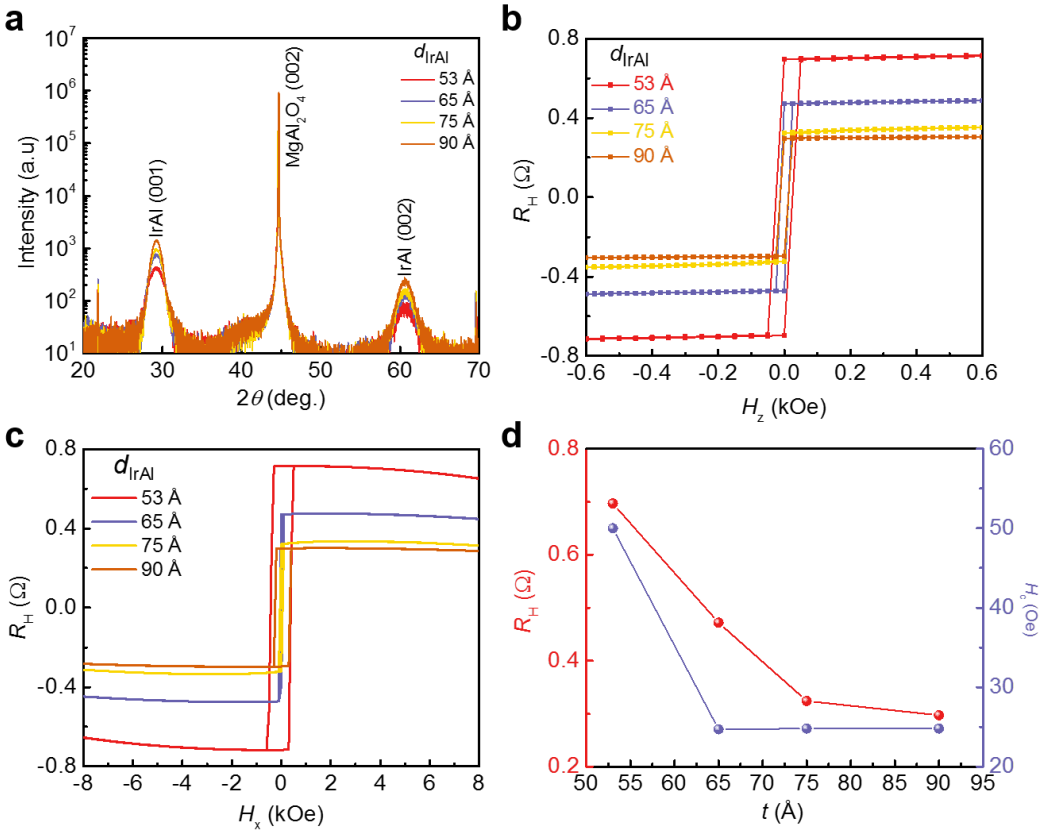

Figure 5.8 (a) *X*-ray diffraction results of *d* IrAl / 15 $Mn_{2.15}Sn$ bilayer structure. (b) Plot of anomalous Hall resistance (R_H) versus out-of-plane magnetic field (H_z) for $Mn_{2.15}Sn$ films with different thickness of seeded IrAl layer. (c) Hall resistance for $Mn_{2.15}Sn$ films with different thickness of seeded IrAl layer measured with field along the current direction. (d) Plot of R_H and H_c versus thickness of seeded IrAl layer.

5.5 Current induced switching and SOT efficiency in IrAl / Mn_xSn bilayer structures

$I_{D.C}$ is input along the *x* direction in Hall bar devices, the sample rotates in the *xy* plane with an angle (θ) from the field (H) direction, θ changes from 0 to 360°. It is shown in Figure 5.9a, the sign of R_H reverses at $\theta \sim 90°$, the maximum torque ($\vec{\tau} = \vec{E} \times \vec{B}$) reverses the magnetic moment direction. Furthermore, magnetic moment is tilted from the equilibrium position by large field (H ~10 kOe), which is because the stable magnetic state is broken, thus the magnitude of R_H becomes smaller compare with that of in small field. It is shown in Figure 5.5a, the

magnetization of $Mn_{2.15}Sn$ films can be switched easily with a low current density ($J_c \sim 3 \times 10^6$ A cm^{-2}) at zero field. Therefore, we applied positive and negative field ($H_x \sim 0.1$ kOe) along current direction, respectively, then we measure the change of R_H in Figure 5.9b. The switching polarity changed by reversing the magnetic field. We found ultralow critical current density ($J_c \sim 10^6$ A cm^2) for the magnetization switching of $Mn_{2.15}Sn$ films under a small field of 100 Oe, which could be derived from inversion symmetry breaking at heterostructure interface as well as large spin-orbit torques induced by IrAl layer [126]. We utilize the harmonic Hall measurement to quantify the magnitude of damping-like and field-like SOTs. Figure 5.9 c shows the first (V_ω) and second ($V_{2\omega}$) harmonic Hall voltages measured from 53 IrAl / 15 $Mn_{2.15}Sn$ bilayer samples. The field is swept along and transverse alternating current (I_0 = 0.5 mA) direction with a frequency of 137 Hz.

The second harmonic Hall voltage $V_{2\omega}$ arises from the magnetization oscillations which is induced by the effective fields from SOTs with applied alternating current $I = I_0 \sin(\omega t)$ [126,127], where ω is angular frequency and t is the oscillation periodic time. By this technique, we can obtain the effective magnetic fields induced by damping-like (H_{DL}) and field-like (H_{FL}) SOTs based on the equation [126, 127]:

$$H_{DL(FL)} = -2 \frac{dV_{2\omega}/dH_{x(y)}}{d^2V_{1\omega}/dH_{x(y)}^2} \quad (1)$$

when the field is swept along the current direction, we can extract H_{DL}. H_{FL} is derived from field sweeping perpendicular to the current direction. We can quantify the SOT efficiency (ξ) including damping-like (ξ_{DL}) and field-like (ξ_{FL}) by:

$$\xi_{DL(FL)} = \frac{2eM_s t}{\hbar} \frac{H_{DL(FL)}}{J_e} \quad (2)$$

where $\hbar$ is Planck's constant, e is the charge of electron, t is the magnetic film thickness, J_e is the current density flowing through the Hall bar device. We have quantified the ratio of ξ_{DL} and ξ_{FL} in 53 IrAl / 15 Mn_xSn bilayer structures. It is shown in Figure 5.9e, both ξ_{DL} and ξ_{FL} increases with x increasing then dramatically dropped, which could be derived from interface transparency as well as electrical potential or Fermi surface mismatching [128, 129, 130]. This also suggests that more Mn vacancies in Mn_xSn films is helpful to obtain large H_{DL} and H_{FL} because of symmetry breaking from nonequivalent Mn moments. The magnetic oscillation is easily induced owing to the large number of vacancies from instable Mn moments in $Mn_{2.15}Sn$ films. The out-of-plane significant field-like torque is crucial for field-free switching of $Mn_{2.15}Sn$ thin films, the origin of this torque could mainly arise from the interface disordering

and/or atomic step in hetero-interfaces (See Figure 5.2 and Figure 5.3) between IrAl / Mn_xSn bilayer structures. Moreover, interfacial strong spin-orbit coupling determined by the termination layer of IrAl could induce the magnetic moment canting at interface. Therefore, its magnetization reversal happens more easily with low J_c. The large SOTs, high quality crystal structure as well as the nontrivial physical phenomenon in hetero-interfaces all play vital roles in their excellent performance of current induced magnetization switching.

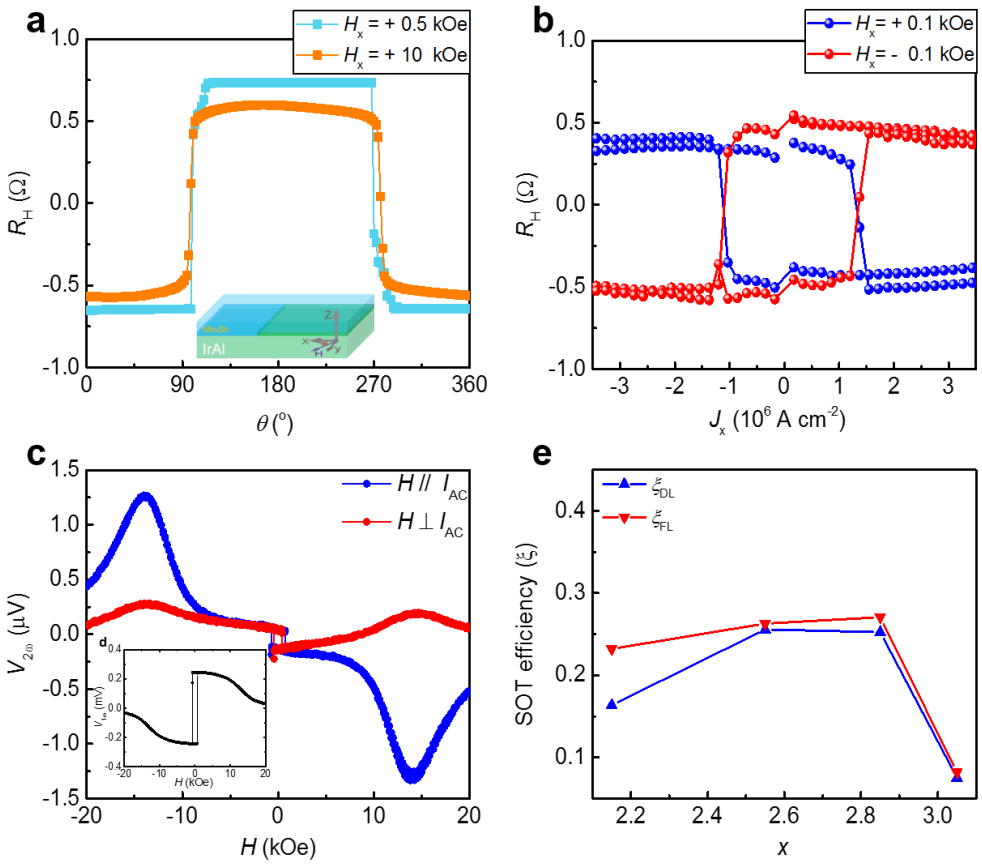

Figure 5.9 Electronic transport measurements in 53 IrAl / 15 $Mn_{2.15}Sn$ bilayer structure. (a) Angle (θ) dependent anomalous Hall resistance R_{xy}, the rotation was performed along *x*-*y* plane for *I* along *x* direction in 53 IrAl / 15 $Mn_{2.15}Sn$ bilayer sample. (b) Current induced magnetization switching with applied positive and negative in-plane field along *x* direction in 53 IrAl / 15 $Mn_{2.15}Sn$ bilayer sample, respectively. (c) 1st ($V_{1\omega}$) and 2nd ($V_{2\omega}$) harmonic Hall voltages measured in 53 IrAl / 15 $Mn_{2.15}Sn$ bilayer structure with an alternating current of 0.5 mA. (d) Spin-orbit torque efficiency (ξ) including damping-like (ξ_{DL}) and field-like (ξ_{FL}) in 53 IrAl / 15 Mn_xSn samples as a function of *x*.

5.5.1 Magnetic and electrical properties of 90 Å $Mn_{2.15}Sn$ layer

We grew thickness dependent $Mn_{2.15}Sn$ Heusler layers on top of IrAl seeded under layers which displays in Figure 5.6. The saturation magnetization of 90 Å $Mn_{2.15}Sn$ thin film is ~ 30 emu/cc with PMA. We measured its Hall resistance R_H with different input current density J_x varying from 1.4 to 8.12 (10^6 A cm^{-2}) into Hall bars. R_H gradually decreases as J_x increasing. When J_x

is larger than 6.58 (10^6 A cm^{-2}), the anomalous Hall effect vanishes. The Joule heating effect from large J_x could break its magnetization state. We perform the current induced magnetization switching experiments to make sure the characteristic length of the spin-orbit torques. The magnetization can be fully switched with large in-plane magnetic field (H_x ~2 kOe) in in Figure 5.10c. The critical switching current density varies from 6.5 ~ 7 (10^6 A cm^{-2}) depending on the field. The switching part of magnetization gradually decreases with field decreasing, which is suggested by the decrease of R_H. These results indicate that thermal effect from Joule heating is not the dominant mechanism in the magnetization switching. The spin-orbit torques can switch the magnetization with a long current pulses (1 ms). Then we shorten current pulse length from millisecond to nanosecond rang, which displays in Figure 5.10d. The switching part of magnetization gradually become less suggests by the shrink of R_H with decreasing current pulse width in Figure 5.10d. The switching polarity reversed when t_p is lower than 100 ns. From these results, we think the incubation time for magnetization switching by spin-orbit torques is larger than 100 ns. Furthermore, the switching polarity reverses is from the magnetic moment disordering at interface and Mn vacancies. The spin-orbit torques, incubation time and joule heating effect all make contributions to the switching of unit cells and large thickness of $Mn_{2.15}Sn$ Heusler thin film.

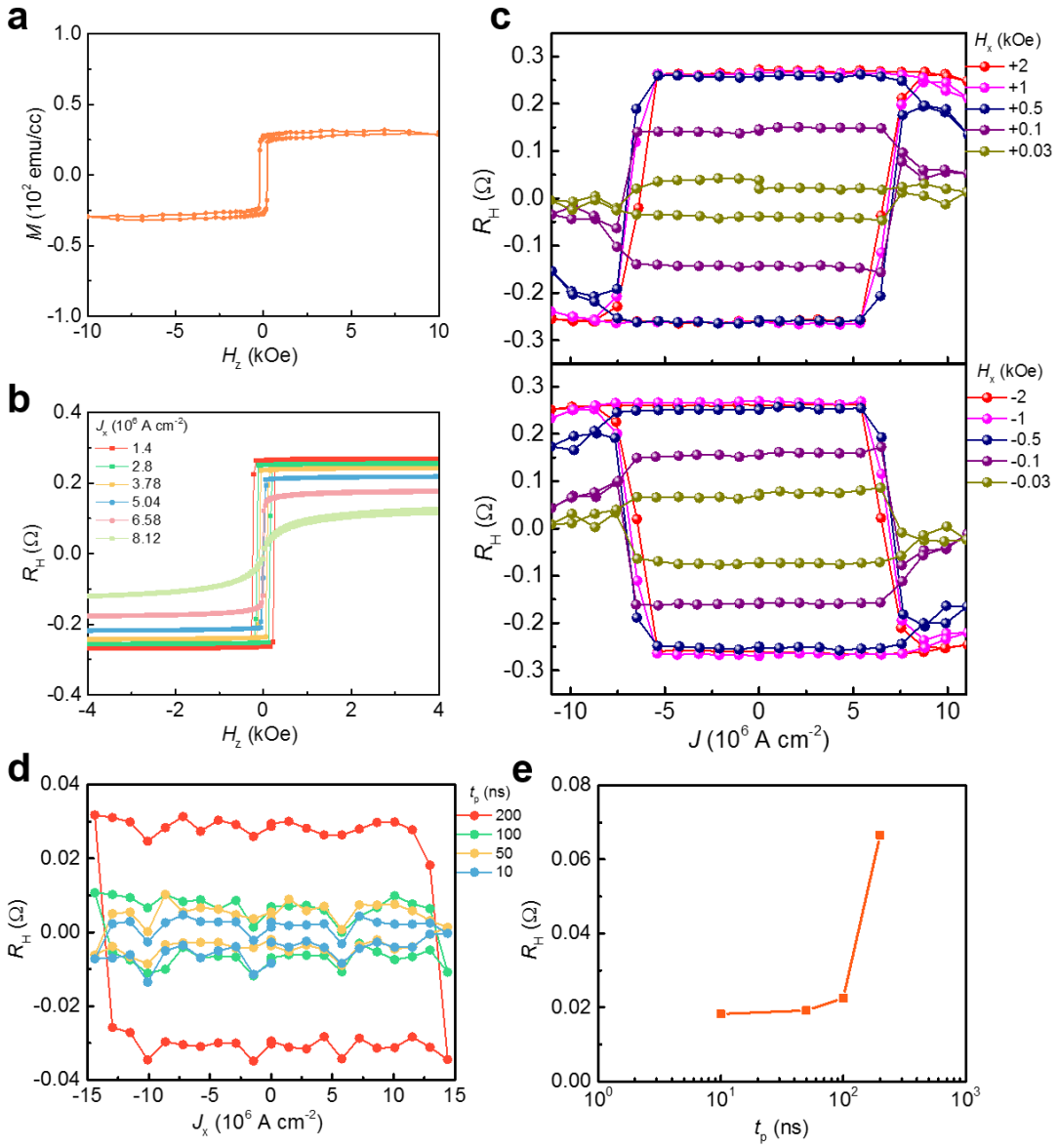

Figure 5.10 Magnetic and electronic transport measurements in 53 IrAl / 90 $Mn_{2.15}Sn$ bilayer structure. (a) Out-of-plane magnetization hysteresis loop of 53 IrAl / 90 $Mn_{2.15}Sn$ bilayer samples. (b) Anomalous Hall resistance of 53 IrAl / 90 $Mn_{2.15}Sn$ bilayers with different input current density. (c) Millisecond current pulse width induced magnetization switching in 53 IrAl / 90 $Mn_{2.15}Sn$ bilayer structures with varying applied in-plane field. (d) Nanosecond current pulse width induced magnetization switching in 53 IrAl / 90 $Mn_{2.15}Sn$ bilayer structures with 2 kOe in-plane magnetic field. (e) Plot of anomalous Hall resistance (R_H) versus current pulse width (t_p) in the range of nanosecond.

5.6 XMCD analysis of IrAl / $Mn_{3.05}Sn$ bilayer structure

Figure 5.11 reveals the key magnetic properties of $Mn_{3.05}Sn$ layers grown on top of IrAl under layer by X-ray magnetic circular dichroism (XMCD) measurements. Figure 5.11a shows the XMCD and X-ray absorption spectra measured with magnetic field under a normal incidence angle (B // c-axis)). Weak XMCD signal at the Mn $L_{2,3}$ edge (5% at L_2 at saturation field of 6T)

is the indication of low magnetic moments of the Mn atomic sites. Field dependent magnetization hysteresis loops measured in normal (Figure 5.11 a and b) and grazing (Figure 5.11 c and d) incidence shows that $Mn_{3.05}Sn$ films have a weak but detectable magnetic anisotropy favoring the out-of-plane easy axis, which is consistent with *M-H* loop measured by SQUID-VSM. We extracted the total magnetic moment of 0.26 μB/Mn including a spin moment of 0.176 μB/Mn and an orbital moment of 0.01 μB/Mn by sum-rule analysis in normal incidence geometry (field perpendicular to the sample). and a similar magnitude of these moment observed in grazing incidence geometry (Figure 5.11 e), meaning that a field of 6T is close to saturate the magnetization in the $Mn_{3.05}Sn$ system . The larger magnitude of spin moment mostly arises from their tetragonal crystal structure, being the orbital moment comparably small. From our atomistic magnetic moment investigations, we confirm that the orbital moment small but finite, featuring a weak anisotropy. The quantitatively determination of Mn moment is strong evidence to support our switching experiments: a weak moment (compensated ferrimagnet) usually requires less energy to switch. Their tetragonal distortion in crystal structure contribute to their ferrimagnetic properties and low power consumption for magnetization switching.

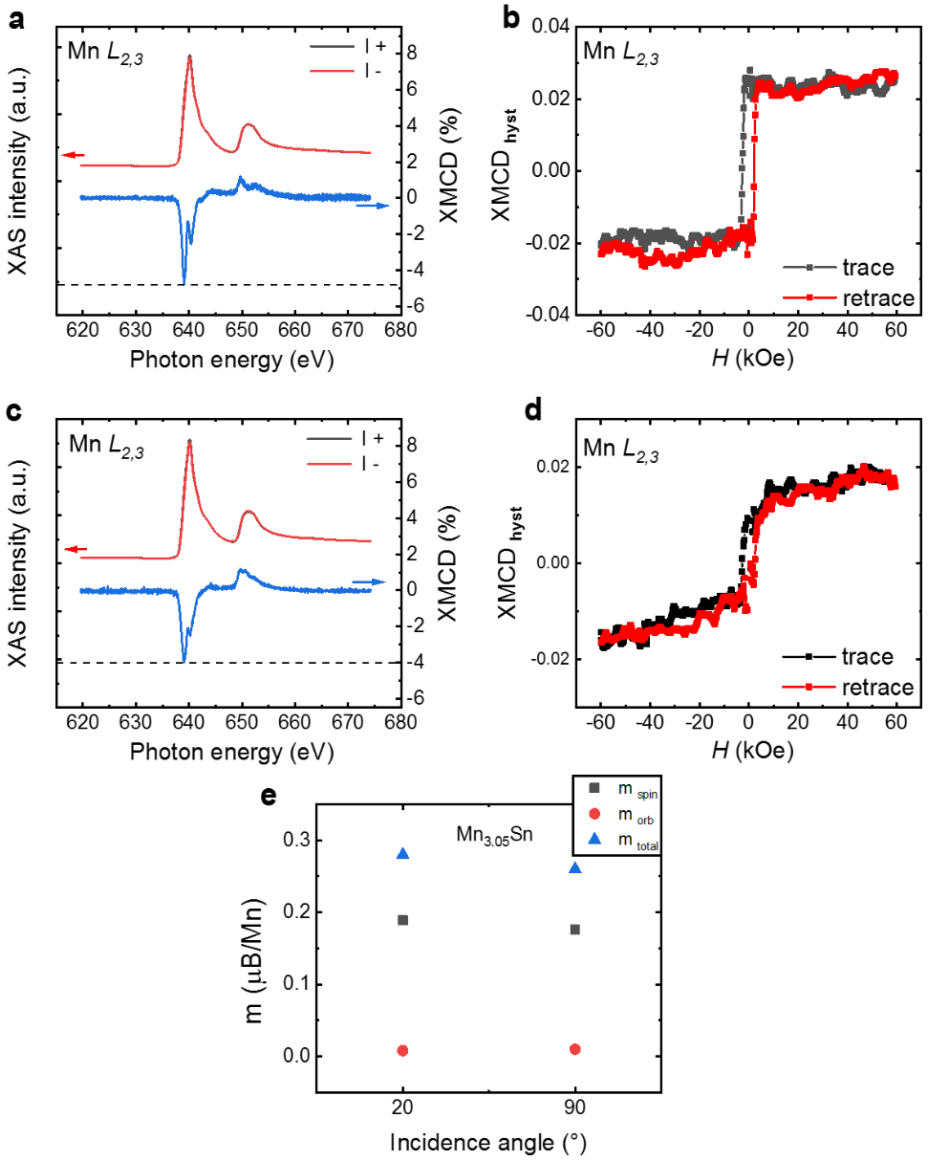

Figure 5.11 Element-specific magnetic properties of IrAl / $Mn_{3.05}Sn$ bilayers by X-ray magnetic dichroism. (a and c) X-ray absorption spectra with different photon helicities and the resulting difference (XMCD), for the Mn $L_{2,3}$ edge at B = 6 T with out-of-plane magnetic field a, and in-plane magnetic field c. (b and d) XMCD hysteresis loops taken in normal (NI) and grazing (GI) incidence, corresponding to the out-of-plane and in-plane component of the magnetization, respectively. (e) The quantification of magnetic moment of Mn by sum-rule analysis including total moment values, spin and orbital moment for $Mn_{3.05}Sn$ thin films.

5.7 Summary

The excellent performance in current writing and reading operation highlight the promising application of Heusler alloys and their compatibilities with complementary metal–oxide–semiconductor (CMOS) technology. Further work is still needed to explore the Heulser alloys down to monolayer limit, other than the heavy metals like Pt, Ta, W, Weyl semimetals and topological insulators et al., IrAl showing large spin-orbit torque efficiency also can be used as SOT generators, which is used in MRAMs. The Mn vacancies in Heusler thin films and atomic step heterojunction play vital role in scaling down the magnetization switching current density and field-free switching, which has large influence on both damping-like and field-like SOTs. The large family of Heusler alloys including binary and ternary compound with known crystal structure, electronic and magnetic properties allow more space for us to solid our understanding in their electrical current writing and reading control. Our work shows that ferrimagnetic Heulsers and new spin Hall effect materials IrAl can both simultaneously improve the energy efficiency of a system, which is compared with other ferro-or ferrimagnetic based SOTs systems.

6. Summary and Outlook

In this thesis, we developed a series of 5*d* transition metal – aluminum alloy thin films by magnetron sputtering. We found the giant spin Hall effect and spin-orbit torque sources from M_xAl_{100-x} alloy system, which displays significant advantage compare with platinum, tantalum, tungsten, topological insulators and non-collinear antiferromagnet et al. The resistivity of M_xAl_{100-x} alloy thin films shows giant magnitude in the range of 20 ~ 40 atom % depending on M. The maximum resistivity, spin Hall angle and spin Hall conductivity shows strong correlation ship with the number of electron in 5*d* band for M_xAl_{100-x} alloys. The critical current density (J_c ~ 7 MA/cm^2) is minimized and motion speed (v ~ 1 km/s) of domain walls maximized by constructing [001] orientation synthetic antiferromagnets using Co, Ni, $Co_{90}Fe_{10}$ with $L1_0$ RuAl as space layer formed on top of Ir_xAl_{100-x}. The interplay of spin Hall conductivity, interfacial DMI, and crystal growth orientation has lowered the power consumption of racetrack memories with several folds compare with previous reports. The full IrAl based magnetic tunnel junction with Co / Ni / Co/ RuAl / $Co_{90}Fe_{10}$ as bottom free layer, MgO as tunnel barrier and $Co_{20}Fe_{60}B_{20}$ as pinned layer displays giant TMR (83.5 %) at room temperature. The successful growth of IrAl on Si wafer proves its compatible capability with CMOS technology by using these thin film stacks.

We discovered skyrmion bubble and Néel skyrmion in Co_xAl thin films and IrAl / $Co_{2.3}Al$ bilayer structure separately proved by MFM and LTEM. A significant topological Hall signal is found in both two sample structures. The strong spin-orbit coupling from IrAl under layer and interfacial DMI in between IrAl and $Co_{2.3}Al$ thin film play important roles in Néel skyrmion formation. The itinerant electron-mediated long-ranged interaction, long-ranged dipole-dipole interaction and DMI are three key factors to determine the spin textures of Co_xYAl intemetallic compound.

The magnetization state of ferrimagnetic Mn_xSn (Sb) Heusler thin film with perpendicular magnetic anisotropy is switch up and down by spin-orbit torques from seeded IrAl under layer. Zero field magnetization switching happened in IrAl / Mn_xSn bilayer structures because of the inversion symmetry breaking at interfaces from atomic step hetero-junction in between IrAl and Mn_xSn layers. The critical current density of current induced magnetization switching of unit cell thickness $Mn_{2.15}Sn$ thin film is minimized to 1 MA/cm^2. Both damping-like and field-like torques make significant contribution to their magnetization switching scheme. XMCD proves that a weak moment (compensated ferrimagnet) usually requires less energy to switch with low power consumption.

In the future, we try to decrease the resistivity then at the same time increase the spin Hall conductivity of spin Hall effect materials, maximizing the interface transparency, tuning properties by modifying the growth orientation of thin films, and excite motion of different spin textures such as skyrmions, antiskyrmions, merons et al. at room temperature.

Bibliography

1. Apalkov, Dmytro, Bernard Dieny, and J. M. Slaughter. Magnetoresistive random access memory. *Proceedings of the IEEE* 104.10 (2016): 1796-1830.
2. Zhu, Jian-Gang. Magnetoresistive random access memory: The path to competitiveness and scalability. *Proceedings of the IEEE* 96.11 (2008): 1786-1798.
3. Tehrani, Saied, et al. Magnetoresistive random access memory using magnetic tunnel junctions. *Proceedings of the IEEE* 91.5 (2003): 703-714.
4. Liu, Luqiao, et al. Spin-torque ferromagnetic resonance induced by the spin Hall effect. *Physical Review Letters* 106.3 (2011): 036601.
5. Siddiqui, Saima A., et al. Current-induced domain wall motion in a compensated ferrimagnet. *Physical Review Letters* 121.5 (2018): 057701.
6. Wadley, Peter, et al. Electrical switching of an antiferromagnet. *Science* 351.6273 (2016): 587-590.
7. Duine, R. A., et al. Synthetic antiferromagnetic spintronics. *Nature Physics* 14.3 (2018): 217-219.
8. Zijlstra, T., et al. Epitaxial aluminum nitride tunnel barriers grown by nitridation with a plasma source. *Applied Physics Letters* 91.23 (2007): 233102.
9. Parkin, Stuart SP, et al. Giant tunnelling magnetoresistance at room temperature with MgO (100) tunnel barriers. *Nature Materials* 3.12 (2004): 862-867.
10. Lee, Young Min, et al. Giant tunnel magnetoresistance and high annealing stability in CoFeB / MgO / CoFeB magnetic tunnel junctions with synthetic pinned layer. *Applied Physics Letters* 89.4 (2006): 042506.
11. Liu, Luqiao, et al. Spin-torque switching with the giant spin Hall effect of tantalum. *Science* 336.6081 (2012): 555-558.
12. Pai, Chi-Feng, et al. Spin transfer torque devices utilizing the giant spin Hall effect of tungsten. *Applied Physics Letters* 101.12 (2012): 122404.
13. Demasius, Kai-Uwe, et al. Enhanced spin–orbit torques by oxygen incorporation in tungsten films. *Nature Communications* 7.1 (2016): 1-7.
14. Wang, Yi, et al. Room temperature magnetization switching in topological insulator-ferromagnet heterostructures by spin-orbit torques. *Nature Communications* 8.1 (2017): 1-6.

15. Samanta, Manisha, et al. Intrinsically low thermal conductivity and high carrier mobility in dual topological quantum material, n-Type BiTe. *Angewandte Chemie International Edition* 59.12 (2020): 4822-4829.
16. Khang, Nguyen Huynh Duy, Yugo Ueda, and Pham Nam Hai. A conductive topological insulator with large spin Hall effect for ultralow power spin–orbit torque switching. *Nature Materials* 17.9 (2018): 808-813.
17. Wu, Hao, et al. Spin-orbit torque switching of a nearly compensated ferrimagnet by topological surface states. *Advanced Materials* 31.35 (2019): 1901681.
18. Shi, Shuyuan, et al. All-electric magnetization switching and Dzyaloshinskii–Moriya interaction in WTe_2/ferromagnet heterostructures. *Nature Nanotechnology* 14.10 (2019): 945-949.
19. Tang, Shujie, et al. Quantum spin Hall state in monolayer 1T'-WTe_2. *Nature Physics* 13.7 (2017): 683-687.
20. Zhou, Jiaqi, et al. Intrinsic spin Hall conductivity of the semimetals $MoTe_2$ and WTe_2. *Physical Review B* 99.6 (2019): 060408.
21. Xu, Hongjun, et al. High spin Hall conductivity in large-area type-II Dirac semimetal $PtTe_2$. *Advanced Materials* 32.17 (2020): 2000513.
22. Husain, Sajid, et al. Large damping-like spin–orbit torque in a 2d conductive 1T-TaS_2 monolayer. *Nano letters* 20.9 (2020): 6372-6380.
23. Muduli, P. K., et al. Evaluation of spin diffusion length and spin Hall angle of the antiferromagnetic Weyl semimetal Mn_3Sn. *Physical Review B* 99.18 (2019): 184425.
24. Bai, H., et al. Control of spin-orbit torques through magnetic symmetry in differently oriented noncollinear antiferromagnetic Mn_3Pt. *Physical Review B* 104.10 (2021): 104401.
25. Zhang, Weifeng, et al. Giant facet-dependent spin-orbit torque and spin Hall conductivity in the triangular antiferromagnet $IrMn_3$. *Science Advances* 2.9 (2016): e1600759.
26. Hirsch, J. E. Spin hall effect. *Physical Review Letters* 83.9 (1999): 1834.
27. Sinova, Jairo, et al. Spin hall effects. *Reviews of Modern Physics* 87.4 (2015): 1213.
28. Yang, See-Hun, Kwang-Su Ryu, and Stuart Parkin. Domain-wall velocities of up to 750 m s^{-1} driven by exchange-coupling torque in synthetic antiferromagnets. *Nature Nanotechnology* 10.3 (2015): 221-226.

29. Guan, Yicheng, et al. Increased efficiency of current-induced motion of chiral domain walls by interface engineering. *Advanced Materials* 33.10 (2021): 2007991.
30. Ryu, Kwang-Su, et al. Chiral spin torque at magnetic domain walls. *Nature Nanotechnology* 8.7 (2013): 527-533.
31. Ryu, Kwang-Su, et al. Chiral spin torque arising from proximity-induced magnetization. *Nature Communications* 5.1 (2014): 1-8.
32. Shao, Qiming, et al. Roadmap of spin-orbit torques. *IEEE Transactions on Magnetics* (2021).
33. Ramaswamy, Rajagopalan, et al. Recent advances in spin-orbit torques: Moving towards device applications. *Applied Physics Reviews* 5.3 (2018): 031107.
34. Manchon, Aurelien, et al. Current-induced spin-orbit torques in ferromagnetic and antiferromagnetic systems. *Reviews of Modern Physics* 91.3 (2019): 035004.
35. Yim, W. M., et al. Epitaxially grown AlN and its optical band gap. *Journal of Applied Physics* 44.1 (1973): 292-296.
36. Kubota, Hitoshi, et al. Large magnetoresistance in magnetic tunnel junctions using Co-Mn-Al full Heusler alloy. *Japanese Journal of Applied Physics* 43.7B (2004): L984.
37. Zhang, X-G., and W. H. Butler. Large magnetoresistance in bcc Co / MgO / Co and FeCo / MgO / FeCo tunnel junctions. *Physical Review B* 70.17 (2004): 172407.
38. Parkin, Stuart SP, Masamitsu Hayashi, and Luc Thomas. Magnetic domain-wall racetrack memory. *Science* 320.5873 (2008): 190-194.
39. Parkin, Stuart, and See-Hun Yang. Memory on the racetrack. *Nature Nanotechnology* 10.3 (2015): 195-198.
40. Annunziata, A. J., et al. Racetrack memory cell array with integrated magnetic tunnel junction readout. *2011 International Electron Devices Meeting*. IEEE, 2011.
41. Jensen, Pablo, et al. Growth and percolation of thin films: A model incorporating deposition, diffusion and aggregation. *Chaos, Solitons & Fractals* 6 (1995): 227-236.
42. Šmilauer, Pavel. Thin metal films and percolation theory. *Contemporary Physics* 32.2 (1991): 89-102.
43. Han, Jiahao, et al. Room-temperature spin-orbit torque switching induced by a topological insulator. *Physical Review Letters* 119.7 (2017): 077702.
44. Martinez, Eduardo, Satoru Emori, and Geoffrey SD Beach. Current-driven domain wall motion along high perpendicular anisotropy multilayers: The role of the

Rashba field, the spin Hall effect, and the Dzyaloshinskii-Moriya interaction. *Applied Physics Letters* 103.7 (2013): 072406.

45. Yang, See-Hun, Chirag Garg, and Stuart SP Parkin. Chiral exchange drag and chirality oscillations in synthetic antiferromagnets. *Nature Physics* 15.6 (2019): 543-548.
46. Hayashi, Masamitsu, et al. Dependence of current and field driven depinning of domain walls on their structure and chirality in permalloy nanowires. *Physical Review Letters* 97.20 (2006): 207205.
47. Moore, T. Aetal, et al. High domain wall velocities induced by current in ultrathin Pt / Co / AlOx wires with perpendicular magnetic anisotropy. *Applied Physics Letters* 93.26 (2008): 262504.
48. Pollard, Shawn D., et al. Observation of stable Néel skyrmions in cobalt/palladium multilayers with Lorentz transmission electron microscopy. *Nature Communications* 8.1 (2017): 1-8.
49. Liu, Luqiao, et al. Current-induced switching of perpendicularly magnetized magnetic layers using spin torque from the spin Hall effect. *Physical Review Letters* 109.9 (2012): 096602.
50. Zhao, Bing, et al. Unconventional charge – spin Conversion in Weyl-semimetal WTe_2. *Advanced Materials* 32.38 (2020): 2000818.
51. Fukami, Shunsuke, et al. Magnetization switching by spin–orbit torque in an antiferromagnet–ferromagnet bilayer system. *Nature Materials* 15.5 (2016): 535-541.
52. Yang, Hongxin, et al. Anatomy of Dzyaloshinskii-moriya interaction at Co/Pt interfaces. *Physical Review Letters* 115.26 (2015): 267210.
53. Tokura, Yoshinori, and Naoya Kanazawa. Magnetic skyrmion materials. *Chemical Reviews* 121.5 (2020): 2857-2897.
54. Robertson, MacCallum, et al. In-plane Néel wall chirality and orientation of interfacial Dzyaloshinskii-Moriya vector in magnetic films. *Physical Review B* 102.2 (2020): 024417.
55. Slonczewski, John C. Conductance and exchange coupling of two ferromagnets separated by a tunneling barrier. *Physical Review B* 39.10 (1989): 6995.
56. Parkin, S. S. P., N. More, and K. P. Roche. Oscillations in exchange coupling and magnetoresistance in metallic superlattice structures: Co/Ru, Co/Cr, and Fe/Cr. *Physical Review Letters* 64.19 (1990): 2304.

57. Edwards, D. M., et al. Oscillations of the exchange in magnetic multilayers as an analog of de Haas–van Alphen effect. *Physical Review Letters* 67.4 (1991): 493.
58. Bruno, P. Theory of interlayer magnetic coupling. *Physical Review B* 52.1 (1995): 411.
59. Gupta, Kriti, et al. Disorder dependence of interface spin memory loss. *Physical Review Letters* 124.8 (2020): 087702.
60. Fache, T., et al. Determination of spin Hall angle, spin mixing conductance, and spin diffusion length in CoFeB/Ir for spin-orbitronic devices. *Physical Review B* 102.6 (2020): 064425.
61. Bass, Jack, and William P. Pratt. Spin-diffusion lengths in metals and alloys, and spin - flipping at metal/metal interfaces: an experimentalist's critical review. *Journal of Physics: Condensed Matter* 19.18 (2007): 183201.
62. Cubukcu, Murat, et al. Ultra-fast perpendicular spin–orbit torque MRAM. *IEEE Transactions on Magnetics* 54.4 (2018): 1-4.
63. Apalkov, Dmytro, et al. Spin-transfer torque magnetic random access memory (STT-MRAM). *ACM Journal on Emerging Technologies in Computing Systems (JETC)* 9.2 (2013): 1-35.
64. Sato, Noriyuki, et al. Two-terminal spin–orbit torque magnetoresistive random access memory. *Nature Electronics* 1.9 (2018): 508-511.
65. Pfleiderer, Christian, and Achim Rosch. Single skyrmions spotted. *Nature* 465.7300 (2010): 880-881.
66. Roessler, Ulrich K., A. N. Bogdanov, and C. Pfleiderer. Spontaneous skyrmion ground states in magnetic metals. *Nature* 442.7104 (2006): 797-801.
67. Bogdanov, A. N., and U. K. Rößler. Chiral symmetry breaking in magnetic thin films and multilayers. *Physical Review Letters* 87.3 (2001): 037203.
68. Thiaville, A., et al. Domain wall motion by spin-polarized current: a micromagnetic study. *Journal of Applied Physics* 95.11 (2004): 7049-7051.
69. Yu, X. Z., et al. Real-space observation of a two-dimensional skyrmion crystal. *Nature* 465.7300 (2010): 901-904.
70. Yu, X. Z., et al. Near room-temperature formation of a skyrmion crystal in thin-films of the helimagnet FeGe. *Nature Materials* 10.2 (2011): 106-109.
71. Seki, Shinichiro, and Masahito Mochizuki. *Skyrmions in magnetic materials*. Cham: Springer International Publishing, 2016.

72. Sondhi, Shivaji Lal, et al. Skyrmions and the crossover from the integer to fractional quantum Hall effect at small Zeeman energies. *Physical Review B* 47.24 (1993): 16419.

73. Abolfath, M., et al. Critical comparison of classical field theory and microscopic wave functions for skyrmions in quantum Hall ferromagnets. *Physical Review B* 56.11 (1997): 6795.

74. Jena, Jagannath, et al. Elliptical Bloch skyrmion chiral twins in an antiskyrmion system. *Nature Communications* 11.1 (2020): 1-9.

75. Srivastava, Abhay K., et al. Observation of robust Néel skyrmions in metallic PtMnGa. *Advanced Materials* 32.7 (2020): 1904327.

76. Nayak, Ajaya K., et al. Magnetic antiskyrmions above room temperature in tetragonal Heusler materials. *Nature* 548.7669 (2017): 561-566.

77. Adams, T., et al. Skyrmion lattice domains in $Fe_{1-x}Co_xSi$. *Journal of Physics: Conference Series*. Vol. 200. No. 3. IOP Publishing, 2010.

78. Janson, Oleg, et al. The quantum nature of skyrmions and half-skyrmions in Cu_2OSeO_3. *Nature Communications* 5.1 (2014): 1-11.

79. Soumyanarayanan, Anjan, et al. Tunable room-temperature magnetic skyrmions in Ir/Fe/Co/Pt multilayers. *Nature Materials* 16.9 (2017): 898-904.

80. Raju, M., et al. The evolution of skyrmions in Ir/Fe/Co/Pt multilayers and their topological Hall signature. *Nature Communications* 10.1 (2019): 1-7.

81. Yasui, Yuuki, et al. Imaging the coupling between itinerant electrons and localised moments in the centrosymmetric skyrmion magnet $GdRu_2Si_2$. *Nature Communications* 11.1 (2020): 1-6.

82. Khanh, Nguyen Duy, et al. Nanometric square skyrmion lattice in a centrosymmetric tetragonal magnet. *Nature Nanotechnology* 15.6 (2020): 444-449.

83. Shibata, K., et al. Towards control of the size and helicity of skyrmions in helimagnetic alloys by spin–orbit coupling. *Nature Nanotechnology* 8.10 (2013): 723-728.

84. Wynn, C. M., et al. Magnetic dipole − dipole interactions and single-ion anisotropy: revisiting a classical approach to magnets. *Chemistry of Materials* 9.10 (1997): 2156-2163.

85. Yu, Xiuzhen, et al. Magnetic stripes and skyrmions with helicity reversals. *Proceedings of the National Academy of Sciences* 109.23 (2012): 8856-8860.

86. Yu, X. Z., et al. Biskyrmion states and their current-driven motion in a layered manganite. *Nature Communications* 5.1 (2014): 1-7.

87. Woo, Seonghoon, et al. Observation of room-temperature magnetic skyrmions and their current-driven dynamics in ultrathin metallic ferromagnets. *Nature Materials* 15.5 (2016): 501-506.

88. Heinze, Stefan, et al. Spontaneous atomic-scale magnetic skyrmion lattice in two dimensions. *Nature Physics* 7.9 (2011): 713-718.

89. Romming, Niklas, et al. Writing and deleting single magnetic skyrmions. *Science* 341.6146 (2013): 636-639.

90. Heinze, S., et al. Real-space imaging of two-dimensional antiferromagnetism on the atomic scale. *Science* 288.5472 (2000): 1805-1808.

91. Wang, Lingfei, et al. Ferroelectrically tunable magnetic skyrmions in ultrathin oxide heterostructures. *Nature Materials* 17.12 (2018): 1087-1094.

92. Meng, Keng-Yuan, et al. Observation of nanoscale skyrmions in $SrIrO_3$ / $SrRuO_3$ bilayers. *Nano Letters* 19.5 (2019): 3169-3175.

93. Chakraborty, Anirban, et al. Magnetic skyrmions in a thickness tunable 2D ferromagnet from a defect driven Dzyaloshinskii-Moriya interaction. *Advanced Materials* (2022): 2108637.

94. Wu, Yingying, et al. Néel-type skyrmion in WTe_2 / Fe_3GeTe_2 van der Waals heterostructure. *Nature Communications* 11.1 (2020): 1-6.

95. Yamaguchi, M., H. Inui, and K. Ito. High-temperature structural intermetallics. *Acta Materialia* 48.1 (2000): 307-322.

96. Tang, Zhaolin, Fuhui Wang, and Weitao Wu. Effect of MCrAlY overlay coatings on oxidation resistance of TiAl intermetallics. *Surface and Coatings Technology* 99.3 (1998): 248-252.

97. Cinca, Nuria, Carlos Roberto Camello Lima, and Jose Maria Guilemany. An overview of intermetallics research and application: Status of thermal spray coatings. *Journal of Materials Research and Technology* 2.1 (2013): 75-86.

98. Filippou, Panagiotis Ch, et al. Chiral domain wall motion in unit-cell thick perpendicularly magnetized Heusler films prepared by chemical templating. *Nature Communications* 9.1 (2018): 1-10.

99. Kurumaji, Takashi, et al. Skyrmion lattice with a giant topological Hall effect in a frustrated triangular-lattice magnet. *Science* 365.6456 (2019): 914-918.

100. Peng, Licong et al. Lorentz transmission electron microscopy studies on topological magnetic domains. *Chinese Physics B* 27.6 (2018): 066802.

101. Bader, S.D. & Parkin, S. S. Spintronics. *Annu. Rev. Condens. Matter Phys.* ***1,*** 71-88, (2010).

102. Žutić, I., Fabian, J. & Sarma, S.D. Spintronics: Fundamentals and applications. *Review Modern Physics* ***76,*** 323, (2004).

103. Wu, S. F., et al. Observation of the quantum spin Hall effect up to 100 Kelvin in a monolayer crystal. *Science* **359,** 76-79, (2018).

104. Garello. K. et al. Symmetry and magnitude of spin-orbit torques in ferromagnetic heterostructures. *Nature Nanotechnology* **8,** 587-593, (2013).

105. Finley, J. et al. Spin-orbit torque switching in a nearly compensated Heusler ferrimagnet. *Advanced Materials* **31,** 1805361, (2019).

106. Xie, X. J. et al. Controllable field-free switching of perpendicular magnetization through bulk spin-orbit torque in symmetry-broken ferromagnetic films. *Nature Communication* **12,** 1-10, (2021).

107. Zheng, Z. Y. et al. Field-free spin-orbit torque-induced switching of perpendicular magnetization in a ferrimagnetic layer with a vertical composition gradient. *Nature Communication* **12,** 4555, (2021).

108. Graf, T., Felser, C., & Parkin, S. S. Simple rules for the understanding of Heusler compounds. *Progress Solid State Chemistry* **39,** 1-50, (2011).

109. Faleev, S. V. et al. Heusler compounds with perpendicular magnetic anisotropy and large tunneling magnetoresistance. *Physicsl Review Materials* **1,** 024402, (2017).

110. Felser, C. et al. Tetragonal Heusler compounds for spintronics. *IEEE Transactions on Magnetics* **49,** 682-685, (2013).

111. . Martin, J. et al. Direct observation of half-metallicity in the Heusler compound Co_2MnSi. *Nature Communication* **5,** 1-5, (2014).

112. Nayak, A. K. et al. Design of compensated ferrimagnetic Heusler alloys for giant tunable exchange bias. *Nature Materials* **14,** 679-684, (2015).

113. Galanakis, I., & Şaşıoğlu, E. High T_C half-metallic fully - compensated ferrimagnetic Heusler compounds. *Applied Physics Letters* **99,** 052509, (2011).

114. Jeong, J. W. et al. Termination layer compensated tunnelling magnetoresistance in ferrimagnetic Heusler compounds with high perpendicular magnetic anisotropy. *Nature Communication* **7,** 1-8, (2016).

115. Jamer, M. E. et al. Compensated ferrimagnetism in the zero-moment Heusler alloy Mn_3Al. *Physical Review Applied* **7,** 064036, (2017).

116. Ferrante, Y. et al. Tetragonal Mn_3Sn Heusler films with large perpendicular magnetic anisotropy deposited on metallic MnN underlayers using amorphous substrates. *APL Material* **7,** 031103, (2019).

117. Liu, L. et al. Symmetry-dependent field-free switching of perpendicular magnetization. *Nature Nanotechnology* **16,** 277-282, (2021).

118. Yu, G. Q. et al. Switching of perpendicular magnetization by spin–orbit torques in the absence of external magnetic fields. *Nature Nanotechnology* **9,** 548-554, (2014).

119. Wu, H. et al. Chiral symmetry breaking for deterministic switching of perpendicular magnetization by spin–orbit torque. *Nano Letters* **21,** 515-521, (2020).

120. Tang, M. et al. Bulk spin torque-driven perpendicular magnetization switching in $L1_0$ FePt single layer. *Advanced Materials* **32,** 2002607, (2020).

121. Wang, P. et al. Giant spin Hall effect and spin-orbit torques in 5d transition metal – aluminum alloys from extrinsic potential scattering. Unsubmitted, (2021)

122. Banerjee, C. et al. Single pulse all-optical toggle switching of magnetization without gadolinium in the ferrimagnet Mn_2Ru_xGa. *Nature Communication* **11,** 1-6, (2020).

123. Ren, L. Z. et al. Spin-orbit torque switching of a high - quality perpendicularly magnetized ferrimagnetic Heusler Mn_3Ge film. *ACS Applied Materials & Interfaces.* **13,** 18294-18300, (2021).

124. Zhao, X. P. et al. Spin-orbit torque induced magnetization switching in ferrimagnetic Heusler alloy $D0_{22}$-Mn_3Ga with large perpendicular magnetic anisotropy. *Applied Physics Letters* **115,** 142405, (2019).

125. Zuo, J. M., et al. Lattice and strain analysis of atomic resolution *Z*-contrast images based on template matching. *Ultramicroscopy* **136,** 50-60, (2014).

126. Kim, J. Y. et al. Layer thickness dependence of the current-induced effective field vector in Ta | CoFeB | MgO. *Nature Materials* **12,** 240-245, (2013).

127. Pi, U. H. et al. Tilting of the spin orientation induced by Rashba effect in ferromagnetic metal layer. *Applied Physics Letters* **97,** 162507, *(*2010).

128. Zhu, L. J., Ralph, D. C., Buhrman, R. A. Enhancement of spin transparency by interfacial alloying. *Physical Review B* **99,** 180404, (2019).

129. Zhu, L. J., Ralph, D. C., Buhrman, R. A. Effective spin-mixing conductance of heavy-metal-ferromagnet interfaces. *Physical Review Letters* **123,** 057203, (2019).

130. Zhu, L. J., Ralph, D. C., & Buhrman, R. A. Spin-orbit torques in heavy-metal-ferromagnet bilayers with varying strengths of interfacial spin-orbit coupling. *Physical Review Letters* **122,** 077201, (2019).

Acknowledgement

I really appreciate Prof. Dr. Stuart S.P. Parkin provide me an opportunity to join Max-Planck-Institute of Microstructure Physics and work with him in the past several years. This journey is really interesting and tough for me. We indeed found some new materials and new phenomenon that is really useful to promote the practical application of them into next generation of magnetoresistive random-access memories. Using science and technology to help others and promote the development of the world is always my lifelong wishes. It's my great pleasure to work with Prof. Dr. Stuart S.P. Parkin during my Ph.D process.

IBM scientist Dr. See-Hun Yang has offered me a huge amount of help especially in data analysis, figures preparation and papers writing selflessly. I grew a lot from a fresh Ph.D student to a qualified PhD candidate during the countless discussions. Many thanks to See-Hun.

As a team, Dr. Jaechun Jeon, Dr. Andrea Migliorini, Dr. Rana Saha, Dr. Hakan Deniz, Dr. Andriy Styervoyedov, Jiho Yoon, and Scientist Holger Meyerheim and some other members have helped me a lot especially in the aspect of electrical and magnetic properties measurement. They are all good experts. I really thank all my Chinese colleagues, we can relax a lot in the manner of playing games or just gossips talking from the tough and difficult Ph.D study.

Several years can't back to China to accompany my parents because of serious Covid-19 pandemic, as the only son in the families, I owed a lot to my parents. Thanks for the unconditional love and support from my parents. I really appreciate my girlfriend Dr. Qun Yang unconditionally support me in the most hard and difficult time of my PhD life. Thanks!

I thank all the people who gave me help and suggestions in the past several years, thanks again.

List of Publications

Thesis related publications

Peng Wang et al. Giant spin Hall effect and spin-orbit torques in 5*d* transition metal- aluminum alloys from extrinsic scattering. *Adv. Mater.* (2022): 2109406.

Peng Wang et al. Strain-gradient induced Néel skyrmions in ferromagnetic alloys. (To be submitted).

Peng Wang et al. Field-free spin-orbit torque switching of tetragonal Mn_xSn Heusler by atomic step heterojunction. (To be submitted).

Other publications

Fan, Li, Yicheng Guan, Peng, Wang, et al. All electrical reading and writing of spin chirality, *Sci. Adv.*, accepted.

Peng, Wang et al. One-dimensional carbon/SiC nanocomposites with tunable dielectric and broadband electromagnetic wave absorption properties. *Carbon* 125 (2017): 207-220.

Peng, Wang et al. Flexible SiC/Si_3N_4 composite nanofibers with in situ embedded graphite for highly efficient electromagnetic wave absorption. *ACS Applied Materials & Interfaces* 9.34 (2017): 28844-28858.

Peng, Wang et al. "Electrospinning of graphite/SiC hybrid nanowires with tunable dielectric and microwave absorption characteristics." *Composites Part A: Applied Science and Manufacturing* 104 (2018): 68-80.

Academic Curriculum Vitae

First name:	Peng
Family name:	Wang
Gender:	Male
Date of Birth:	August 20th, 1992
Nationality:	Chinese

ACADEMIC EDUCATION

05/2018-11/2022	*Ph.D student (Physics)* Martin-Luther-University Halle-Wittenberg, Max-Planck Institute of Microstructure Physics, Halle, Germany Supervisor: Prof. Dr. Stuart S.P. Parkin
09/2015 - 03/2018	*Master's degree in Engineering* Northwestern Polytechnical University, Xi'an, China
09/2011 - 07/2015	*Bachelor's degree in Science* School of Sciences China University of Petroleum (East China), Qingdao, China

Peng Wang

Halle (Saale), Germany

March 14th, 2022

Halle (Saale), den 03.14.2022 .....

(Peng Wang)

Eidesstattliche Erklärung

Ich, Peng Wang, erkläre an Eides statt, dass ich die Arbeit selbstständig und ohne fremde Hilfe verfasst, keine anderen als die von mir angegebenen Quellen und Hilfsmittel benutzt und die den benutzten Werken wörtlich oder inhaltlich entnommenen Stellen als solche kenntlichgemacht habe.

Halle (Saale), den 03.14.2022 .....

(Peng Wang)